Structuring Spatiotemporal Oxygen Environments for Microbial Single-Cell Analysis in Microfluidics

Strukturierung räumlich-zeitlicher Sauerstoffumgebungen in der mikrofluidischen Einzelzellanalyse von Mikroorganismen

Von der Fakultät für Maschinenwesen der Rheinisch-Westfälischen Technischen Hochschule Aachen zur Erlangung des akademischen Grades eines Doktors der Ingenieurwissenschaften genehmigte Dissertation

vorgelegt von

Keitaro Kasahara

Berichter: Univ.-Prof. Dr. rer. nat. Wolfgang Wiechert
Univ.-Prof. Dr.-Ing. Jørgen Magnus

Tag der mündlichen Prüfung: 06.06.2025

Abstract

Microbial single-cell analysis using microfluidics is a promising method for studying microbial growth behavior in detail under precisely controlled environments. However, little effort has been made to incorporate spatiotemporal O_2 control, a critical factor influencing microbial growth and physiology. This dissertation explores various strategies for establishing straightforward O_2 control, temporal O_2 control in the range of seconds to minutes, and spatial O_2 control in the range of micrometers.

First, a comprehensive experimental platform was developed that is transferable to microbial single-cell analysis within various formats of microfluidic devices. Using a low-cost 3D-printed mini-incubator surrounding the air-permeable PDMS microfluidic chip, the O_2 concentration in the microfluidic chip was controlled. The O_2 sensing method using FLIM and an O_2-sensitive dye was also implemented, allowing direct measurement of the O_2 availability inside the fluid channels. Subsequent imaging with time-lapse microscopy and deep-learning-based image analysis provided a solid platform for data analysis.

Furthermore, a double-layer microfluidic chip was developed to implement spatiotemporal O_2 control in microbial single-cell analysis. The newly developed microfluidic platform could reproduce O_2 oscillations occurring within seconds to minutes, thus enabling time-resolved microbial growth analysis at single-cell resolution. The case studies were performed by studying the aerobic and anaerobic growth and adaptation of *E. coli* and *C. glutamicum*. The growth analysis results revealed aerobic/anaerobic specific growth and growth adaptation in response to O_2 oscillations, insights that cannot be obtained using conventional cultivation setups.

Lastly, several different designs of the double-layer microfluidic chip were introduced to achieve spatial O_2 control in microbial single-cell analysis in the range from millimeters down to micrometers. The experimental results demonstrated the capability of spatial O_2 control by diffusion. The proposed concepts and devices are expected to be used for further microbial growth characterization under spatiotemporally structured O_2 microenvironments.

Zusammenfassung

Die Einzelzellanalyse lebender Mikroorganismen in mikrofluidischen Versuchsanordnungen ist eine innovative experimentelle Methode zur Aufschlüsselung des mikrobiellen Wachstums mit Einzelzell-Auflösung. Die Mikrofluidik ermöglicht dabei die Kultivierung der Organismen unter genau kontrollierten Bedingungen. Bisher gibt es kaum veröffentliche Studien und technische Ansätze, in denen eine praktikable, räumlich-zeitliche O_2-Kontrolle im Mikrochip realisiert wurde. Dabei gehört Sauerstoff zu den Faktoren, die einen erheblichen Einfluss auf das mikrobielle Wachstum haben. In dieser Dissertation werden verschiedene Systeme zur Steuerung des im Chip vorhandenen Sauerstoffs entwickelt und experimentell charakterisiert. Diese neuen Methoden ermöglichen das Anlegen zeitlich veränderlicher O_2-Konzentrationen mit Umschaltvorgängen im Bereich von Sekunden und räumlich aufgelöste Sauerstoffgradienten im µm-Bereich.

Zugeschnitten auf die bereits vorhandenen mikrofluidischen Kultivierungssysteme, wurde zunächst eine universellere Inkubatorlösung entwickelt. Durch die Verwendung eines 3D-gedruckten Mini-Inkubators, der den gasdurchlässigen Mikrofluidikchip umgibt, konnte die O_2-Konzentration im Mikrofluidikchip einfach, wenn auch verhältnismäßig langsam gesteuert werden. Bildgebende Fluoreszenzlebenszeit-Messungen eines O_2-empfindlichen Farbstoffes wurden implementiert, welche eine räumlich-zeitlich aufgelöste Messung der O_2-Verfügbarkeit in den Fluidkanälen ermöglichen. Die Lebendzellmikroskopie erzeugt während des Experiments große Bilddatensätze, und die Deep-Learning basierte Bildanalyse im Anschluss an das Experiment ermöglicht, eine effiziente und robuste Analyse.

Darüber hinaus wurde ein integrativer Ansatz für einen zweilagigen mikrofluidischen Chip entwickelt, der eine erheblich schnellere O_2-Kontrolle in der mikrobiellen Einzelzellanalyse ermöglicht. Der neu entwickelte mikrofluidische Chip erlaubt reproduzierbare O_2-Oszillationen mit Perioden im Sekundenbereich und länger. Dieser Ansatz ermöglicht erstmalig durchgeführte, zeitlich aufgelöste Wachstumsanalysen unter schnellen Sauerstoff-Veränderungen. Diverse Fallstudien wurden durchgeführt, indem aerobes, anaerobes Wachstum und die zellulären Adaption von *E. coli* und *C. glutamicum* untersucht wurden, welche mit herkömmlichen Kultivierungsmethoden bisher nicht möglich waren.

In einer dritten Entwicklungsstufe, wurden zweischichtige mikrofluidische Chips entwickelt, die eine räumliche O_2-Kontrolle, z.B. das Anlegen von Gradienten im Bereich von mm bis µm ermöglichen. Erste experimentellen Ergebnisse waren erfolgreich und zeigen die Möglichkeit der räumlichen O_2-Kontrolle. Die vorgeschlagenen Konzepte sollen zukünftig für weitere Wachstumsanalysen in räumlich-zeitlich strukturierten O_2-Mikroumgebungen eingesetzt werden.

Contents

Abstract iv

Zusammenfassung vi

Nomenclature xiii

1 Motivation and Background 1

1.1 Spatiotemporally Structured Environments in Microbial Habitats 1

1.2 Oxygen and Microbial Growth 4

1.3 Microfluidics 6

1.4 Challenges and Requirements 9

1.5 Scope of Thesis 10

1.6 Thesis Outline 11

2 Technology Overview 15

2.1 Single-Cell Analysis in Microfluidics 15

2.2 Oxygen Sensing with Fluorescence Lifetime Imaging Microscopy 17

2.3 Deep Learning-Based Automated Image Analysis 19

3 Versatile System for Microbial Growth Analysis under Controlled Oxygen 21

3.1 Technical Concept 21

3.2 Materials and Methods 25

3.3 Results 32
3.4 Discussion 41

4 Double-Layer Microfluidics for Recreating Rapid Oxygen Oscillations 45
4.1 Technical Concept 46
4.2 Materials and Methods 48
4.3 Results 54
4.4 Discussion 73

5 Investigating Growth of *C. glutamicum* under Oscillating Oxygen Environments 77
5.1 Introduction 77
5.2 Materials and Methods 79
5.3 Results 80
5.4 Discussion 83

6 Microfluidic Chip Development for Spatial Oxygen Control 87
6.1 General Concept 87
6.2 Design 1: Side Gas Channels 88
6.3 Design 2: Double-Layer Chip with Large Gas Channels for High Throughput 91
6.4 Design 3: Double-Layer Chip with Finer Gas Channels for µm-Scale Gradient 93
6.5 Design 4: Double-Layer Chip with Glass-Made Top Layer 101
6.6 Discussion 107

7 Conclusions and Outlook 113
7.1 Conclusions 113
7.2 Outlook 114

Acknowledgements **119**

Bibliography **132**

Publications **136**

List of Figures **140**

List of Tables **141**

A Simulation Setup **143**

B Permission for Re-Use of Contents **145**

Nomenclature

Abbreviations

1D	One-dimensional
2D	Two-dimensional
3D	Three-dimensional
C. glutamicum	*Corynebacterium glutamicum*
E. coli	*Escherichia coli*
ATP	Adenosine triphosphate
BSA	Bovine serum albumin
CAD	Computer-aided design
CMOS	Complementary metal-oxide-semiconductor
DL	Deep learning
FFT	Fast Fourier transform
FLIM	Fluorescence lifetime imaging microscopy
FRET	Förster resonance energy transfer
GFP	Green fluorescent protein
IPTG	Isopropyl β-D-1- thiogalactopyranoside
LB	Lysogeny broth

OD	Optical density
OMERO	Open Microscopy Environment Remote Objects
PDMS	Polydimethylsiloxane
PEG	Polyethylene glycol
PFS	Perfect focus system
PTFE	Polytetrafluoroethylene
ROI	Region of interest
RTDP	Tris(2,2'-bipyridyl) dichlororuthenium(II) hexahydrate
S.D.	Standard deviation
Symbols	
α	Fraction of accessible fluorophore (-)
$\bar{\mu}_{\text{aerobic}}$	Phase-averaged growth rate under aerobic gassing phase (h^{-1})
$\bar{\mu}_{\text{anaerobic}}$	Phase-averaged growth rate under anaerobic gassing phase (h^{-1})
μ	Specific growth rate (h^{-1})
μ_{aerobic}	Specific growth rate under aerobic conditions (h^{-1})
$\mu_{\text{anaerobic}}$	Specific growth rate under anaerobic conditions (h^{-1})
$\mu_{\Delta t}$	Instantaneous growth rate (h^{-1})
$\mu_{0\%}$	Specific growth rate at constant 0% O_2 (h^{-1})
$\mu_{21\%}$	Specific growth rate at constant 21% O_2 (h^{-1})
ω	Spin-coating speed (rpm)
τ	Fluorescence lifetime (ns)
A_{colony}	Colony area (μm^2)
$A_{\text{single cell}}$	Single-cell area (μm^2)

C	Offset for anaerobic growth (h^{-1})
d	Distance (µm)
f_{O_2}	Fractional O_2 saturation in solution relative to pure O_2 (-)
h	Height (m, mm, µm)
I	Fluorescence intensity (a.u.)
K_q	Stern-Volmer quenching constant (-)
K_{O_2}	Michelis-Menten constant regarding O_2 availability (%)
l	Length (m, mm, µm)
$N_{\text{population}}$	Cell number in a colony
S_{O_2}	Percent O_2 saturation relative to pure O_2 (%)
T	Temperature (°C)
t	Time (s, min, h)
T'	Oscillation half period (min)
t_{recovery}	Time for growth recovery after switching gaseous conditions (min)
t_{response}	Time for growth response after switching gaseous conditions (min)
t_{diff}	Characteristic diffusion time (s)
$t_{x\%}$	Diffusion time to reach $x\%$ of the final O_2 saturation level (min)
W	Membrane thickness (m)
w	Width (m, mm, µm)
CO_2	Carbon dioxide
D	Diffusion coefficient (m^2/s)
L	Diffusion length (m)
N_2	Molecular nitrogen
O_2	Molecular oxygen

1 Motivation and Background

Microbial habitats are often not stable but spatiotemporally structured, which plays a crucial role in shaping microbial communities and their interactions. Molecular oxygen (O_2) particularly influences microbial growth and behavior, making it a critical factor to investigate. Microfluidic approaches are increasingly utilized to systematically study microbial growth, physiology, and interactions at the single-cell, population, and community levels under spatiotemporally structured O_2 conditions. These methods enable precise control over spatiotemporal microenvironments with real-time imaging capabilities — an advantage not feasible with conventional experimental setups. This chapter provides a comprehensive overview of the research background for this thesis, emphasizing relevant previous studies. The scope of the thesis is outlined, including challenges and requirements identified from the research background.

1.1 Spatiotemporally Structured Environments in Microbial Habitats

Microbes in natural habitats are exposed to spatiotemporally structured environmental conditions and have evolved strategies to adapt to these conditions [1]. These environments are characterized by variations in spatial arrangements and temporal dynamics, which significantly influence microbial behavior, coexistence, and evolutionary processes. Various parameters, such as O_2 availability [2], nutrients[3], pH [4], temperature [5], and light [6], are shaping complex microenvironments, serving as habitats for diverse microbial life. Natural habitats include various environments, ranging from soil and aquatic systems (ocean, river, lake, etc.) to host-associated microenvironments (gut, oral cavity, etc.).

Spatially arranged microenvironments in microbial habitats often arise from gradients or resource patchiness. Soil aggregate, for example, has tortuous and porous structures that restrict resource transport via diffusion or fluid flow, driving spatially heterogeneous

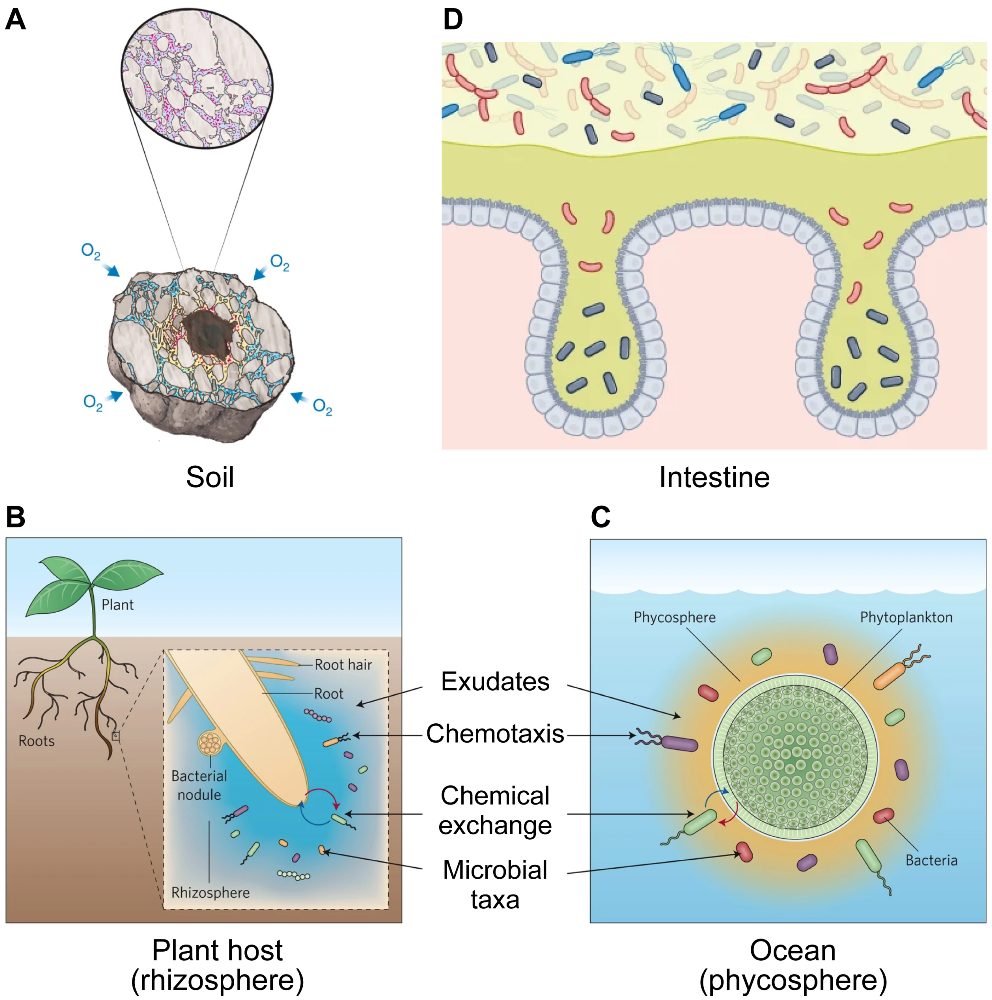

Figure 1.1: Spatiotemporally structured environments in microbial habitats. **(A)** Soil aggregate, **(B)** rhizosphere, **(C)** phycosphere, and **(D)** intestine (adapted with permission from **(A)** [7], **(B, C)** [8], and **(D)** [9].

distribution of resources and leading to spatial microbial patterns (Fig. 1.1A) [7, 10–12]. In the ocean at the microscale, a nutrient-rich region known as the "phycosphere" surrounds a phytoplankton cell, which creates gradients and patches of dissolved organic matter and O_2 exuded from the cells and offers aquatic bacteria a sweet spot of microenvironments (Fig. 1.1C) [3, 8]. Similar to the phycosphere is the rhizosphere, a small area near the plant root that offers bacteria organic substrate, making it a hotspot for microbial inhabitance (Fig. 1.1B) [8, 13]. In the intestine, distinctive protrusion and dead-end pocket structures (villus and crypt) exist, structuring resource gradients and forming spatial patterning of the gut microbiome (Fig. 1.1D) [9, 14]. Another example of spatial arrangement is biofilm, a layer of microbes that colonizes and develops on surfaces. Within these layered structures, resource gradients are structured by different diffusion rates due to varying distances from the surface and consumption of resources by various layers of microbial populations [15–17]. The scale of such spatial microenvironments is estimated by cell size ($\sim$ 0.4 - 2 µm range) in the case of non-motile bacterium and motility rate in the case of motile bacterium [3].

Adding to spatial aspects, temporal dynamics further complicate the configuration of microenvironments that microbes inhabit. Microbes proliferate in fluctuating environments on different time scales with different parameters. Fluctuations at long time scales can occur in months and seasons. Previous research has shown that seasonal drying and wetting cycles in tropical forests result in nutrient pulse and fluctuating nitrogen availability in soil on the timescale of months to seasons [18]. The short time scale can be in days and hours. For instance, plants and cyanobacteria, requiring light sources for photosynthesis, experience day/night cycles every around half a day [6]. Soil temperature can also fluctuate by day/night cycles and weather, which affects soil microbial respiration and promotes thermal adaptation [5]. In aquatic environments, microbes encounter new microenvironments in the time scale of seconds to minutes due to changes in surrounding conditions, displacement caused by fluid flow, and microbe's motility in the case of chemotactic bacteria [19]. The phycosphere, the nutrient hotspot explained earlier, can dissipate in minutes or even faster due to diffusion and turbulence in fluid [20, 21]. Temporal dynamics in microenvironments can also occur in animal hosts owing to daily activities, such as ingestion and breathing, and can be found in the nasal passage [4], lung [22] and intestine [23].

Spatiotemporally dynamic environments are also prevalent in biotechnological cultivation setups. In industrial-scale bioreactors, for instance, the stirring of large culture volumes often results in inefficient mixing, leading to the heterogeneous distribution of O_2 and nutrients (Fig. 1.2) [24–27]. Microbes cultivated in such a bioreactor experience fluctuating environments as they roam around different sections of the bioreactor [28, 29]. The heterogeneous distribution of resources and resulting cultivation in fluctuating environments can potentially lead to yield losses, so research efforts have been prompted to alleviate these gradients. However, achieving fully optimized and uniform cultivation

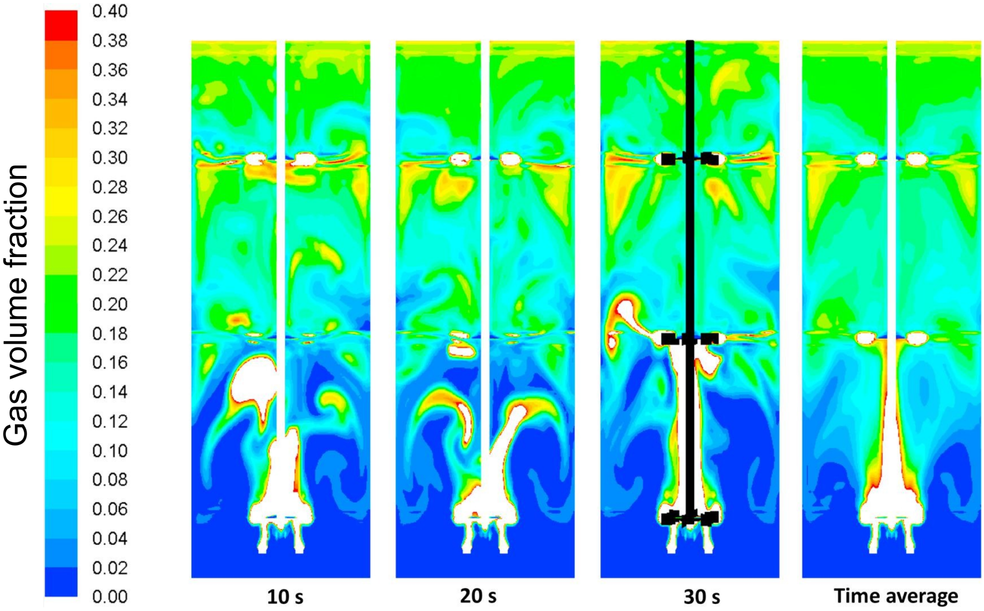

Figure 1.2: Spatiotemporally fluctuating environments in an industrial-scale bioreactor, illustrating gas volume fractions at different time points (adapted with permission from [27]).

conditions within a single vessel remains challenging.

Investigating microbial behavior in spatiotemporally structured environments will improve understanding of microbial adaptation strategies to external environmental changes that naturally occur. In a practical sense, these studies have the potential to offer insights into how to enhance efficiency in industrial biotechnology.

1.2 Oxygen and Microbial Growth

Among the various environmental conditions, the availability of O_2 is one of the most critical for microbial growth and physiology, as O_2 is intricately linked with a multitude of microbial processes, such as iron homeostasis (via spontaneous or enzymatic oxidation of soluble ferrous to insoluble and thus challenging to access ferric iron) [30]. O_2 is valuable as a primary electron acceptor for aerobic respiration in many microorganisms. While obligate aerobes and anaerobes essentially need either sufficient O_2 supply or strict O_2 limitation for growth, facultative anaerobes are capable of growing under both aerobic and anaerobic conditions by adapting their metabolic pathways between aerobic respiration and anaerobic respiration or fermentation depending on surrounding O_2 environments [31–33]. This characteristic of facultative anaerobes to adapt to different O_2 environments has been extensively studied in single-shift O_2 environments. The previous studies have involved the analysis of the intracellular adaptation, such as transcriptome [31], protein synthesis [34], metabolome [35], flux balance [36], and phenotypic adaptation like growth fitness [37].

Microbes behave following spatiotemporal O_2 environments based on their tolerance to O_2 availability. As a result, spatiotemporally heterogeneous O_2 environments could drive metabolic diversity and heterogeneity within populations. Within microbial populations, spatiotemporal O_2 environments can induce stress responses, such as oxidative stress under high O_2 levels (via the formation of reactive O_2 species as by-products of O_2 metabolism), which enhances microbial resilience or drives evolutionary adaptations [38]. Pathogenesis is also closely related to spatiotemporal O_2 gradients since pathogenic virulence and infection are influenced by the O_2 availability within host tissues [32, 39]. At the microbial community level, spatiotemporal O_2 environments mediate interspecies interactions, such as cross-feeding (aerobic microbes depleting O_2 and creating anaerobic conditions for obligate anaerobes) [7, 40], competition (several species competing for O_2) [41], and signaling (quorum sensing being modulated by O_2 gradients) [42]. These interactions lead to the organization of microbial spatial structures, represented by biofilms in soils, host tissues (for example, the gut microbiota), and many other occasions [16, 43, 44].

Despite the increasing need for detailed understandings of microbial behavior under spatiotemporally structured O_2 environments, several constraints have hindered such studies. Firstly, conventional cultivation techniques, including microtiter plates, shaking flasks, and bioreactors, do not facilitate environmental changes with defined spatiotemporal O_2 profiles on the time scale of seconds to minutes and the spatial scale of µm. Conventional laboratory cultivation setups typically lack environmental control capability, with minimal control over spatial distribution, time course, and resulting O_2 microenvironments. Furthermore, these setups are hardly suitable for fully resolving growth physiology with high spatiotemporal resolution due to the impracticality of repetitive sampling without disrupting the cultivation. Due to these limitations in (i) controlling O_2 in a spatiotemporal manner and (ii) resolving cell growth physiology with high spatiotemporal resolution, it has been challenging to analyze the cellular response to spatiotemporally structured O_2 environments regarding microbial growth and physiology.

1.3 Microfluidics

Today, microfluidics is gaining attention to overcome hurdles associated with conventional experimental setups in diverse fields. Microfluidics refers to the study dealing with small (nano to atto liters) amounts of fluids inside channels, typically with dimensions of tens to hundreds of micrometers [45]. Its characteristics at the microscale (for example, laminar flow) make the system distinctive from larger-scale systems, suited for handling small volumes of fluid precisely and, therefore, diverse applications in chemical, biological, and medical analyses [46, 47]. Microfluidics possesses the potential to solve the limitations in conventional setups (i, ii) mentioned in the previous section.

(i) Spatiotemporal O_2 control An elastomer called Polydimethylsiloxane (PDMS) is primarily used as a material for microfluidic devices. Leveraging its high air permeability [48, 49], the control of O_2 in microfluidics has been demonstrated for various biological applications [49–54], as depicted in Fig. 1.3. Many O_2 control is based on gas diffusion using multiple layers/side channels or chemical reactions leading to O_2 scavenging/generation. These devices have been previously used for various purposes, such as a micro bioreactor and platforms for biofilm studies and three-dimensional cell cultures. Since many of these developments have been tailored for mammalian cell cultivation and tissue engineering purposes, the scale of these devices is often larger than the scale required for microbial behavioral investigation, making a hurdle for microbiological applications.

(ii) Cell growth analysis with high spatiotemporal resolution In the last decade, experimental approaches combining time-lapse microscopy and microfluidics have been widely used to spatially and temporally resolve the behavior of single microbes and populations, for example, in terms of microbial growth [55], phenotypic population heterogeneity [56], and cellular interactions [57–61]. When studying cellular interactions, image-based single-cell analysis can provide new insights into the exchange of nutrients, conjugative transfer of plasmids, quorum sensing, and host-pathogen relations. Recent studies utilized microfluidic platforms for microbial growth and interaction studies in confined environments, for example, to investigate spatial microbial community organization in response to O_2 carbon counter-gradients in pore networks, microbial colo-

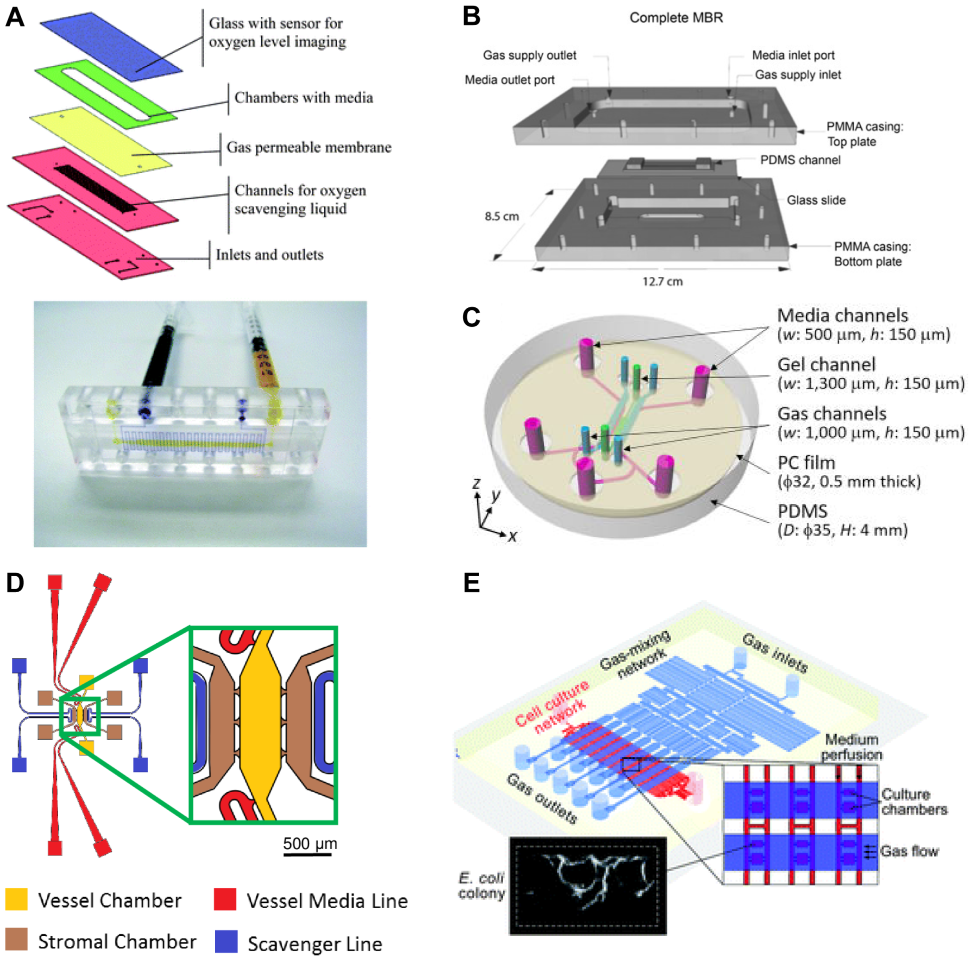

Figure 1.3: Microfluidic devices for spatiotemporal O_2 control. **(A)** Microfluidic O_2 gradient generator for biofilm studies. **(B)** Micro bioreactor providing control over O_2 and shear stress for stem and progenitor cells. **(C)** Three-dimensional cell culture microfluidic platform under spatiotemporally controlled O_2. **(D)** Microfluidic device to recreate physiologically relevant O_2 environments. **(E)** Double-layer microfluidic device for fine temporal O_2 control. (adapted with permission from **(A)** [51], **(B)** [52], **(C)** [49], **(D)** [54], and **(E)** [50]).

nization in a biologically relevant microstructure, and spatiotemporal interaction in a microbial community, as depicted in Fig. 1.4 [7, 62, 63]. Innovative microfluidics and

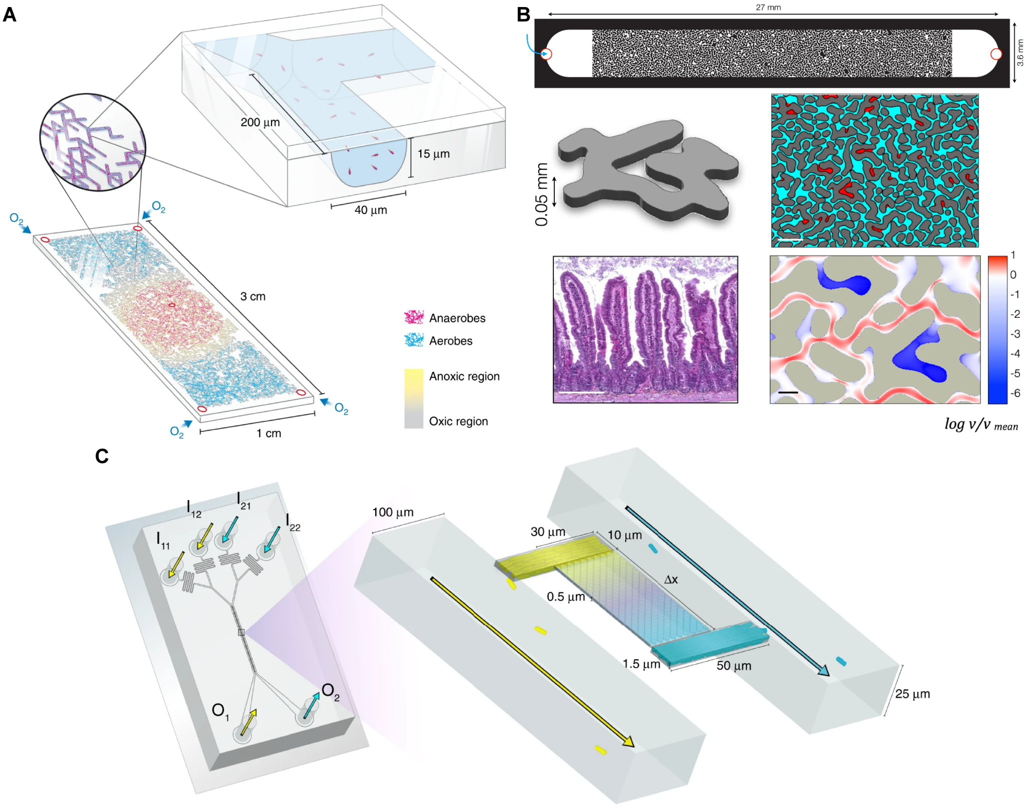

Figure 1.4: Microfluidic devices enabling microbial growth and interaction studies in confined environments. **(A)** Microfluidic device to study spatial microbial community organization in response to O_2 and carbon counter-gradients in pore networks. **(B)** Porous medium model microfluidic chip to investigate microbial colonization in a biologically relevant microstructure. **(C)** Microfluidic platform to investigate spatiotemporal interactions in a microbial community. (adapted with permission from **(A)** [7], **(B)** [62], and **(C)** [63]).

time-lapse imaging greatly benefit interaction studies. These single-cell approaches can provide complementary and novel data that are not accessible with population-based laboratory-scale methods.

As described in (i) and (ii), microfluidics offer a tailored experimental platform with precise environmental control and imaging at single-cell resolution. Utilizing these technologies could allow for mimicking natural microenvironments on-chip and extracting microbial growth and physiology data with high temporal resolution at the single-cell, population, and community levels.

1.4 Challenges and Requirements

Although promising advancements in microfluidics for microbiological research, there are still challenges to be solved. As mentioned in the previous section, the majority of the attempts for O_2 control and on-chip sensing demonstrated in microfluidic devices were made using relatively large cultivation channels for mammalian cells and were less suitable for microbial single-cell analysis [64]. Hence, only a few concepts are easily transferable to microbial single-cell analysis when focusing on usability.

Regarding temporal micro-environment control, there are a few microfluidic experimental systems to emulate oscillating pH and nutrients [65, 66]. However, few microfluidic devices have been developed for rapid O_2 control in seconds to minutes [67]. As a result, the correlation between microbial growth and the fluctuating O_2 environment has not been analyzed in detail, and there is a lack of understanding regarding the cellular capability to adapt to rapidly fluctuating O_2 environments. Recent studies have shown that microbial behavior in fluctuating environments, where state changes occur on the order of seconds to minutes, can differ from that observed in single-shift experiments [66, 68]. Investigating the impact of O_2 fluctuations on microbial growth would facilitate a more comprehensive understanding of species-specific adaptation processes that remain elucidated.

Spatial O_2 control has also been applied to microfluidic devices, mainly for mammalian cell cultivation, leading to a large-scale O_2 spatial control (such as an O_2 gradient in the scale of mm). Several previous reports investigated the aerotaxis of microorganisms [69–71]; however, these researches also utilized large-scale O_2 gradients, limiting the microbial growth analysis in spatially structured microenvironments in a scale similar to microbes (in µm order).

Aside from aspects of microbial cultivation and O_2 control, it remains a challenge to efficiently extract quantitative cellular properties from thousands of microscopy images acquired during time-lapse imaging. Integrating automated image analysis into the experimental approach could improve the efficiency and accuracy of data extraction. To achieve a more systematic investigation of the effect of O_2 levels in (micro)environments on microbial behavior, a comprehensive experimental platform is required. The setup should allow microbial cultures and single-cell analysis in defined O_2 environments. Finally, subsequent automated image analysis is essential to derive new information from statistically reliable large data sets.

1.5 Scope of Thesis

This thesis focuses on developing methods for spatiotemporal O_2 control within microfluidic systems to enable high-resolution analysis of microbial single-cell behavior (Fig. 1.5). The research also aims to showcase some case studies where developed microfluidic methods are utilized for understanding microbial dynamics under confined O_2 environments. The following key aspects are primarily tackled based on the challenges and requirements summarized in Section 1.4.

1. **Straightforward O_2 control**: A comprehensive experimental platform is developed that is easily transferable to microbial single-cell analysis within various formats of microfluidic devices. This platform development also intends to demonstrate the power of microfluidics to microbiologists interested in using microfluidic systems as a general tool for different biological studies.
2. **Temporal O_2 control in the range of seconds to minutes**: A microfluidic device allowing rapid O_2 control and microbial single-cell behavioral analysis is developed. Microbial cultivation under gas oscillations occurring in seconds to minutes is conducted to investigate the impact of O_2 oscillations on microbial growth and adaptation.
3. **Spatial O_2 control in the range of µm**: Various designs of microfluidic devices are tested to achieve fine spatial O_2 control. Such a device can be utilized to investigate the development of microbial communities in spatially structured microenvironments mimicking physiological and environmental conditions in nature.

In addition to the key aspects of this thesis mentioned above, a versatile image analysis platform is continuously being developed. This platform strengthens microfluidic experiments with automated time-lapse microscopy through deep-learning-based image analysis. This versatile and seamless platform allows efficient and reliable extraction of quantitative information from large datasets.

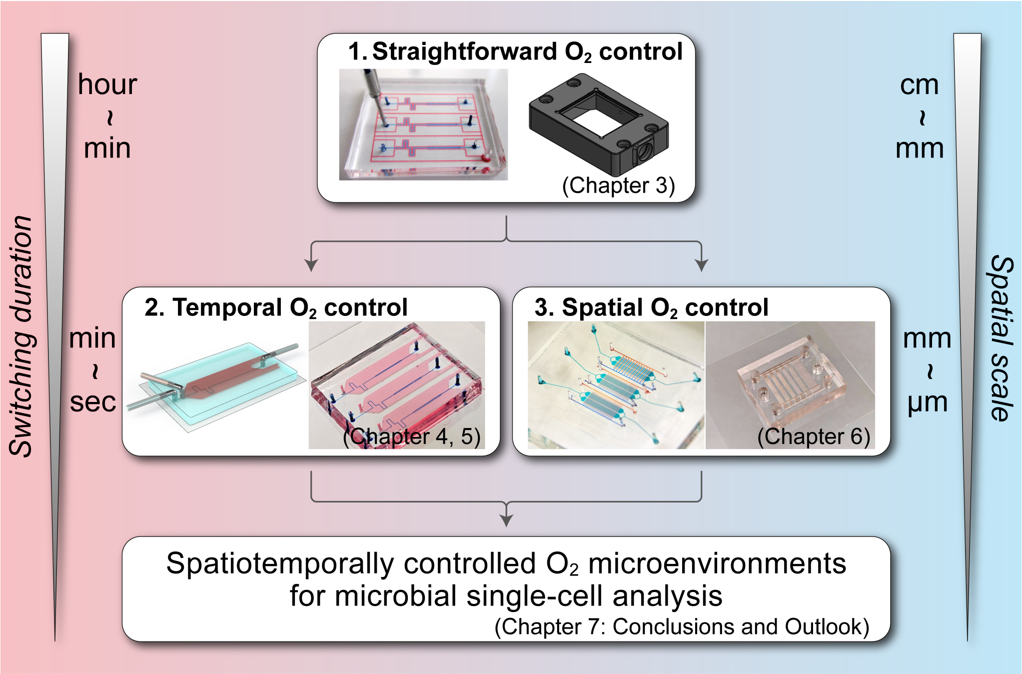

Figure 1.5: Schematic illustration describing the scope of the thesis.

1.6 Thesis Outline

This thesis comprises seven chapters.

Chapter 1, titled "Motivation and Background," described the research motivation, background, related previous studies, and the scope of this thesis.

Chapter 2, titled "Technology Overview," explains several fundamental technologies utilized in this thesis, with broad overviews of related topics. Specifically, this chapter aims to give explanations about "single-cell analysis in microfluidics," "O_2 sensing with fluorescence lifetime imaging microscopy," and "deep-learning-based automated image analysis."

Chapter 3, titled "Versatile System for Microbial Growth Analysis under Controlled Oxygen," describes the first development of an easy-to-use mini-incubator and microbial analysis platform under controlled O_2 conditions. The comprehensive experimental platform comprising of (i) on-chip cultivation and online control of O_2 in-flow, (ii) online O_2 monitoring by fluorescence lifetime imaging, and (iii) time-lapse microscopy for automated image acquisition and subsequent deep-learning-based image analysis, offers a wide variety of researchers a solution to implement O_2 control into various formats of microfluidic experiments. This chapter is based on a published journal paper (Kasahara *et al.*, *Frontiers in Microbiology*, 2023).

Chapter 4, titled "Double-Layer Microfluidics for Recreating Rapid Oxygen Oscillations," describes a novel microfluidic platform enabling microbial growth investigation under rapidly changing O_2 conditions. The growth dynamics of the facultative anaerobe *Escherichia coli* (*E. coli*) MG1655 is investigated under O_2 oscillations occurring within seconds to minutes. A double-layer microfluidic chip is developed to facilitate rapid gas exchange within the cultivation chambers and frequent data acquisition accompanied by time-lapse microscopy to analyze cell division at the single-cell resolution. The microfluidic chip, automated time-lapse microscopy, and deep-learning-based image analysis compose a versatile platform to analyze microbial growth and its correlation to applied O_2 oscillations. The platform was employed to cultivate *E. coli* under well-defined O_2 oscillating environments with varying oscillation periods to examine cellular adaptation in a time-resolved manner. Periodically oscillating microbial growth dynamics composed of several adaptation phases and synchronized with applied O_2 oscillations are reported. This chapter is based on a published journal paper (Kasahara *et al.*, *Lab on a Chip*, 2025).

Chapter 5, titled "Investigating Growth of *C. glutamicum* under Oscillating Oxygen Environments," describes an investigation of aerobic and anaerobic growth of *Corynebacterium glutamicum (C. glutamicum)* using the developed double-layer microfluidic platform. The growth and adaptation of *C. glutamicum* is examined under oscillating O_2 environments. The results from this chapter serve as a case study where the microfluidic device developed in Chapter 4 can be utilized to investigate different types of microorganisms (*E. coli* and *C. glutamicum*). A short "Introduction" section is provided to help readers follow the chapter easily.

Chapter 6, titled "Microfluidic Chip Development for Spatial Oxygen Control," describes a series of microfluidic designs for spatial control of O_2 microenvironments. Various designs are examined to enable replicating spatially controlled O_2 microenvironments and to achieve high-throughput analysis. The primary focus of this chapter is on explaining O_2 control principles, chip fabrication, and preliminary O_2 control experiments.

Chapter 7, titled "Conclusions and Outlook," lastly concludes the thesis and discusses future improvements and applications of this thesis.

Chapters 3, 4, and 6 mainly describe the development of experimental setups. Therefore, these chapters include a "Technical Concept" section to explain the motivation and concept behind the development. This is followed by "Materials and Methods," "Results," and "Discussion." Some contents are repeatedly explained in several chapters for better clarity.

2 Technology Overview

This chapter provides an overview of the technologies and principles underpinning this thesis. Specifically, it discusses (1) single-cell analysis in microfluidic environments, (2) O_2 sensing using fluorescence lifetime imaging microscopy, and (3) deep learning-based automated image analysis.

2.1 Single-Cell Analysis in Microfluidics

Single-cell analysis has become an essential method for investigating unique characteristics and physiological states of individual cells within a population, insights often neglected in bulk assays that report population averages [72, 73]. This approach allows researchers to examine cellular systems in greater detail, uncovering heterogeneity within cell populations and providing a deeper understanding of cellular complexity. Recently, microfluidic systems have been integrated for single-cell analysis, allowing manipulation of small-volume samples (sorting, isolation, trapping of individual cells) on a single device based on various strategies such as microwells, micro patterns, droplets, cytometry, and so on [74–76].

To examine spatiotemporal dynamics of individual cell behavior in confined environments, a practical approach involves trapping cells in microgrooves or microchambers, cultivating them, and performing time-lapse imaging [63, 77–79]. Microstructures are commonly fabricated using soft lithography, a series of techniques to replicate microstructures from a master mold onto soft polymers [80, 81]. Typically, these master molds are prepared via photolithography, where several spin-coated photoresist layers on a silicon wafer are micropatterned by light exposure through photomasks, as depicted in Fig. 2.1. PDMS is widely used to replicate these micropatterns of master molds due to its advantages, including biocompatibility, high gas permeability (diffusion coefficient for $O_2 \approx 10^{-9}\ \mathrm{m^2\ s^{-1}}$), optical transparency, and access to microenvironmental control [82,

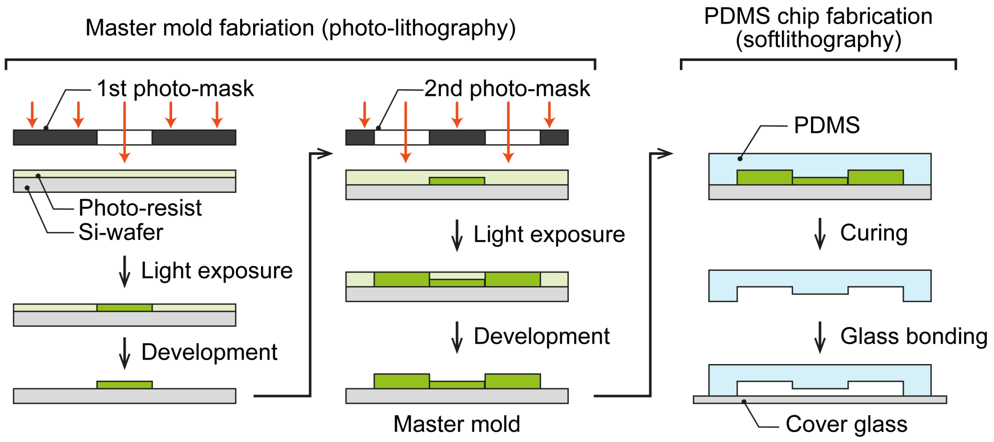

Figure 2.1: schematics of photo-lithography and soft lithography for PDMS-based microfluidic chip fabrication.

83]. These characteristics make PDMS suitable for applications in biological cell culture and optical microscopy.

In microfluidic grooves or chambers designed for microbial single-cell analysis, cell growth is confined to a one- (1D) or two-dimensional (2D) monolayer, providing an optimal focal plane for optical microscopy throughout the cultivation process and subsequent single-cell segmentation tasks (Fig. 2.2). Depending on the organism to be cultured, the resulting chamber height can be specified by adjusting the photoresist thickness of the spin-coated photo-resist layer during master mold fabrication. This technology has previously been employed to investigate cell growth characterization under various conditions, including constant [78, 84] and oscillating environments [65, 66], spatially structured chemical gradients [63, 85], and the mechanisms governing cell division [77, 79].

A microfluidic design with 2D chambers is employed throughout this thesis. A microfluidic chip holds multiple chambers for high-throughput investigation. Cultivation chambers are arranged in series, interconnected by two common fluid supply channels. During the cultivation phase, the volume flows in the parallel supply channels are equal. Therefore, no pressure difference and, thus, no convective flow is induced inside the growth chambers. As a result, mass transfer between the supplied medium and the growth chamber is governed by diffusion, and the cells are not affected by shear forces [86]. The chip is fixed on microscopy for simultaneous cultivation and time-lapse imaging.

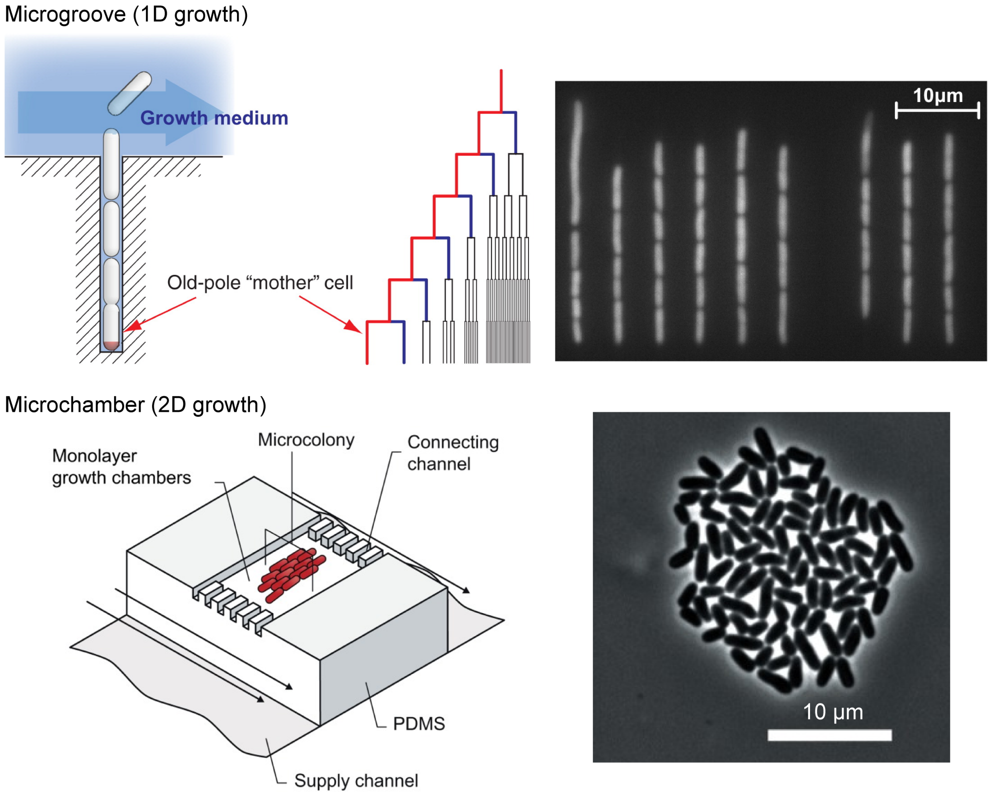

Figure 2.2: Microbial single-cell analysis using microfluidic grooves and chambers (adapted with permission from [84] and [78]).

2.2 Oxygen Sensing with Fluorescence Lifetime Imaging Microscopy

Since microfluidic culture chips contain micrometer-sized growth chambers, conventional sensors with external settings cannot be integrated to measure O_2. Therefore, novel bottom-up approaches have been developed. The focus of earlier work was on Clark-type electrode sensors that measure O_2 by detecting a current flow [87, 88]. Although these sensors were miniaturized to be integrated into microscale devices [89], they still suffered from self-consumption of O_2, contamination in contact with samples, and complexity in designing electrical connections [90].

Optical O_2 sensors attracted more attention as a candidate suitable for O_2 measurement in microfluidics. These sensors use O_2-sensitive fluorescent probes that quench in

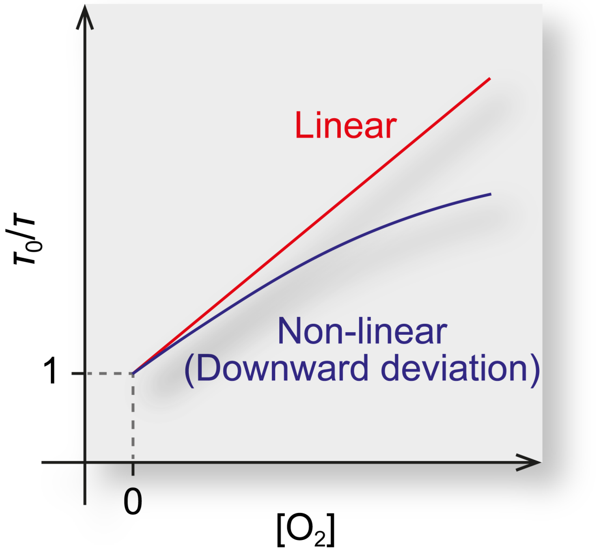

Figure 2.3: Stern-volmer plot illustrating linear relationship (red) and non-linear relationship with downward deviation (blue).

the presence of O_2. The degree of quenching can be measured as the change in fluorescence intensity or lifetime, which follows the Stern-Volmer Equation (red line depicted in Fig. 2.3).

$$\frac{I_0}{I} = \frac{\tau_0}{\tau} = 1 + K_q f_{O_2} \tag{2.1}$$

I and τ represent fluorescence intensity and lifetime, respectively. K_q represents the Stern-Volmer quenching constant. f_{O_2} represents fractional O_2 saturation in solution, defined as the ratio of the dissolved O_2 concentration to the saturation concentration under pure O_2 (100%) at the same temperature and pressure. The subscript 0 represents the values at an O_2 saturation of 0%. The optical O_2 sensors can easily be implemented into microfluidic devices in various formats (thin sensor film, micro/nanoparticles, solution), providing accurate, real-time, and spatial O_2 detection without self-consumption issues. Leveraging these advantages, fluorescence intensity-based measurements were widely integrated into microfluidics [91–93]. The intensity-based approach, however, can be affected by variations in light source intensity, environmental conditions, and photobleaching, resulting in inaccurate O_2 measurements. To reduce these effects, an approach based on Förster resonance energy transfer (FRET) and ratiometric measurements was also presented [94].

Contrarily, fluorescence lifetime imaging microscopy (FLIM) is independent of the dye concentration, providing more robust and accurate O_2 measurements compared to intensity-based and ratiometric approaches [95]. By performing FLIM in the frequency domain and in combination with a dedicated microscope camera, O_2 can be imaged with spatial and temporal resolution during live-cell microscopy on a microfluidic device [48, 96, 97]. A linear relationship in Equation 2.1 holds for many cases; however, certain circumstances can positively/negatively deviate the plot, leading to a non-linear Stern-Volmer plot (Fig. 2.3). Specifically, it was explained in previous research that fluorescence quenching at a microscopic level is complex due to a small sampling volume and resulting heterogeneity in the presence or absence of a quencher, which makes the Stern-Volmer plot curving downward [98]. It was also pointed out that a highly concentrated sample showed a non-linear relationship negatively deviating from the Stern-Volmer plot [99]. In such cases, a modified Stern-Volmer equation is applied to rationalize the downward curvature (blue line depicted in Fig. 2.3) [98–102].

$$\frac{I_0}{I} = \frac{\tau_0}{\tau} = \frac{1 + K_q f_{O_2}}{1 + K_q f_{O_2} - \alpha K_q f_{O_2}} \tag{2.2}$$

α denotes the fraction of accessible fluorophore. In this thesis, a water-soluble ruthenium dye, tris(2,2'-bipyridyl) dichlororuthenium(II) hexahydrate (RTDP), is used to determine on-chip O_2 concentrations using FLIM. O_2 concentration in a mixed gas is expressed as a volumetric concentration in percentage. Dissolved O_2 concentration in solution is expressed either as percentage or fraction relative to pure O_2.

2.3 Deep Learning-Based Automated Image Analysis

Automated image analysis powered by deep learning (DL) has emerged as a transformative approach in microbial cultivation. It enables high-throughput monitoring and analysis of microbial growth by leveraging advanced computational techniques to interpret images of microbial colonies, substantially enhancing the efficiency and accuracy of microbiological research.

The image analysis performed in this thesis is a seamless procedure integrating a re-

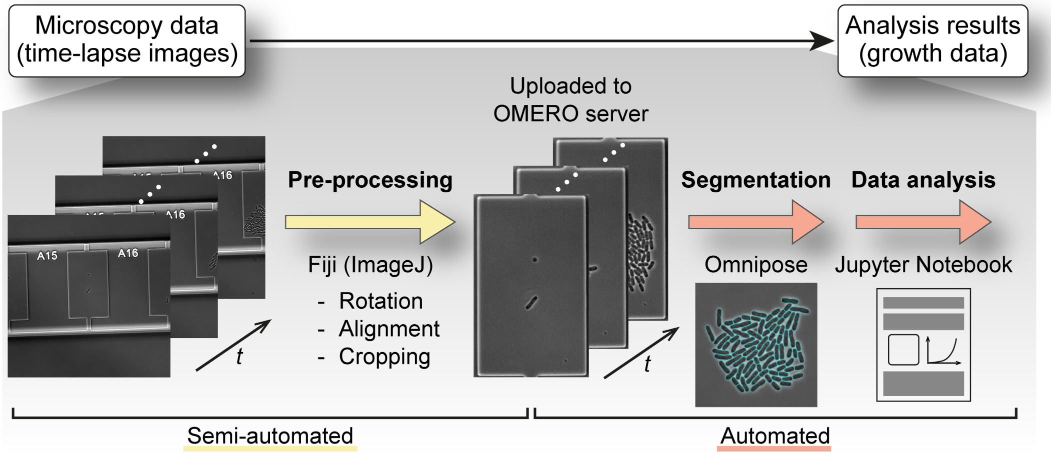

Figure 2.4: Procedure of image analysis.

cently developed cell annotation tool and segmentation model, as shown in Fig. 2.4 [103, 104]. Acquired microscopy data in nd2 format is exported as tiff files and pre-processed using Fiji [105], which included rotation, alignment (Correct 3D Drift [106]), and cropping. These procedures are done semi-automated, using a custom macro for Fiji. The pre-processed TIFF files are then uploaded to the Open Microscopy Environment Remote Objects (OMERO) server [107] for subsequent analysis. For the automated image analysis, Jupyter Notebooks are developed based on Python to perform deep-learning-based cell segmentation (Omnipose [108]), followed by filtering artifacts and extracting single-cell sizes. These Jupyter Notebooks are designed for a single time-lapse recording and provide video rendering to guarantee and document sufficient cell segmentation quality. The same Jupyter Notebooks are repeatedly applied to all the time-lapse images (scaling analysis), leading to fully automated image processing such that experiment results are obtained overnight.

3 Versatile System for Microbial Growth Analysis under Controlled Oxygen

Microfluidic cultivation devices that facilitate O_2 control enable unique studies of the complex interplay between environmental O_2 availability and microbial physiology at the single-cell level. This chapter describes a comprehensive experimental approach to allow spatiotemporal single-cell analysis of living microorganisms under controlled O_2 availability. To this end, a gas-permeable polydimethylsiloxane microfluidic cultivation chip and a low-cost 3D-printed mini-incubator were successfully used to control O_2 availability inside microfluidic growth chambers during time-lapse microscopy. Dissolved O_2 was monitored by imaging the fluorescence lifetime of the O_2-sensitive dye RTDP using FLIM microscopy. The acquired image data stacks from biological experiments, containing phase contrast and fluorescence intensity data, were analyzed using in-house developed and open-source image analysis tools. The resulting O_2 concentration could be dynamically controlled in the range between 0% and 100%. The system was experimentally tested by culturing and analyzing an *Escherichia coli* strain expressing green fluorescent protein as an indirect intracellular O_2 indicator. The presented system allows for innovative microbiological research on microorganisms and microbial ecology with single-cell resolution. Part of the results in this chapter were published in Kasahara *et al.*, *Frontiers in Microbiology*, 2023.

3.1 Technical Concept

An experimental system for controlling O_2 during microbial single-cell analysis has been developed (Fig. 3.1). The system includes (A) O_2 control with microfluidic cultivation inside a 3D printed mini-incubator, (B) O_2 sensing using an O_2 -sensitive dye RTDP and FLIM, and (C) an automated image analysis procedure based on deep learning (Fig. 3.1).

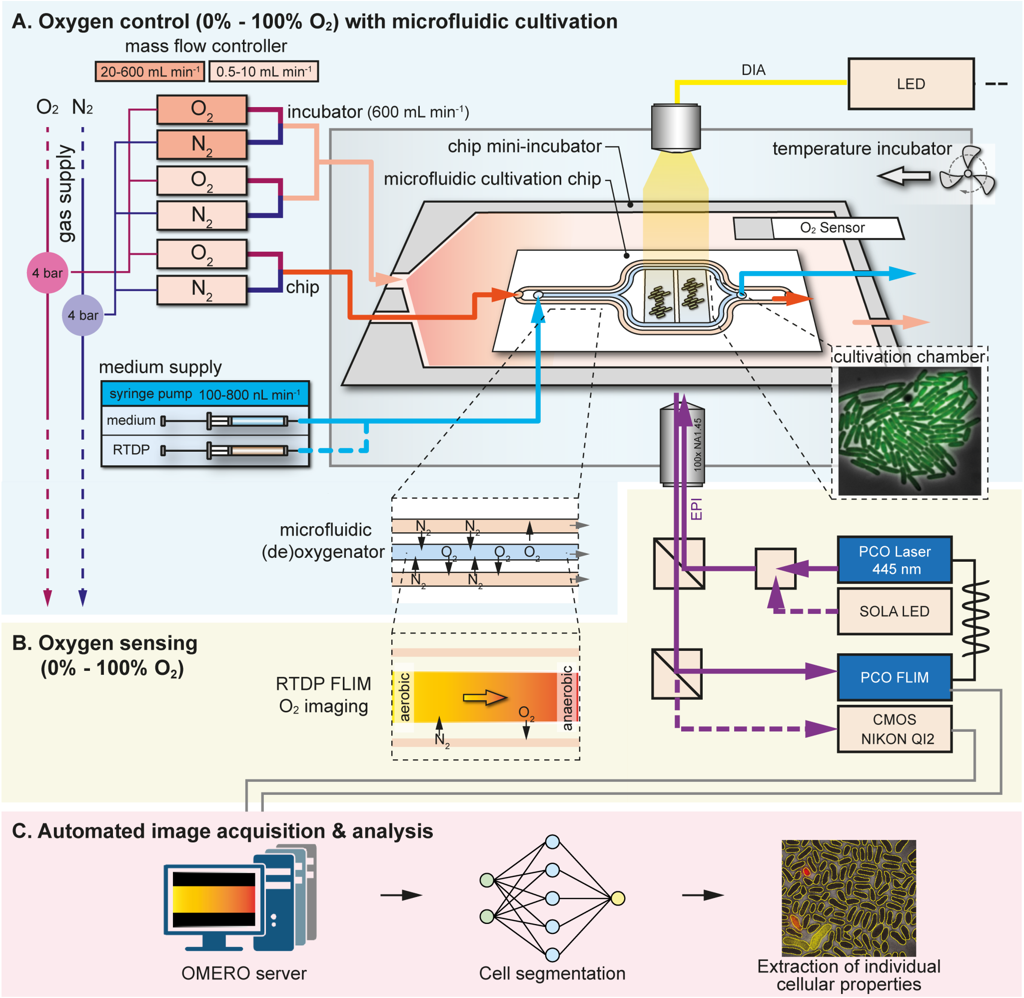

Figure 3.1: Overview of the microfluidic cultivation system for spatiotemporal microbial single-cell analysis under controlled O_2 environments. **(A)** O_2 control was achieved by using a microfluidic chip inside a 3D printed mini-incubator over the range of 0% - 100%. **(B)** O_2 sensing with spatial and temporal resolution was implemented by imaging the fluorescence lifetime of the O_2-sensitive dye RTDP. **(C)** Automated image acquisition and analysis was performed with special software tools.

(A) Microfluidic Chip and O_2 control with 3D-Printed Mini-Incubator

A new microfluidic chip with the required channel layout was designed to allow the on-chip control and simultaneous cultures (Fig. 3.2A). The fluid channel (blue) is sandwiched between two adjacent gas channels (red). All supply channels are 100 μm wide and 10 μm deep. As shown in Fig. 3.2A (i, ii), each channel comprises (i) a (de)oxygenator zone, followed by (ii) a cultivation zone with 80 cultivation chambers, allowing a statistically reliable number of microbial populations to be imaged during a single experiment.

A 100 μm thick PDMS wall acts as a gas-permeable membrane between the fluid and adjacent gas channels. The height of a cultivation chamber is 1 μm, and the surface area = 50 μm × 30 μm, resulting in a volume of a single cultivation chamber of 1.5 pL. The height of the chamber corresponds to the diameter of a typical *E. coli* cell thereby restricting cell growth to a defined monolayer (Fig. 3.2A (iii)). As all gas channels are interconnected, only a single gas inlet and outlet port is required for on-chip gas flow, which results in uniform O_2 levels across the chip. In addition, all cultivation channels are equipped with adjacent gas channels on either side, creating a homogeneous O_2 distribution across the cultivation zone.

For illustration purposes, the microfluidic channels of the fabricated chip were visualized by the infusion of red and blue dye, as shown in Fig. 3.2B. The chip contains three parallel culture channels, allowing three simultaneous cultures during a single experiment. The scanning electron microscope images of the fabricated chip show (i) the (de)oxygenator structure with the fluid channel in the center and the adjacent gas channels at the sides and (ii) the cultivation chamber with the rectangular structure and two connections to the fluid supply channels (Fig. 3.2C).

The 3D printed mini-incubator was utilized to deliver a continuous gas flow of the desired O_2/N_2 composition over the PDMS chip. Due to the high gas permeability of PDMS, as explained in Chapter 2, it facilitates efficient gas exchange by diffusion across the entire chip surface. When the chip was operated without the incubator, anaerobic conditions were impossible due to uncontrolled O_2 influx from the surrounding laboratory atmosphere. Thus, the mini-incubator enables cultures without O_2 when 100% N_2 was supplied continuously, and undesired influx was prevented.

Gas flow was controlled using four interconnected mass flow controllers (O_2 0.5 - 10 mL/min, O_2 20 - 600 mL/min, N_2 0.5 - 10 mL/min and N_2 20 - 600 mL/min) to automatically mix O_2 and N_2 in desired ratios before flushing into the microfluidic chip and mini-incubator. The mini-incubator was operated at a total gas flow of 600 mL/min, and a gas flow of 10 mL/min was delivered through the microfluidics. In the microfluidic chip, gas exchange was assisted with the (de)oxygenator structure, facilitating gas

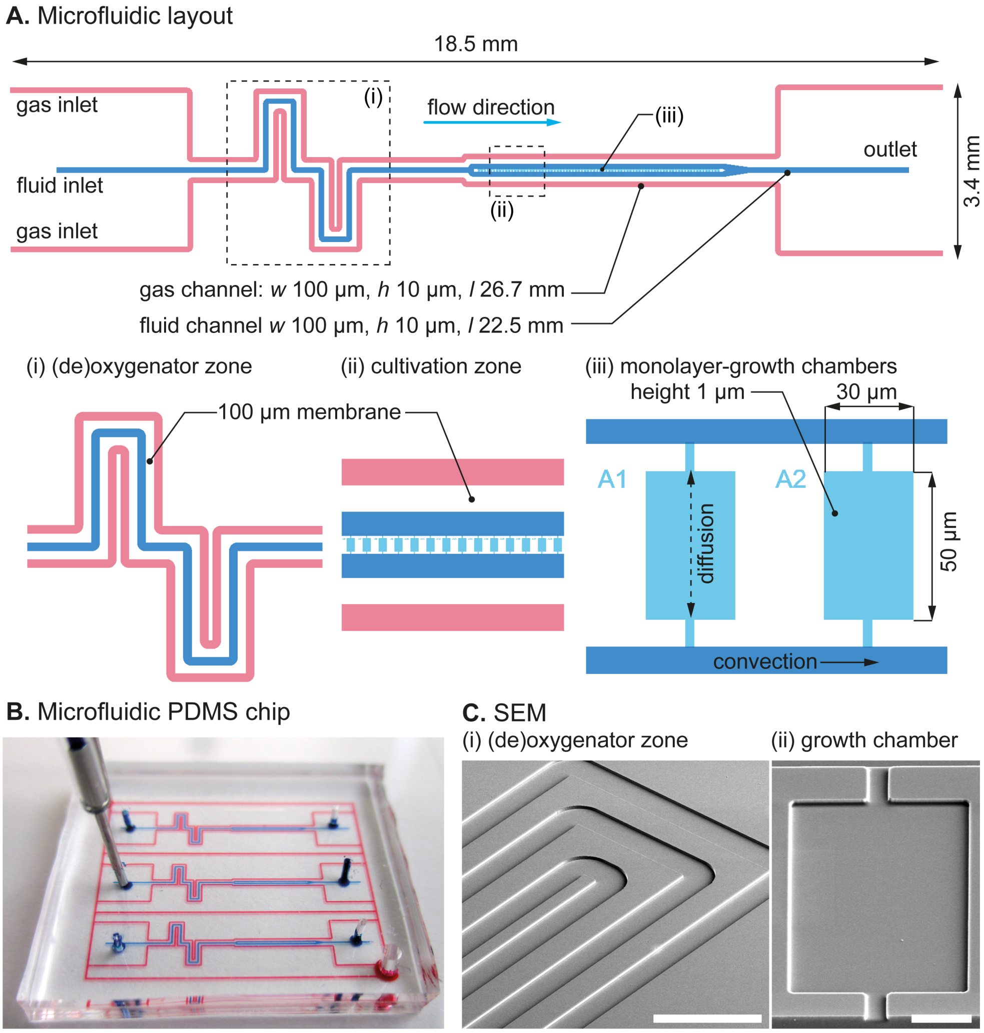

Figure 3.2: Detailed design of the microfluidic chip. **(A)** Layout of the microfluidic channels, with details of the (i) (de)oxygenator zone and (ii) cultivation zone with (iii) growth chambers. **(B)** Photograph of the fabricated microfluidic PDMS chip. The chip is the size of a typical postage stamp. For visualization, the gas and fluid channels were colored with red and blue ink. **(C)** SEM images of the microfluidic (i) (de)oxygenator structure (scale bar = 300 μm) and (ii) growth chamber (scale bar = 20 μm).

diffusion between the fluid and the adjacent gas channels across the PDMS membranes in-between, as shown in Fig. 3.1A. The syringe pump delivered either the RTDP solution during on-chip O_2 sensing or the culture medium during single-cell analysis at a flow rate of 400 nL/min. The RTDP-based O_2 sensing was not performed simultaneously with the microbial single-cell analysis but was used separately to characterize the device's performance.

(B) O_2 Sensing

Dissolved O_2 in the fluid channel was determined by camera-based fluorescence lifetime imaging of the O_2-sensitive dye RTDP (Fig. 3.1B). A growth medium was provided continuously during microbial cultures to maintain stable culture conditions. Growth chambers were arranged behind the (de)oxygenator structure to allow sufficient residence time and, thus, gas-exchange time of the fluid. This allowed the cells to be supplied with (de)oxygenated medium and cultured at the desired O_2 concentrations. Phase contrast and fluorescence intensity images were obtained using the conventional complementary metal-oxide-semiconductor (CMOS) camera.

(C) Deep-Learning Based Automated Image Analysis

After microfluidic cultivation and continuous image acquisition from multiple chambers, the data can be large, making manual handling of the data time-consuming and difficult. Therefore, the acquired image sequences were processed with an in-house developed automated image analysis platform to extract interesting cellular properties such as cell number, area, and fluorescence intensity to determine growth rates and cellular activities. Cellular properties can be extracted for each cell in the culture chambers, providing detailed information at the single-cell level. (Fig. 3.1C).

3.2 Materials and Methods

3.2.1 Microfluidic Device Fabrication

The microfluidic cultivation chip was fabricated following a two-layer soft lithography. Briefly, a 100 mm silicon wafer was subsequently coated with two layers of the photoresist SU-8 (Microchemicals GmbH, Germany) and structured by photolithography (Helmholtz Nano Facility, Germany [109]). The masks for the photolithography were designed with the layout editor Clewin5 (WieWeb software, The Netherlands).

The fabricated silicon wafer containing the SU-8 structure served as the mold for the following PDMS casting step. 50 g of a PDMS mixture (Sylgard 184 Silicone elastomer kit, Dow, US) was prepared by thoroughly mixing the monomer base with the crosslinker in a ratio of 10:1, resulting in a homogeneous and opaque highly viscous mixture. This mixture was then degassed in a desiccator at 200 mbar under pressure for 1 h to remove any air bubbles. The resulting fully transparent PDMS mixture was poured over the silicon wafer mounted in a typical petri dish. Thermal curing was then performed at 80°C for at least 1 h. The crosslinked PDMS slab was manually peeled from the silicon mold and cut into single chips. Then, inlets and outlets for the fluid and the gas flow connections were manually punched using a punching tool (ϕ = 0.75 mm, World Precision Instruments, US). Single PDMS chips were finally bonded to glass substrates (D263®Bio, 39.5 mm × 34.5 mm × 0.175 mm, Schott AG, Germany) after an O_2 plasma treatment (Femto Plasma Cleaner, Diener Electronics, Germany) for 25 s.

3.2.2 Gas and Fluid Flow Control

Mass flow controllers, calibrated for two different mass-flow ranges (0.5 - 10 mL/min and 20 - 600 mL/min, red-y, Vögtlin Instruments GmbH, Switzerland), and the gasses O_2 and N_2, were used to mix the gas at desired O_2 and N_2 ratios (gas supply pressure: $p = 4$ bar). A mini-incubator (50.0 × 82.0 × 18.0 mm) was designed using computer-aided design (CAD, Solidworks, Dassault Systems, France) and fabricated by 3D printing as illustrated in Fig. 3.3A and B (Original Prusa i3 MK3S, Prusa Research, Czech Republic). The O_2 concentration inside the mini-incubator was continuously measured by an inserted laboratory-scale O_2 sensing probe (VisiFerm mA 120 H3, Hamilton, US). The 3D CAD and printing files are available as supplemental material. Fluid flow was controlled using a syringe pump (neMESYS, CETONI, Germany) to continuously deliver the sensor solution and culture medium.

3.2.3 Microscopy Setup

Microfluidic cultures and O_2 imaging were performed on an inverted and automated live-cell microscope (Nikon Eclipse Ti-E 2, Nikon, Japan) equipped with a 20 × objective (Plan Apo λ, Nikon, Japan), a 100 × objective (Plan Apo λ Oil, Nikon, Japan), and the perfect focus system (PFS) for focus drift compensation during time-lapse imaging. The setup was equipped with two digital cameras, which can be used sequentially during time-lapse imaging. A CMOS camera (DS-Qi2, Nikon, Japan) was installed in the

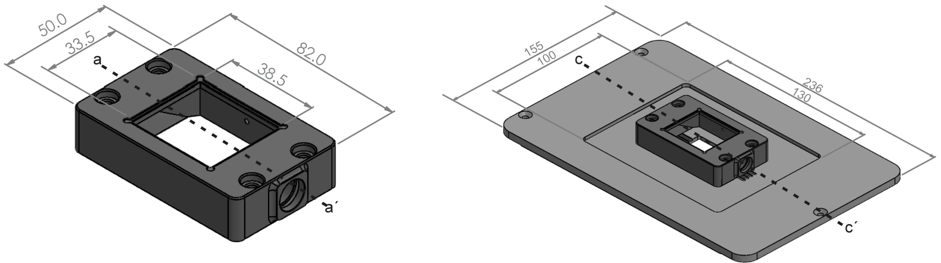

A. 3D-printed mini-incubator

C. Mini-incubator on microscope stage

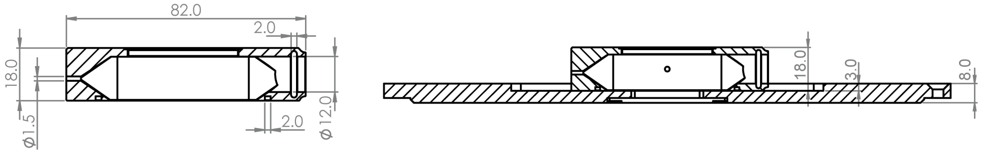

B. Cross sectional view (a - a´)

D. Cross sectional view (c - c´)

Figure 3.3: Detailed design of the mini-incubator. **(A)** Dimensions of the mini-incubator. **(B)** Cross-sectional view of the mini-incubator (a - a'). Dimensions are in mm. **(C)** Dimensions of the mini-incubator mounted on the customized chip holder fitting into the microscope stage. **(D)** Cross-sectional view (c - c').

right microscope port to record phase-contrast and wide-field fluorescence images. The fluorescence excitation light was supplied by a solid-state white light excitation source (SOLA Light Engine, Lumencor, US) and a fluorescence filter cube (GFP-3035D, Nikon, Japan).

The special FLIM camera (550 kHz frequency domain, pco.flim, PCO AG, Germany) connected to the modulated excitation laser (445 nm, 100 mW, pco.flim laser, Omicron-Laserage Laserprodukte GmbH, Germany) was mounted to the left microscope port. A customized filter cube with an excitation filter = 440/40 (F47-440, AHF analysentechnik AG, Germany), a dichroic mirror = 495LP (F48-495, AHF analysentechnik AG, Germany), and an emission filter = 605/70 (F47-605, AHF analysentechnik AG, Germany) was used for FLIM. The microscope setup was also surrounded by a temperature incubator (Okolab, Italy), ensuring stable cultivation temperature. A customized chip holder fitting into the motorized X-Y-stage was used to mount the microfluidic chip and the 3D-printed mini-incubator, as illustrated in Fig. 3.3C and D.

Table 3.1: LB medium composition. All the chemicals were bought from Carl Roth, Germany. The pH was adjusted to 7.0 with NaOH. The solution was autoclaved at 121°C for 20 min, then stored at 4°C.

Component	Concentration [g/L]
Peptone	10
Yeast extract	5
NaCl	10

3.2.4 Microbial Cultures

E. coli MG 1655 carrying the vector pVWEx-1-gfpUV and a kanamycin resistance gene was used for microbial growth experiments. Green fluorescent protein (GFP) expression in the *E. coli* strain was induced by the addition of 0.1 mM isopropyl β-D-1- thiogalactopyranoside (IPTG, Carl Roth, Germany). Microbial cultures were performed according to the following procedure. The primary preculture was performed in a complex lysogeny broth (LB) medium (Table 3.1). For all subsequent culture steps, defined minimal M9 medium supplemented with 2% glucose (Carl Roth, Germany), 2% casamino acid (VWR, US), and 50 μg/mL kanamycin (Carl Roth, Germany) was used (Table 3.2). First, a shake flask containing 15 mL of LB medium was inoculated with a single colony from an agar plate and cultured at 37°C and 150 rpm for approximately 8 h. The second preculture containing M9 minimal medium was inoculated from the primary culture, with an initial optical density measured at a wavelength of 600 nm (OD_{600}) of 0.05, and cultivated overnight at 30°C, 120 rpm. The final shake flask culture was inoculated from the second preculture with initial OD_{600} = 0.3 and cultivated at 30°C and 120 rpm until the culture reached the logarithmic growth phase. Cells derived from the log phase culture were seeded into the growth chambers of the microfluidic chip.

3.2.5 FLIM Calibration for on-Chip O_2 Sensing

Prior to the fluorescence lifetime imaging (FLIM), a calibration measurement must be performed with a reference slide containing a fluorescent dye with a known and stable lifetime (lifetime = 3.75 ns, UMM-SFG, Starna Scientific, UK). This calibration is required to correctly determine the lifetime from unknown samples, in this case, the life-

Table 3.2: Defined M9 medium composition. All the chemicals were bought from Carl Roth, Germany. The pH was adjusted to 7.0 with NaOH. The solution was autoclaved at 121°C for 20 min, then stored at 4°C.

Component	Concentration
Defined M9 medium [g/L]	
$Na_2HPO_4 \cdot 2\,H_2O$	7.53
KH_2PO_4	3.00
NaCl	0.50
NH_4Cl	1.00
$MgSO_4 \cdot 7\,H_2O$	0.25
$CaCl_2 \cdot 2\,H_2O$	0.15
Trace elements (1000X)	1 mL/L
Trace elements (1000X) [mM]	
$(NH_4)_6Mo_7O_{24} \cdot 4\,H_2O$	0.003
H_3BO_3	0.4
$CoCl_2 \cdot 6\,H_2O$	0.03
$CuSO_4 \cdot 5\,H_2O$	0.01
$MnCl_2 \cdot 3\,H_2O$	0.8
$ZnSO_4 \cdot 7\,H_2O$	0.01

time of the O_2-sensitive dye RTDP. The calibration procedure must be performed every time the laser is shut down or operated at a different frequency.

For O_2 sensing inside the microfluidic chip, 5 mg/mL of RTDP solution (Acros Organics, Belgium) dissolved in Milli-Q water (Merck Millipore, US) was used. The prepared RTDP solution was protected from light until use. The fluorescence of RTDP is quenched in the presence of O_2 according to the Stern-Volmer equation (Eq. 2.1).

First, the RTDP solution must be calibrated at two known O_2 concentrations, at 0% O_2 giving τ_0, and at, for example, 100% O_2 to derive K_q. In practice, however, the calibration procedure at 0% O_2 can be challenging because it requires an anoxic sensor solution. Several methods have been demonstrated, for example, using a droplet of the sensor surrounded with 100% N_2 gas or consuming O_2 by adding an O_2 scavenging chemical to the solution [96, 110]. However, none of these methods were compatible with the proposed approach.

Here, the calibration was performed at 0% O_2 using a gas-tight glass syringe connected to a glass capillary filled with an anoxic RTDP solution to determine τ_0. The RTDP solution and the syringe were prepared entirely in the anaerobic workbench. Briefly, the solution was gassed with N_2 for at least 1 h in the anaerobic workbench, then filled into a gas-tight glass syringe (1.0 mL, ILS, Germany) to ensure an anoxic solution (Fig. 3.4A). The syringe was connected to a glass capillary (75 µm inner diameter, 375 µm outer diameter, 700 mm length, Molex, US), which was then manually flushed with the anoxic RTDP solution. Before the assembly, 10 mm of the polymer coating was removed in the middle of the capillary using a flame and acetone to prepare an optical detection window for FLIM. The assembled syringe, including the capillary, was taken out of the anaerobic workbench, fixed above the objective on a suitable specimen holder, and the capillary end was connected to a waste container and flushed continuously at 400 nL/min using the syringe pump. Then, FLIM was performed to determine τ_0.

Furthermore, the RTDP solution was calibrated at 100% O_2 inside the microfluidic chip by using the on-chip microfluidic gas flow combined with the continuous gas flow through the mini-incubator at 100% O_2 to determine $\tau_{100\%}$ (Fig. 3.4B). Briefly, the fluid channel was connected to a syringe (Omnifix®F Solo 1mL, Braun, Germany) via polytetrafluoroethylene (PTFE) tubing (0.5 mm inner diameter, 1.6 mm outer diameter, Chromatographie Service GmbH, Germany) and the RTDP solution was delivered at 400 nL/min. Gas flow was maintained at 100% O_2 for several hours until the O_2 diffusion reached equilibrium and a steady-state lifetime sensor output and $\tau_{100\%}$ was determined. The obtained τ_0 and $\tau_{100\%}$ were used to calculate the K_q value in Eq. 2.1.

Calibration was performed at two different temperatures (T = 25°C and 30°C). As is clear, the fluorescence lifetime of RTDP also varies with temperature. Therefore, calibration, measurement, and microbial cultures should all be conducted at the same temperature.

The following lifetime values were determined during calibration. At 25°C, τ_0 = 573 ns and $\tau_{100\%}$ = 160 ns, whereas at 30°C, τ_0 = 526 ns and $\tau_{100\%}$ = 144 ns. Using Eq. 2.1, K_q was calculated as 2.58 at T = 25°C and 2.65 at T = 30°C (Fig. 3.4C and D). Using these K_q values and Eq. 2.1, the measured O_2 concentrations could be calculated from the measured fluorescence lifetimes.

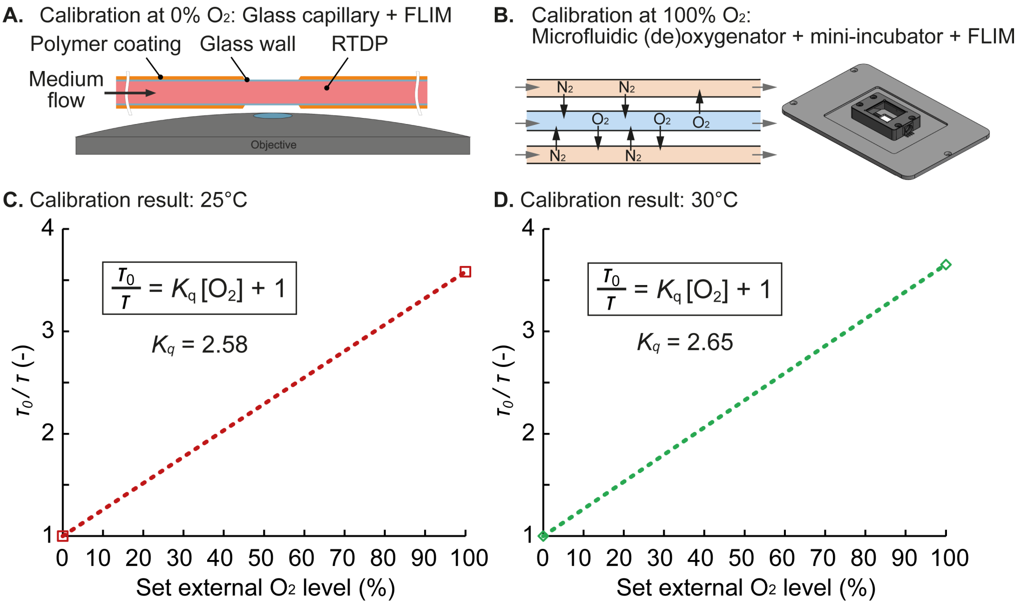

Figure 3.4: Setup for FLIM calibration of RTDP. **(A)** Calibration at 0% O_2 level using the glass capillary. **(B)** Calibration at 100% O_2 level using the microfluidic (de)oxygenator and the mini-incubator. **(C)** Calibration plot of RTDP solution at 25°C, fitted with Stern-Volmer equation. **(D)** Calibration plot of RTDP solution at 30°C, fitted with Stern-Volmer equation.

3.2.6 Microfluidic Cultivation and Time-Lapse Imaging

A cell suspension was prepared using cells harvested from the logarithmic growth phase of the final shake flask culture and diluted to an $OD_{600} = 0.35$. Cells were then seeded into the microfluidic cultivation chambers by delivering the cell suspension into the fluid channel by applying gentle pressure to the syringe while visually inspecting the seeding performance. After sufficient chambers were seeded with cells, M9 medium was used to rinse residual cells from the supply channels. M9 medium containing 0.1 mM IPTG was then continuously delivered at a flow rate of 400 nL/min. Time-lapse phase contrast and fluorescence images were taken every 5 min during the cultivation. Optimal illumination and camera exposure times were experimentally derived for each setup.

In the case of the anaerobic microfluidic cultivation, cell inoculation was performed entirely inside the anaerobic workbench to ensure complete isolation of the cells from

O_2, but without the ability to follow the seeding process by microscopy. After seeding, the glass syringe filled with an anaerobic M9 medium containing 0.1 mM IPTG was connected to the fluid inlet. The entire cultivation setup, including the syringes, the chip, and the mini-incubator, was assembled inside the anaerobic workbench. Finally, the prepared setup was removed from the anaerobic workbench and mounted on the microscope stage. The temperature inside the temperature incubator was maintained at 30°C.

3.2.7 Automated Image Analysis

The recorded phase contrast and fluorescence time-lapse image sequences from biological experiments were analyzed to extract the individual intracellular fluorescence intensities. As the image sequences contained more than $50k$ individual cells, the image processing was done partly automatically using DL segmentation in Jupyter Notebooks and Python [104]. First, the acquired time-lapse sequences were cropped into single cultivation chambers, aligned with Fiji, and stored in an OMERO instance [107]. A pre-trained Omnipose [108] segmentation model was applied to extract the contour of individual cells followed by a border filter eliminating segmentation artifacts closer than 0.5 μm to the image borders. The fluorescence signal for every cell is computed by averaging the fluorescence channel intensities inside every segmented cell contour.

After cell segmentation, cell tracking was performed using the activity prioritized method [111] to explore the distributions of the fluorescence intensities inside every segmented cell contour over the cell generations. The cell lineages were computed using the default parameters of the cell tracker, utilizing the Omnipose segmentation model. Starting from the initially present cell, assigned with generation "zero," the daughter cells gain one generation after every recorded division event. The analysis was performed for the fixed time point for each data set. The cell segmentation and tracking code is available at `https://github.com/JuBiotech/Supplement-to-Kasahara-et-al.-2023a`.

3.3 Results

3.3.1 O_2 Control and Sensing

A sequential step test was performed (at T = 25°C and 30°C) during O_2 control to characterize the dynamical performance of the setup. Therefore, a switching sequence was programmed using an in-house written LabView tool controlling the four mass flow controllers. The O_2 / N_2 ratio of the gas mixture was then changed automatically to generate desired O_2 concentrations in the fluid flow. The RTDP solution was delivered continuously through the fluid channel, while the gas flow composition through the gas channels and the mini-incubator was set to 0%, 2%, 4%, 6%, 8%, 10%, 15%, 21%, and finally to 100% O_2 over 30 hours. The initial sensing phase at 0% O_2 was maintained for 4 h to ensure anoxic starting conditions. Then, the gas composition was altered every 3 hours. During FLIM, the RTDP solution was continuously delivered at 400 nL/min. The O_2 concentration inside the mini-incubator rapidly followed the desired values, and changes were performed with negligible delay, as evident from the O_2 sensor readings from the Hamilton probe installed inside the mini-incubator (data not shown).

Time-lapse images of the fluorescence lifetime were taken every 5 minutes at two successive regions of interest (ROI) before and after the (de)oxygenator as shown in Fig. 3.5A (ROI 1 and 2). The acquired image sequences from FLIM were processed with Fiji to determine the average lifetime of each image, as these images tend to have some noise at the level of individual pixels.

From the representative false-color images determined for each O_2 concentration at T = 30°C (here ROI 1, Fig. 3.5B), it is visible that FLIM delivered lifetime images, revealing homogeneous O_2 availability in the channel. The lifetime decreased with the increasing O_2 concentration, as expected. O_2 values were then calculated using Eq. 2.1 and plotted over time in Fig. 3.6A (T = 30°C) and Fig. 3.7A (T = 25°C).

The O_2 concentration curve shows a response behavior to the concentration switches O_2 performed. Due to the diffusion-limited O_2 transport, the concentration follows an asymptotic progression until equilibrium and the final value is reached. The final O_2 values in the chip were determined in each equilibrium phase by averaging the measured concentration over the last 1h of each performed step and plotted over the desired values in Fig. 3.6B (T = 30°C) and Fig. 3.7B (T = 25°C). The graph clearly shows that the final O_2 concentration reached comparable values over the range from 0% to 100% O_2.

Finally, the gas switching performance was evaluated in terms of diffusion time. Here, the diffusion completion time, defined as the time required to reach 85%, 90% and 95% of the final O_2 saturation levels ($t_{85\%}$, $t_{90\%}$, $t_{95\%}$), were determined and plotted in Fig. 3.6C (T = 30°C) and Fig. 3.7C (T = 25°C). $t_{90\%}$ is indicated as central marker, whereas $t_{85\%}$ and $t_{95\%}$ are represented as the lower and upper bars. The plot shows that $t_{90\%}$ was in the range of 80 to 90 min, independent of the applied O_2 step width. These results are in line with the characteristic diffusion time, t_{diff}, which is independent of

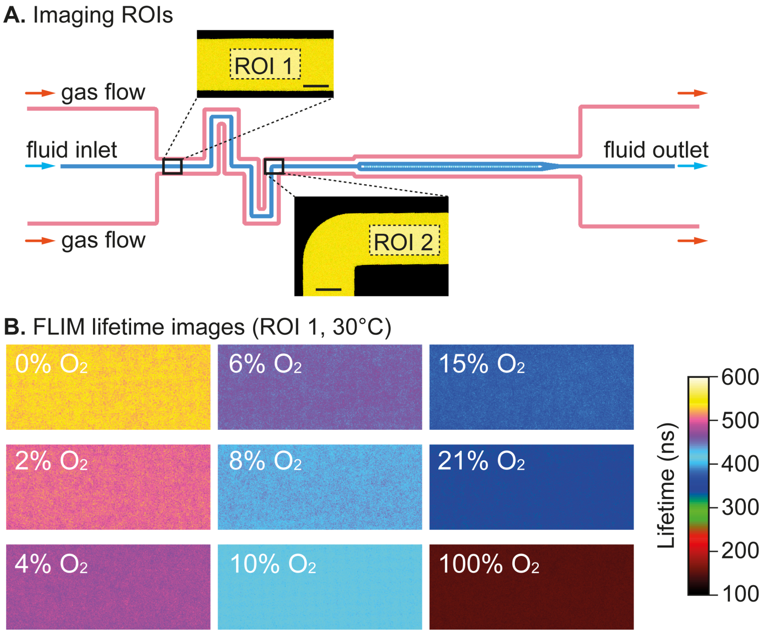

Figure 3.5: FLIM imaging under various O_2 conditions. **(A)** Imaging ROIs 1 and 2 where FLIM of the RTDP O_2 sensor in the fluid channel was performed (scale bars = 50 μm). **(B)** Representative FLIM images obtained at defined O_2 gas flow. The images were taken at ROI 1 at 30°C.

concentration, but depends on the diffusion length L and the material-specific diffusion coefficient D ($t_{\mathrm{diff}} = L^2/D$)[112].

The present system is limited regarding fast O_2 changes, which can be performed below two hours. This is mainly due to the millimeter-thick PDMS chip. The gas exchange can be accelerated by fabricating a thinner PDMS chip to reduce the time required for the gas exchange by diffusion [50, 83]. The objective of this chapter, however, was to develop a relatively simple setup enabling reliable switching and constant culture conditions.

3.3.2 Aerobic and Anaerobic Growth of *E. coli* - Population Level Analysis

As a proof-of-principle application, the impact of changing O_2 availability on microbial growth was investigated at the single-cell level. *E. coli* expressing GFP in the presence

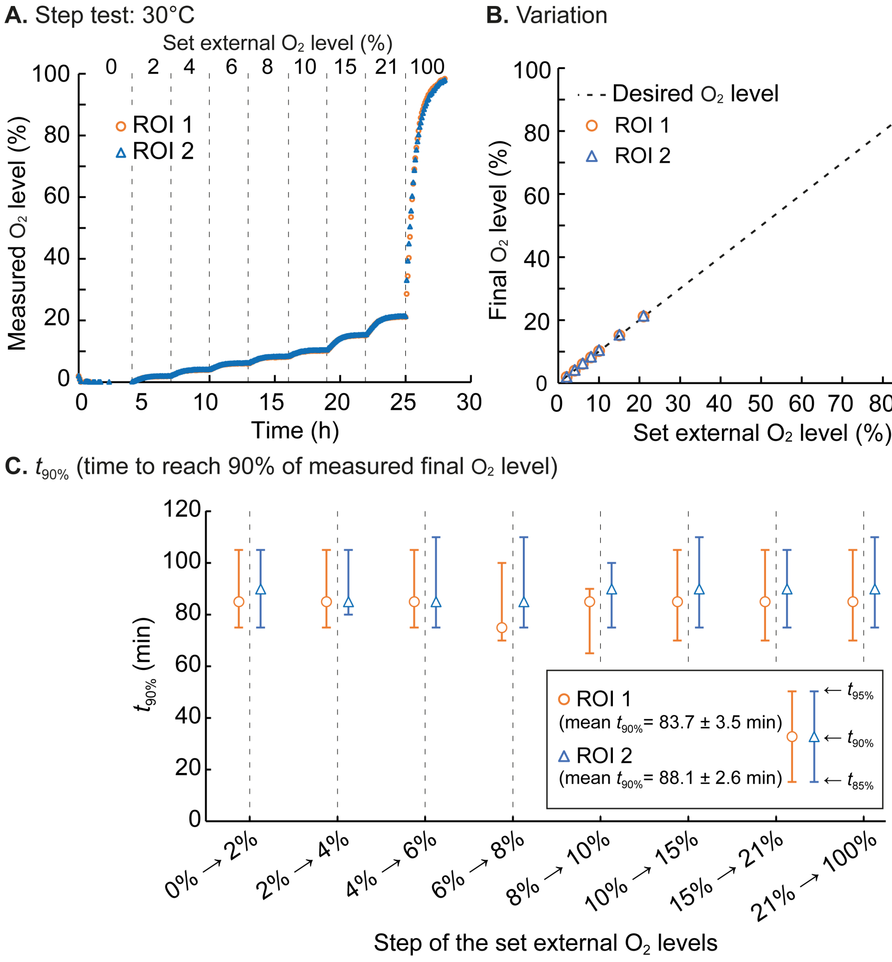

Figure 3.6: O_2 control performance characterization at 30°C. **(A)** O_2 concentration over time derived from corresponding fluorescence lifetime images at ROI 1 and 2. **(B)** Final O_2 concentration determined by FLIM over the externally applied gas flow. The dotted line shows the optimum. **(C)** Switching time analysis: $t_{90\%}$ for each step of the set external O_2 levels. The middle markers indicate $t_{90\%}$, and the bars indicate $t_{85\%}$ and $t_{95\%}$.

of the inducer IPTG was chosen as the model system, and cultures were performed under aerobic and anaerobic conditions. The final maturation step of the GFP chromophore requires O_2 present in the cell. Consequently, GFP fluorescence can only be detected when protein folding is completed at sufficient intracellular O_2, and the fluorescent pro-

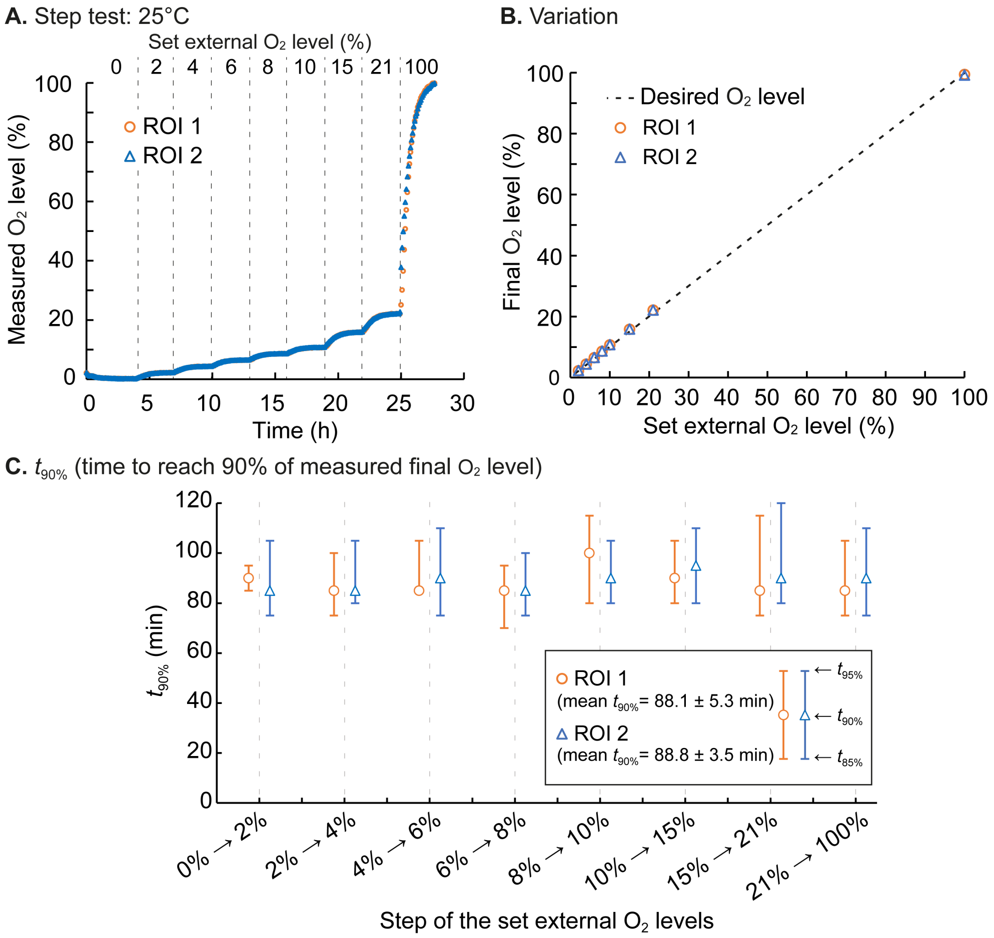

Figure 3.7: O_2 control performance characterization at 25°C. **(A)** O_2 concentration over time derived from corresponding fluorescence lifetime images at ROI 1 and 2. **(B)** Final O_2 concentration determined by FLIM over the externally applied gas flow. The dotted line shows the optimum. **(C)** Switching time analysis: $t_{90\%}$ for each step of the set external O_2 levels. The middle markers indicate $t_{90\%}$, and the bars indicate $t_{85\%}$ and $t_{95\%}$.

tein is fully functional. In the absence of O_2, however, chromophore maturation can not be completed despite complete protein expression, and no intracellular fluorescence should occur. However, once maturation has been completed under aerobic conditions, the GFP fluorescence no longer depends on the absence or availability of O_2. Then, the fluorescence intensity is mainly reduced by GFP dilution due to cell division, protein degradation, and chromophore bleaching. Thus, the present study used GFP as a rudimentary one-way indicator for intracellular O_2 (in this specific case, an O_2 increase was performed).

The phase contrast and the fluorescence microscopy images of growing colonies were acquired every 5 min. These time-lapse images were used to determine the dynamics and heterogeneity of intracellular GFP fluorescence in *E. coli* to study O_2 availability inside the cultivation chambers.

Under aerobic conditions, when infusing 21% O_2, and the continuous supply of fresh minimal medium, exponential *E. coli* colony growth was observed. An exemplary colony is shown in Fig. 3.8A, where phase contrast and fluorescence intensity images were merged for better visualization. In the presence of O_2, GFP was expressed in all cells over the entire culture period of 9 hours. Under anaerobic conditions, when infusing 100% N_2, surprisingly comparable exponential growth was still observed, but as expected, no intracellular GFP fluorescence was detectable for the first 8 hours, as shown in Fig. 3.8B. After 8 hours of culture time, the O_2 availability in the gas supply was switched to 21%, thereby creating aerobic conditions.

The cell numbers ($N_{\text{population}}$) were counted over the time-lapse images to determine population growth rates. The mean intensity of GFP fluorescence over the population ($I_{\text{population}}$) was derived from comparing fluorescence intensities. Here, populations in five independent growth chambers were analyzed for both conditions. The plot in Fig. 3.9A shows that the populations grew exponentially at the growth rate $\mu_{\text{aerobic}} = 0.55 \pm 0.06\ \text{h}^{-1}$ and the fluorescence $I_{\text{population}}$ increased nearly linear due to the continuous expression of fully matured GFP. The slope of the approximate line, $\Delta I_{\text{population}}/\Delta t$, was calculated as 23 a.u. h^{-1} between 00:00 h $\leq t \leq$ 09:00 h.

Under anaerobic conditions, the population growth rate was $\mu_{\text{anaerobic}} = 0.52 \pm 0.07\ \text{h}^{-1}$ (00:00 h $\leq t \leq$ 08:05 h), and the fluorescence $I_{\text{population}}$ stayed low and negligible fluorescence was detected, as shown in Fig. 3.9B. Then, immediately after the switch from anaerobic conditions to aerobic conditions, $I_{\text{population}}$ increased 7-fold faster and reached comparable values compared to non-switch conditions ($\Delta I_{\text{population}}/\Delta t = 165$ a.u. h^{-1} between 08:10 h $\leq t \leq$ 09:00 h).

This 7-fold rapid increase in fluorescence of $I_{\text{population}}$ after the switch to aerobic conditions can be explained as follows. During the primary anaerobic cultivation phase, GFP expression was performed, but intracellular O_2 was not available (or too low) to complete the chromophore maturation process. Incompletely produced GFP did not emit fluores-

A. Time-lapse images - *E. coli* MG1655 - aerobic

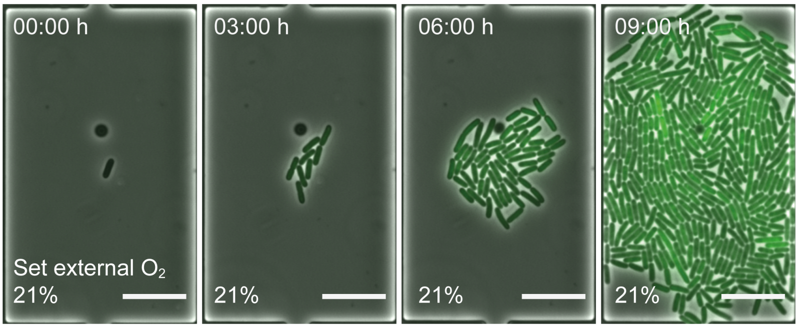

B. Time-lapse images - *E. coli* MG1655 - anaerobic with switch to aerobic

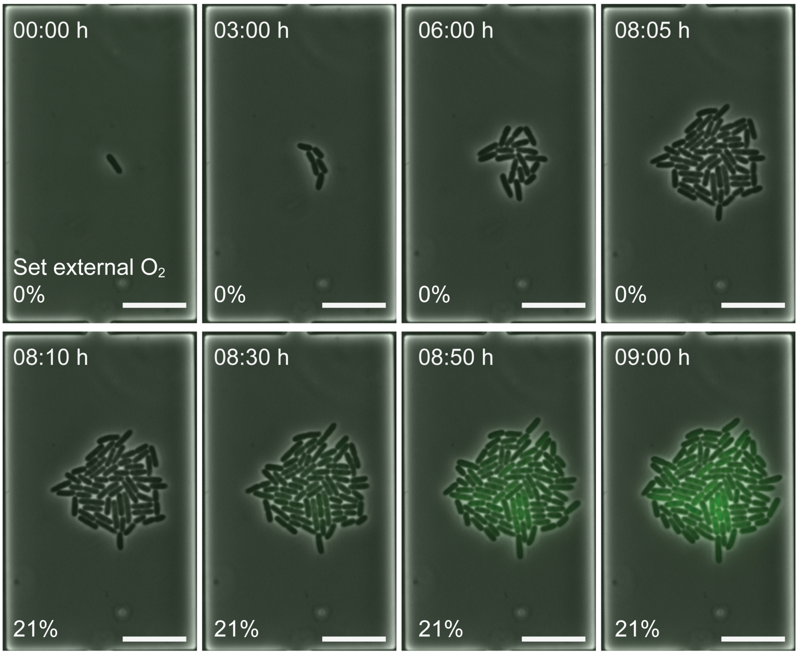

Figure 3.8: Time-lapse image series of *E. coli* MG1655 expressing GFP cultivated at 30°C, continuously supplied with M9 medium supplemented with 2% glucose. **(A)** Time-lapse image series from cultivation under aerobic conditions (00:00 h $\leq t \leq$ 09:00 h). **(B)** Time-lapse image series from cultivation under anaerobic conditions (00:00 h $\leq t \leq$ 08:05 h) with a switch to aerobic conditions (08:10 h $\leq t \leq$ 09:00 h). All scale bars = 10 μm.

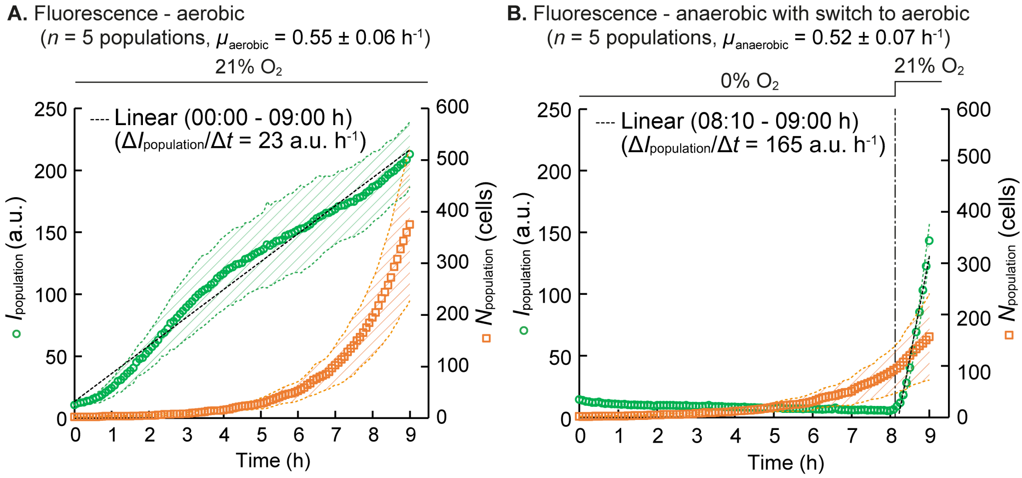

Figure 3.9: Population based analysis of *E. coli* growth and GFP expression. **(A)** Mean intensity of GFP fluorescence over population ($I_{\text{population}}$) and cell number ($N_{\text{population}}$) of *E. coli* MG1655 populations cultured under aerobic conditions. 1875 cells were analyzed at t = 09:00 h. The data are presented as mean ± S.D. denoted by the shaded areas (n = 5 individual populations). **(B)** $I_{\text{population}}$ and $N_{\text{population}}$ of *E. coli* MG1655 populations cultured under anaerobic conditions with a switch to aerobic conditions. 783 cells were analyzed at t = 09:00 h. The data are presented as mean ± S.D. denoted by the shaded areas (n = 5 individual populations).

cence. After switching to 21% O_2, intracellular O_2 became available, and the pending chromophore maturation could finally be completed. In addition, newly expressed GFP might have contributed to the increase in fluorescence. The minimum concentration of O_2 required for the GFP chromophore maturation was reported to be 0.1 ppm [113]. Therefore, it is speculated that the proposed system can be operated at concentrations as low as 0.1 ppm O_2; however, the fluorescence detection limit should be further considered in that context.

Since *E. coli* is a facultative anaerobic organism, it can continue to grow without O_2 using fermentation or anaerobic respiration. Interestingly, comparable growth rates were measured under both aerobic and anaerobic conditions, albeit it was previously reported that *E. coli* grows slower in the absence of O_2 [114]. It is assumed that the overall growth conditions within the microfluidic growth chambers are superior to conventional cultivation methods that typically involve batch cultivation. Previously, it was reported that continuous perfusion of media inside microfluidic devices allows for constant amounts of substrate, no accumulation of inhibitory by-products, and therefore, cells can exhibit faster growth rates throughout the culture period [115].

3.3.3 Aerobic and Anaerobic Growth of *E. coli* - Single-Cell Level Analysis

Time-lapse imaging includes spatiotemporally resolved data of single cells. As shown in the previous paragraph, population-level analysis delivered growth rates based on the number of segmented cells. However, tracking single microbes over subsequent time-lapse images is more challenging, especially if the temporal resolution is too low to follow distinct family lineages. This becomes even more difficult if all cells within the population have identical optical appearance. Therefore, the activity-prioritized cell tracking method was applied to explore single-cell fluorescence over the cell generations [111].

This method allowed deriving the mean intensity of GFP fluorescence (I_{cell}) from segmented cells as well as their corresponding generation number (number of cell divisions observed). Fast-growing cells resulted in high generation numbers, and slow-growing cells resulted in lower generation numbers. For the analysis, one exemplary micro population was selected from the aerobic and the anaerobic cultures, respectively. Three consecutive time points (t = 08:00 h, 08:30 h, and 09:00 h) were then chosen to visualize data analysis results.

Under aerobic conditions, a growth rate of $\mu_{\text{aerobic}} = 0.59\ \text{h}^{-1}$ was derived for the selected population. As shown in the fluorescence time-lapse images of Fig. 3.10A, a pronounced and relatively homogeneous intracellular GFP fluorescence was detected at all time points. In addition to single cell fluorescence levels, image analysis provided each corresponding cell generation, with the results visualized in (Fig. 3.10B), where the color coding from blue to yellow indicates the generation. By plotting single-cell fluorescence I_{cell} over the generation (Fig. 3.10C), correlations could be visualized. Here, there is a slight tendency for cells with lower generation numbers (i.e., slow-growing cells) to exhibit higher GFP fluorescence. In comparison, cells with higher generation numbers (i.e., fast-growing cells) exhibited lower GFP fluorescence.

Under anaerobic conditions ($\mu_{\text{anaerobic}} = 0.50\ \text{h}^{-1}$) this effect was more prominent. As shown in the fluorescence images in Fig. 3.11A, the GFP fluorescence was negligible before the switch at t = 08:00 h. After the switch from anaerobic to aerobic conditions, the GFP fluorescence of the cells rapidly increased, as discussed before (t = 08:30 h, 09:00 h), but phenotypic population heterogeneity in terms of fluorescence intensity was more pronounced. The cells corresponding generation numbers are visualized in Fig. 3.11B, also

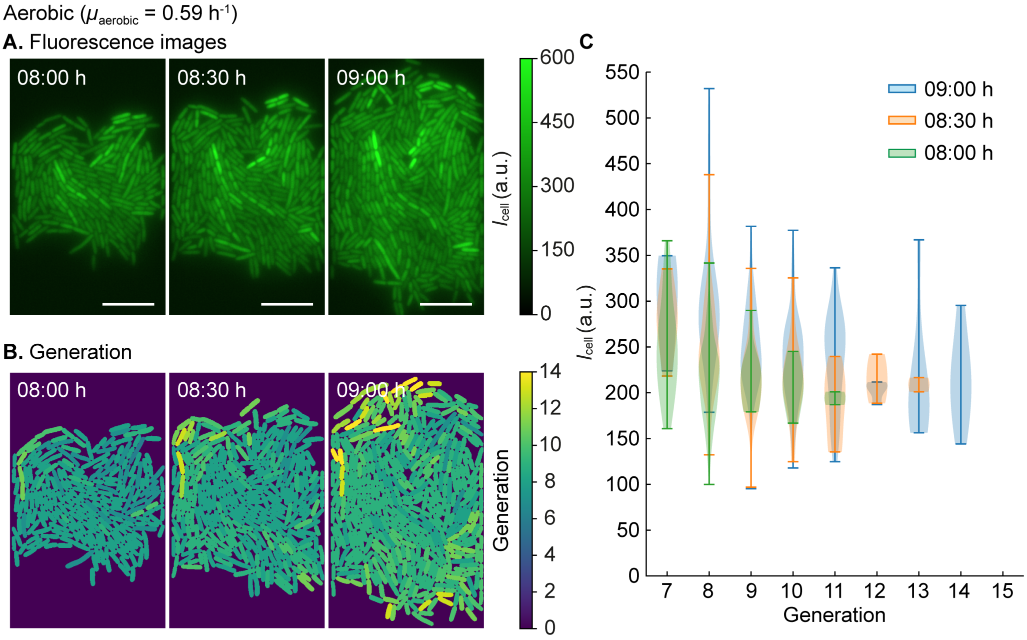

Figure 3.10: Single-cell tracking of fluorescence intensities (I_{cell}) and generation numbers, analyzed for a selected population from aerobic conditions. **(A)** Fluorescence intensity images at $t = $ 08:00 h, 08:30 h, and 09:00 h (scale bars = 10 μm). **(B)** Generations number (number of division events detected) visualized by color coding. **(C)** I_{cell} and generations at three time points.

indicating a more pronounced heterogeneity in terms of single-cell growth rates. Moreover, the plot showing I_{cell} over generation number (Fig. 3.11C) shows that intracellular GFP fluorescence decreases with the increasing division rate. This correlation is likely due to a higher dilution rate of intracellularly accumulated GFP during faster cell division.

3.4 Discussion

Here, a microfluidic cultivation system for microbial single-cell analysis was described. In addition to environmental control by continuous media perfusion, it enables microbial cultures under O_2 control. To this end, a microfluidic cultivation chip was placed inside a simple and low-cost 3D-printed mini-incubator. A couple of mass flow controllers were

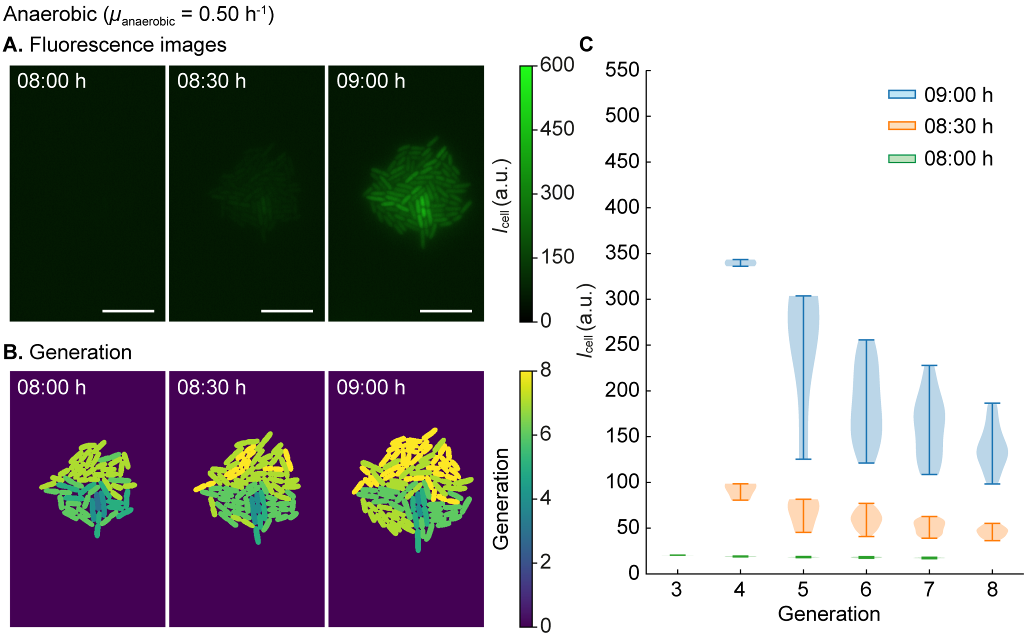

Figure 3.11: Single-cell tracking of fluorescence intensities (I_{cell}) and generation numbers, analyzed for a selected population from anaerobic conditions with a switch to aerobic conditions. **(A)** Fluorescence intensity images at t = 08:00 h, 08:30 h, and 09:00 h (scale bars = 10 μm). **(B)** Generations number (i.e., number of division events detected) visualized by color coding. **(C)** I_{cell} and generations at three time points.

used to deliver defined O_2 / N_2 gas mixtures, which in the present configuration allow for control of O_2 supply from 0% to 100% O_2. The design allows a switching time of less than 100 minutes, which is currently only limited by the thickness of the gas-permeable chip material PDMS. This thickness can be further reduced, requiring more specialized chip assembly and handling.

Camera-based fluorescence lifetime imaging was used to monitor the O_2-sensitive dye RTDP, which can be easily delivered as a sensor solution when pumped through the channels. Measuring the fluorescence lifetime of RTDP is more robust than measuring fluorescence intensity because the lifetime is independent of dye concentration. The RTDP sensor solution has a wide detection range and can be used as an O_2 sensor from 0% to 100% O_2. The detection limit of RTDP as an O_2 sensor is reported to be around 0.5 μmol/L O_2 (0% O_2) [116]. However, the present system is limited by the resolution and detection limit of the camera-based FLIM microscope setup, which should be investigated in more detail. Presumably, anaerobic cultures were performed when 100% N_2 was supplied. It is assumed that the chip can be operated with at least 0.1 ppm O_2, indirectly demonstrated by the incomplete chromophore maturation in the absence of O_2 when using GFP as an intracellular O_2 sensor.

The analyses of microorganisms at both the population and single-cell levels were performed. The strength of the proposed approach is that knowledge from different levels can be obtained from the same experiment. In addition to microfluidic monolayer cultivation, there are several widely used methods for microbial single-cell analysis, such as fluorescence-activated cell sorting and droplet confinement of single cells in a low volume of aqueous solution [117–119]. Although these well-established technologies provide data on vast numbers of cells, they are not suited for spatiotemporal microbial analysis and, therefore, cannot deliver knowledge at the spatially resolved population level. However, considering that the microbial heterogeneity of single cells can influence microbial behavior at the population level, observing microbial behavior at different levels - population and single-cell - and linking them would help add more insight to microbiological research. The power of such an analysis becomes more apparent when a microbial culture is performed in a structured O_2 environment.

Automated image analysis was used to extract cellular properties from large stacks of image data. All these tools are made available as open source. The cultivation setup can serve as an experiment-to-analysis system for various microbial single-cell analysis applications, such as the cultivation of micro-aerophilic and strictly anaerobic organisms whose single-cell behavior has not yet been thoroughly investigated. As iron solubility is dependent on O_2 concentration, studies of iron availability and its effect on cellular physiology are possible. A more advanced microfluidic configuration would also allow O_2 gradients and other patterns to be created. The setup is not limited to controlling O_2 and nitrogen gas but can be adapted to different gases.

4 Double-Layer Microfluidics for Recreating Rapid Oxygen Oscillations

Microbial metabolism and growth are tightly linked to the presence of O_2. Despite microbes often encountering fluctuating O_2 conditions in their natural habitats, our understanding of cellular response and adaptation to O_2 fluctuations at various time scales is limited. This is due to difficulties monitoring microbial growth at the single-cell level under precisely controlled O_2 supply and correlating single-cell growth with the O_2 microenvironment. Here, time-resolved microbial growth analyses were performed at single-cell resolution under a well-controlled O_2 supply. Therefore, a multilayer microfluidic device incorporating a gas supply layer on top of a cultivation layer with a thin intermediate membrane was developed, enabling efficient and homogeneous gas transfer, and thus microbial cultivation under constant, dynamic, and periodically oscillating O_2 environments. Implementing automated time-lapse microscopy and deep-learning-based image analysis, this platform provides access to spatio-temporally resolved microbial growth data at the single-cell level. O_2 switching within tens of seconds and precise knowledge of the resulting microenvironment facilitates accurate correlation between cellular growth and the local O_2 concentration. Performing *Escherichia coli* cultivations under various O_2 oscillation periods revealed distinct growth dynamics, characterized by response, recovery, and adaptation phases, synchronized with applied O_2 oscillation periods. Comprehensive growth data and analyses from the unique platform are crucial for systematically studying the cell response and adaptation to oscillating O_2 environments at single-cell resolution. Part of the results in this chapter were published in Kasahara *et al.*, *Lab on a Chip*, 2025.

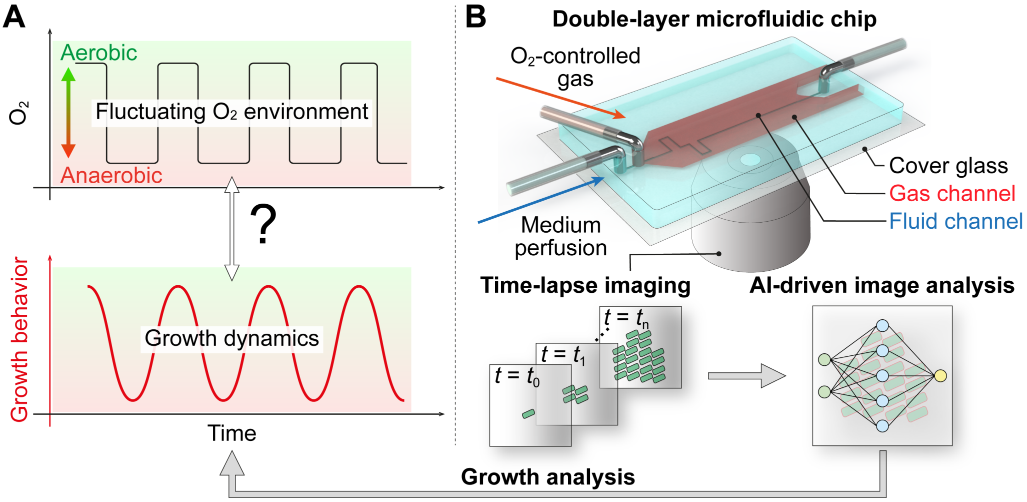

Figure 4.1: Conceptual illustration of the on-chip microbial growth analysis under rapidly fluctuating O_2 environment. **(A)** The conceptual sketch of the proposed analysis of microbial growth behavior with a one-to-one correspondence to the external fluctuating O_2 environment. **(B)** The analytical platform comprises the double-layer microfluidic chip, time-lapse microscopy, and deep-learning-based image analysis, enabling microbial growth characterization under oscillating O_2 environments at high spatiotemporal resolution.

4.1 Technical Concept

4.1.1 Double-Layer Microfluidic Chip to Enable Rapid Gas Control

In the previous chapter, gas control was managed using the mini-incubator mounted on the microscope stage. While this setup was easy to install, it required over an hour for adequate gas exchange due to gas diffusion through the thick PDMS chip, limiting its suitability for experiments requiring rapid gas fluctuations. A device capable of faster gas exchange is anticipated for recreating rapidly fluctuating O_2 environments and investigating microbial growth dynamics under such conditions (Fig. 4.1A).

To address this, a double-layer microfluidic chip was developed to enable faster gas exchange in tens of seconds and recreate rapid O_2 oscillations on-chip (Fig. 4.1B). The chip comprises two layers: a top layer for gas supply and a bottom layer for fluid supply and cell cultivation. These layers are separated by a thin intermediate membrane (65 µm)

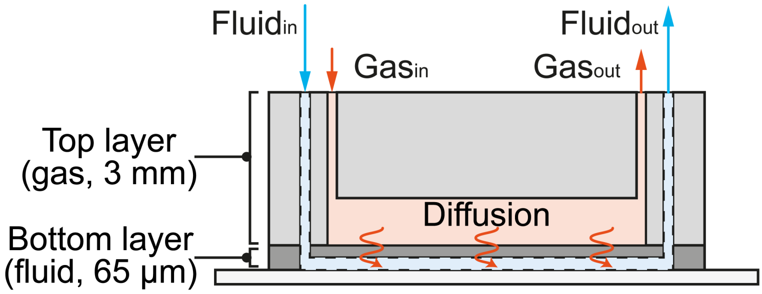

Figure 4.2: Conceptual illustration of the fast gas exchange through the intermediate thin membrane separating the top and bottom layers.

that enables rapid gas diffusion from the top to the bottom layer, facilitating rapid gas control within the medium (Fig. 4.2). Images obtained from time-lapse imaging during microbial cultivation in the microfluidic chip are analyzed using a deep learning-based image analysis platform. This method allows for the efficient extraction of growth data from a large dataset and provides time-resolved microbial growth analysis that is explicitly correlated with well-defined O_2 fluctuations (Fig. 4.1B).

4.1.2 Modular System Allowing Various Chip Designs

Another key feature of the double-layer chip is its modular design, which accommodates various interchangeable configurations for both the top and bottom layers, as long as the overall chip dimensions remain constant. As shown in Fig. 4.3, the top layer for gas supply can be tailored in multiple ways—such as uniform, gradient, separate, or lattice patterns—similarly to the bottom layer for fluid, which may incorporate designs for chambers, co-culture setups, mother-machine channels, or batch modes. This modular approach provides a flexible platform for recreating diverse spatiotemporal O_2 microenvironments with reduced effort in developing a new chip design, enabling the double-layer chip to be applied to a wide range of research requiring spatiotemporal O_2 control.

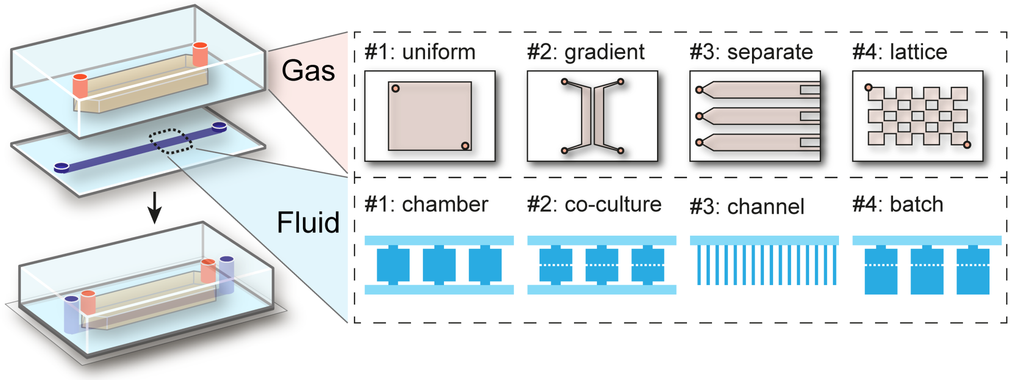

Figure 4.3: Conceptual illustration of the modular system allowing various chip designs.

4.2 Materials and Methods

4.2.1 Microfluidic Device Fabrication

The double-layer microfluidic device, comprising an upper and a lower layer, was fabricated by molding PDMS in separate molds and by assembling (Fig. 4.4) [50]. Firstly, the mold for the upper layer was modeled using CAD and 3D printed with stereolithography as shown in Fig. 4.5 (Form 3B, Formlabs, US). The mold was filled with a mixture of precured PDMS solution (10:1) and heated to 80°C for 20 minutes to initiate the first curing step. A silicon wafer with a two-layer SU-8 photoresist was fabricated by photolithography as described in a previous paper [120] at Helmholtz Nano Facility, Germany [109] and employed as the mold for the lower layer. The PDMS was spin-coated onto the SU-8 mold at 1000 rpm for 60 seconds (SPIN150i, APT Automation, Germany) and heated at 80°C for 10 minutes to initiate the first curing step. Then, the upper layer was peeled off from the mold, cut into chips, and inlets were punched (punching tool ϕ = 0.75 mm, World Precision Instruments, US). The lower layer was not peeled off at this step. The upper layer was then placed onto the lower layer and heated at 80°C for at least one hour. This constituted the second curing step, whereby the upper and lower layers were irreversibly bonded through the full curing process. Once fully cured, the chip was peeled off from the wafer, holes were punched (ϕ = 0.50 mm, World Precision Instruments, US), and bonded to a glass substrate (D263®Bio, 39.5 mm × 34.5 mm × 0.175 mm; Schott AG, Germany) by O_2 plasma treatment for 25 seconds (Femto Plasma Cleaner, Diener

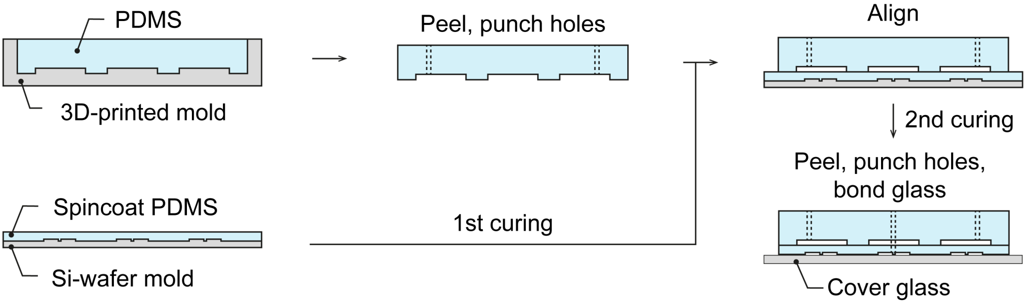

Figure 4.4: Fabrication procedure of the double-layer PDMS microfluidic chip.

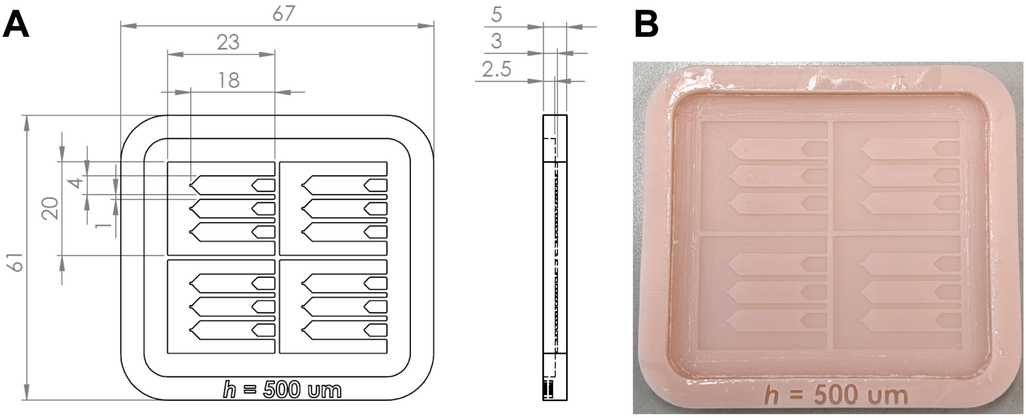

Figure 4.5: 3D-printed mold for the upper layer with three separate gas channels. **(A)** Dimensions of the designed mold in mm. **(B)** Image of the printed mold.

Electronics, Germany). The bonded chip was heated at 80°C for one minute to increase the stability of the bonding.

The thickness of the PDMS membrane (fluid layer) was measured using a stylus profiler with a 12.5 µm radius stylus (Dektak 150, Veeco Metrology, US). The resulting PDMS membrane thickness (W) dependent on spin-coating speed (ω) can be expressed with fitting parameters (A, b) as follows [121].

$$W = A\omega^{-b} \tag{4.1}$$

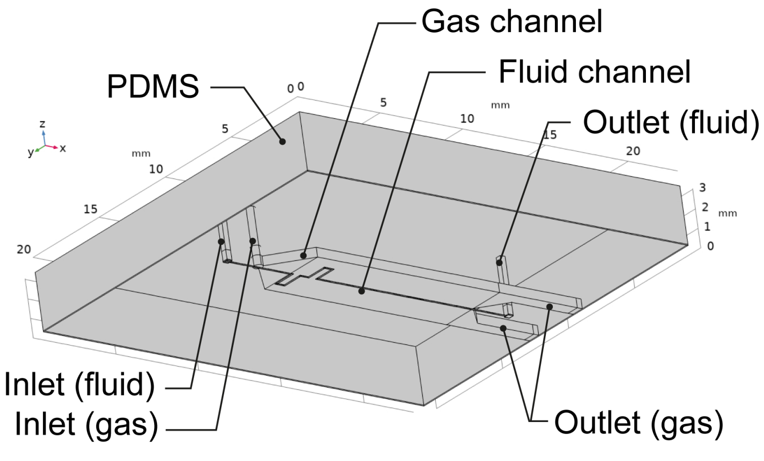

Figure 4.6: Geometry of the PDMS chip generated for gas diffusion simulation.

4.2.2 Computational Simulations

The gas distribution in the PDMS chip was simulated using a finite element method (COMSOL Multiphysics 6.0, COMSOL). A three-dimensional geometrical model comprised three distinct subdomains: a PDMS block, a fluid channel, and a gas channel (Fig. 4.6). A hexahedral mesh was generated for the fluid channel, while a tetrahedral mesh was generated for the remaining geometry. The physical phenomena of fluid and gas flow were numerically analyzed by solving the time-dependent Navier-Stokes equations for laminar and incompressible flow. O_2 transport was determined by diffusion and convection and by the ratios between O_2 concentration and O_2 solubility at the different material boundaries. Further details regarding the simulation setup are described in the Appendix A.

4.2.3 Microscopy

An inverted microscope (Nikon Eclipse Ti-E 2, Nikon, Japan), equipped with a CMOS camera (DS-Qi2, Nikon, Japan) for phase-contrast image acquisition and a FLIM camera (550 kHz frequency domain; pco.flim, PCO AG, Germany), was utilized for the experiments. The FLIM camera was connected to a modulated excitation laser (445 nm, 100 mW; pco.flim laser, Omicron-Laserafe Laserprodukte GmbH, Germany). The microscopy setup was customized with a perfect focus system (PFS, Nikon, Japan) and a temperature incubator (Okolab, Italy) to facilitate automated live-cell imaging during cell cultivation on the microscope. Phase-contrast observation for biological cultivation was conducted with a 100× objective (Plan Apo λ Oil, Nikon, Japan). FLIM imaging was conducted with a 20× objective (Plan Apo λ, Nikon, Japan). To perform FLIM, a customized filter cube was used, which was composed of an excitation filter (440/40, F47-440), a long-pass (LP) dichroic mirror (495LP, F48-495), and an emission filter (605/70, F47-605). All the filter components were purchased from AHF analysentechnik AG, Germany. A custom-made chip holder was used to mount the chip on the microscope stage. The FLIM was calibrated using a reference fluorescent slide with a known lifetime (lifetime = 3.75 ns, UMM-SFG, Starna Scientific, UK) as a standard. Further details are described in a previously published paper [103].

4.2.4 Gas Control and O_2 Sensing

Three interconnected mass flow controllers were utilized to continuously deliver the synthetic air mixture with the desired concentrations of N_2, O_2, and CO_2 (red-y, Vögtlin Instruments GmbH, Switzerland). For on-chip gas control, the inlet of the gas channel was connected to the mass flow controllers. The desired O_2 concentrations in the gas supply were achieved by automatically adjusting the corresponding volume flow rates for O_2 and N_2 while maintaining the total flow rate constant at 600 mL/min throughout the oscillations. 0.4 mL/min of CO_2 was always added to the synthetic air to facilitate reproducible growth of *E. coli* [122]. A tubing with a low gas permeability (N_2: 1.2 barrer, O_2: 2.2 barrer; Tygon®F-4040-A, Saint-Gobain, France) was used to connect the mass flow controller and the hole on the upper layer of the chip. To measure O_2 concentrations of in-flow coming out of the tubing, a fiber O_2 microsensor was used and inserted directly in the tubing (OXR50, pyroscience, Germany).

The O_2 level in the chip was measured by fluorescence lifetime imaging (FLIM) and an O_2-sensitive dye RTDP. The fluorescence of RTDP is quenched in the presence of O_2, which can be quantified as a change in fluorescence lifetime (τ), described by the Stern-Volmer equation (Eq. 2.1).

Here, τ at 21% O_2 (τ_{21}) was used to derive K_q. The gaseous conditions of 0% and 21% O_2 were set by adjusting the mass flow rate of N_2 and O_2. The parameters were determined from the measurement as follows; τ_0 = 481 ns, τ_{21} = 307 ns, K_q = 2.71.

4.2.5 Cell Preparation

E. coli MG1655 was stored in a ROTI Store cryo vial (ROTI®Store cryo vial, Carl Roth, Germany). All microbial cultivations were conducted using a lysogeny broth (LB) complex medium comprising 10 g/L peptone, 5 g/L yeast extract, and 10 g/L NaCl. The pH of the LB medium was adjusted to 7.0 with NaOH, autoclaved at 121°C for 20 minutes, and stored at 4°C. All the aforementioned chemicals were purchased from Carl Roth, Germany. A single bead from the cryo vial was transferred to a 20 mL LB medium in a shaking flask and cultured at 37°C, 150 rpm, for around 16 hours. The subsequent culture was initiated by inoculation from the previous culture, with an initial optical density (OD_{600}) of 0.3 or 0.0001, and cultivated until it reached the exponential growth phase.

4.2.6 Microfluidic Cultivation and Time-Lapse Imaging

The inoculation in the microfluidic chip was performed with the cell solution containing exponentially growing cells, with $OD_{600} = 0.5$. The cell solution was introduced into the fluid channel of the chip with a syringe (Omnifix®-F 1 mL, Braun, Germany). Following the successful inoculation, the syringe was replaced with a new one containing a fresh medium. The remaining cells within the channel were flushed by manually pushing the syringe. The medium was perfused at a constant rate of 100 nL/min using a syringe pump (neMESYS, CETONI, Germany). The chip cultivation continued for three hours before the colony reached the chamber size. The time-lapse imaging was performed, with an image acquisition interval $\Delta t = 1$ min for all the cultivation under constant O_2 environments, and $\Delta t = 10$ seconds for all the cultivation under oscillating O_2 environments.

4.2.7 Image Analysis

The acquired FLIM image data in nd2 format was saved as OME.TIFF files and processed using Fiji to measure the lifetime in a rectangular ROI (l 500 pixels $\times$ w 100 pixels). A median filter (pixel size = 5) was employed to remove noise. Cell segmentation and analysis codes are openly available at `https://github.com/JuBiotech/Supplement-to-Kasahara-et-al.-2025`.

4.2.8 Growth Analysis

Colony area (A_{colony}), which is the sum of single-cell area ($A_{\text{single cell}}$) in a colony, was used for growth analysis because A_{colony} provides us with continuous values as opposed to cell number, which is beneficial for further calculations. A_{colony} was normalized by the colony area at the start of cultivation to compare different chambers and conditions. Exponential growth rates, μ, were quantified based on A_{colony} in the exponential growth phase, as follows.

$$\mu = \frac{\ln A_{\text{colony},\, t} - \ln A_{\text{colony},\, t_0}}{t - t_0} \tag{4.2}$$

The relation of growth rate and O_2 availability was modeled by a Monod kinetic [123] including an offset for anaerobic growth, C (h^{-1}) at 0% O_2, as follows.

$$\mu = \mu' \frac{S_{O_2}}{K_{O_2} + S_{O_2}} + C \tag{4.3}$$

$\mu' + C$ (h^{-1}) is the growth rate under high O_2 availability and K_{O_2} (%) is the so-called Michaelis-Menten constant. S_{O_2} (%) represents the dissolved O_2 saturation in solution, expressed as a percentage relative to the equilibrium value under pure O_2 (100%) at the same temperature and pressure.

Instantaneous growth rates, $\mu_{\Delta t}$, the first derivative of A_{colony}, were calculated as follows.

$$\mu_{\Delta t} = \frac{\ln A_{\text{colony},\, t+\Delta t} - \ln A_{\text{colony},\, t-\Delta t}}{2\Delta t} \tag{4.4}$$

Phase-averaged growth rates under aerobic and anaerobic gassing phases ($\bar{\mu}_{\text{aerobic}}$ and $\bar{\mu}_{\text{anaerobic}}$) were determined by averaging obtained values from all the periods in all the analyzed colonies. t_{response} was determined as the time to hit the lowest $\mu_{\Delta t}$. t_{recovery} was determined as the time for the linear regression slope of $\mu_{\Delta t}$ in a shrinking window to reach zero.

The fast Fourier transform (FFT) was performed using the Data Analysis Tools in Excel. The sample size was adjusted to 2^n before FFT. For all the growth analysis, growth data between $0\text{ h} \leq t < 1\text{ h}$ were omitted since growth data at the beginning of the cultivation was occasionally affected by high noise due to a low initial cell number. Datasets with Δt = 10 seconds were smoothed by a centered moving average (window size = 5) before calculating $\mu_{\Delta t}$ to reduce noise.

4.3 Results

4.3.1 Double-Layer Chip Fabrication

The fabricated double-layer chip is depicted in Fig. 4.7A. For visualization purposes, the top gas-layer channels (red) and bottom fluid-layer channels (blue) were filled with colored dyes. The SEM image (Fig. 4.7A (i)) depicts a series of cultivation chambers (50 μm$\times$30 μm$\times$1 μm), in which cells are trapped, and their growth can be observed over time via time-lapse imaging during cultivation. Each growth chamber is connected to two parallel medium supply channels (w = 100 µm, h = 10 µm), enabling continuous medium perfusion but mass transfer inside the chamber solely by diffusion. The cross-sectional photograph of the device (Fig. 4.7A (ii)) shows the PDMS membrane, which has a thickness of approximately 65 µm (fluid layer in the figure), physically separating the upper gas channel from the lower fluid channel. The thickness of the membrane can be tuned by changing the spin-coating speed, as shown in Fig. 4.7B. Using Equation 4.1, a fitting curve to the measurement results was acquired, with fitting parameters $A = 0.11$ and $b = 1.07$ ($W = 0.11\omega^{-1.07}$; W in m, ω in rpm).

As explained in Chapter 4.1, the design for the upper layer can be interchangeable with other designs with minimal effort thanks to its modular system. To show this capability, two designs (uniform and gradient) are fabricated using the same fabrication procedure, as shown in Fig. 4.8. The top gas-layer channels (orange) and bottom fluid-layer channels (blue) were filled with colored dyes for visualization. In the uniform design, a rectangular gas channel (l 15 mm $\times$ w 13 mm) is placed on the fluid layer, allowing one gas condition at a time. The six pillars in the gas chamber support the structure. In the gradient design, two separate gas channels are prepared with a distance of 1 mm. By flushing gas with different O_2 concentrations in the two gas channels, the O_2 gradient is established within a 1 mm distance between the gas channels. Fabricating these chips requires only a 3D-printed mold for the top layer, allowing new designs with minimal effort (CAD design + $\sim$ 1 hour printing).

4.3.2 Gas Control Optimization

To optimize the mass flow controller configurations (flow rate, connecting order), the O_2 concentration was measured inside the supply tubing outlet under different gas-supply flow rates (10, 20, 50, 100, 200, 600 mL/min) when no chip was installed, as shown in

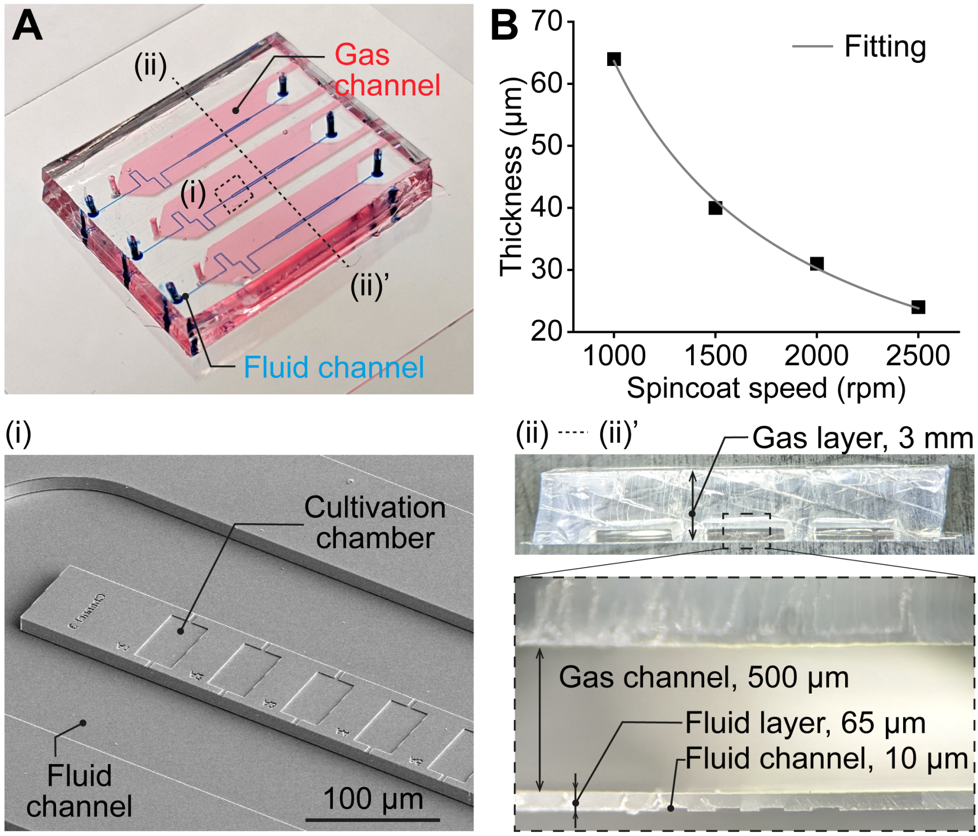

Figure 4.7: Fabricated double-layer microfluidic chip. **(A)** The image of the fabricated chip filled with color dyes (gas channel: red, fluid channel: blue). (i) The SEM image of the cultivation chambers and (ii) the cross-sectional image are also shown. **(B)** The measured thickness of the fluid layer fabricated with different spin-coating speeds. The solid line shows a theoretical fit.

Fig. 4.9A and B. The O_2 concentration was switched from 100% to 0% at $t = 0$ min. The measurement results in Fig. 4.9B indicate shorter gas exchange time with higher mass flow rates. The results also suggest that the gas-supply volume flow rate is the limiting factor in the design, primarily impacting the exchange time of O_2 in the fluid channel rather than diffusion across the PDMS membrane.

Furthermore, different orders of mass flow controllers were examined since dead volumes in the mass flow controller affected the resulting switching performance,

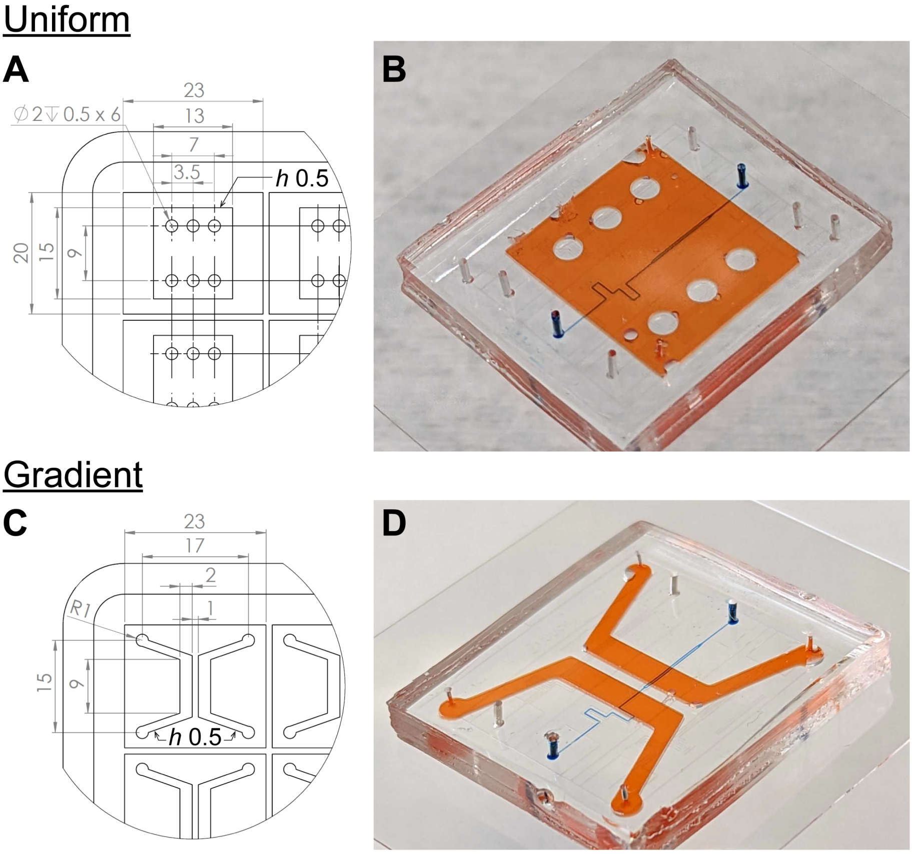

Figure 4.8: Fabricated microfluidic chip with various designs. **(A)** Part of the dimensions of the designed mold in mm (uniform). **(B)** The image of the fabricated chip (uniform). **(C)** Part of the dimensions of the designed mold in mm (gradient). **(D)** The image of the fabricated chip (gradient).

mostly when O_2 flow was entirely switched off, and residual O_2 remained inside the non-perfused tubing and connectors. The residual O_2 is depleted relatively slowly by diffusion and delays on-chip switching performance. When switching to higher O_2 levels, this problem is not observed since all interconnections are continuously perfused, and no controller is switched off. Two different orders (non-serial and serial) were examined here, as shown in the sketch in Fig. 4.9C. In the serial order, the N_2 flow controller is connected at the backmost, expecting all the residual O_2 to be flushed away and, therefore, faster gas exchange. The plot in Fig. 4.9C depicts the O_2 measurement

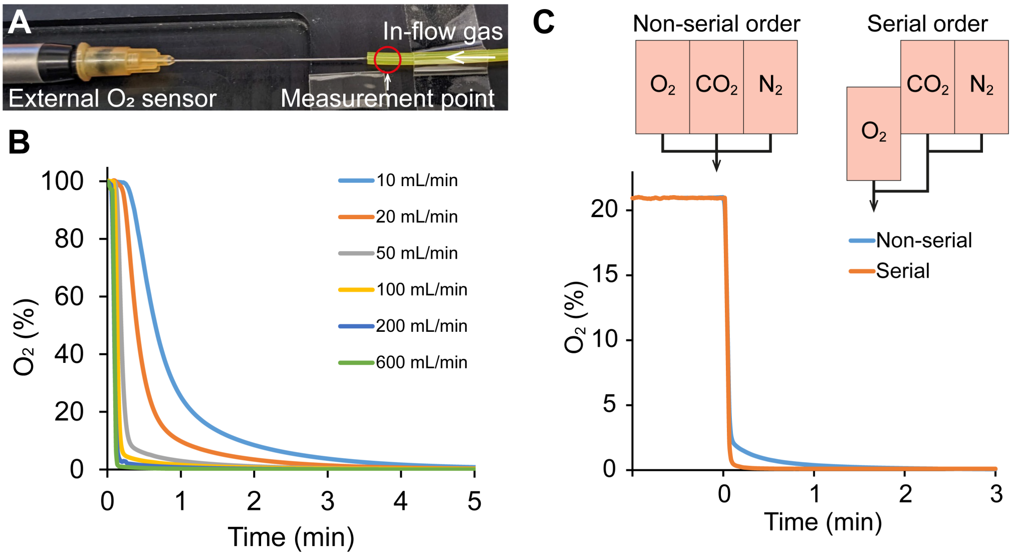

Figure 4.9: Mass flow controller optimization. **(A)** The setup to measure O_2 concentration of in-flow gas inside the supply tubing outlet. **(B)** Measured O_2 level in the in-flow at different mass flow rates. **(C)** Measured O_2 level in the in-flow with different orders of mass flow controllers (flow rate = 600 mL/min).

result (from 21% to 0%), indicating the faster gas exchange in the serially ordered mass flow controllers compared to non-serially ordered ones (6.9-fold faster to reach 0.21%).

With the serially ordered mass flow controllers, the on-chip gassing performance was simulated using computational fluid dynamics with experimentally determined gas-inflow concentration profiles. As depicted in Fig. 4.10A, the simulated O_2 level in the fluid channel exhibits a corresponding change from 21% to 0% when the O_2 level in the inlet gas is changed from 21% O_2 to 0% O_2 at $t = 0$ min. Based on the simulation results, the maximum total flow rate of N_2 and O_2 at 600 mL/min was applied to achieve rapid modulation of O_2 within the fluid channel.

4.3.3 On-Chip O_2 Control Characterization

With the determined total flow rate, the O_2 switching performance was experimentally validated by imaging the fluorescence lifetime of the O_2-sensitive dye RTDP inside the fluid channel with FLIM. Figure 4.10B depicts O_2 concentration measured in the fluid

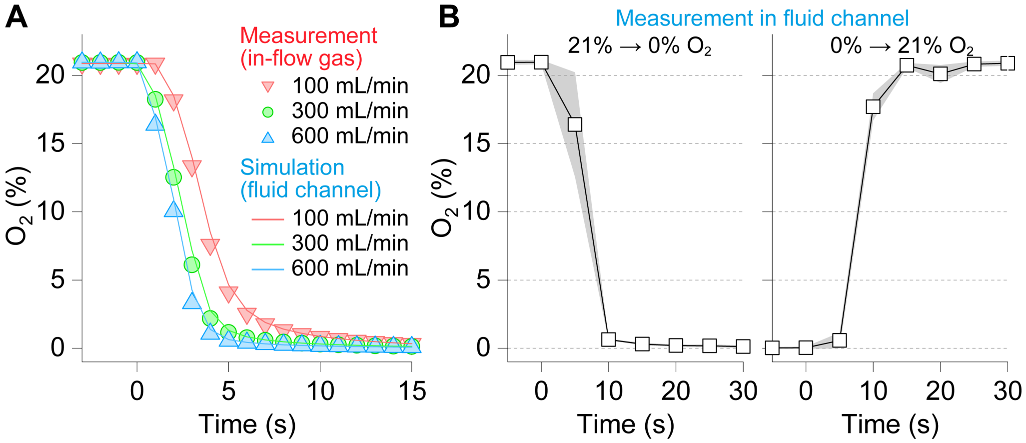

Figure 4.10: Characterization of the on-chip O_2 control. **(A)** Measured O_2 level in the in-flow (plots) and simulated O_2 level at the center of the fluid channel (solid lines) after a shift of O_2 supply from 21% to 0% at mass flow rates of 20, 100, and 600 mL/min. **(B)** Measured O_2 level in the fluid channel after a shift of O_2 supply between 21% and 0%. Data are expressed as mean ± S.D. (*n* = 3 measurements).

channel after the gas exchange from 21% to 0% and vice versa. The supply gas diffused rapidly into the fluid, achieving 99% of the aimed conditions (corresponding to a residual O_2 concentration of 0.21% when switching from 21% to 0%) within 15 seconds in both directions. The O_2 level in the gas supply was also switched between 21% and 0% at various oscillation half periods *T'* (*T'* = 60, 30, 10, 5, 2, 1, 0.5 min), showing the robust experimental O_2-level data when toggling between 21% and 0% at various *T'*, as demonstrated in Fig. 4.11. These device characterization results ensure a fast gas exchange in the order of seconds in the developed microfluidic device.

4.3.4 Optimizing on-Chip Cultivation Conditions

As an initial step, *E. coli* MG1655 was cultivated in the double-layer chip under gas-controlled conditions to evaluate whether unrestricted cell growth could be achieved. Initially, only N_2 and O_2 were supplied for gas control (resulting in 21% O_2 concentration), with CO_2 excluded. Under these conditions, cell growth was reduced by more than half compared to ambient conditions despite similar O_2 availability (Fig. 4.12, conditions no. 1 to 3). To identify the cause of this restricted growth, various parameters, including

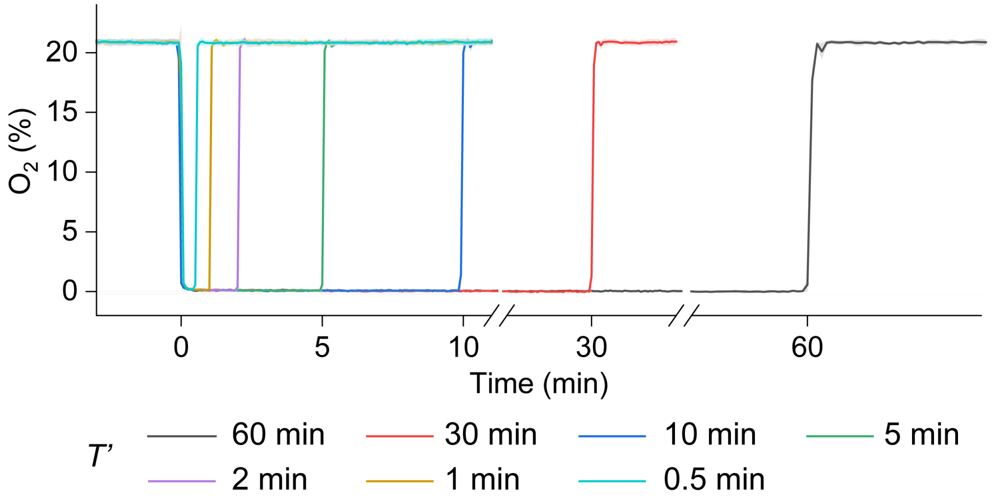

Figure 4.11: O_2 concentration in the fluid channel of the microfluidic chip determined by RTDP lifetime measurement with FLIM under oscillating O_2 environments at various oscillation half periods (*T'*).

temperature, mass flow rate, and CO_2 supplementation, were investigated. Fig. 4.12 summarizes the growth rates under different cultivation conditions (no. 1 to 7). Adjustments in mass flow rate (600, 100, and 20 mL/min; conditions no. 3 to 5) and temperature (40°C; condition 6) did not improve growth; however, adding CO_2 to the gas supply enabled a growth rate comparable to that observed under ambient conditions (condition no. 7). These findings clearly show that CO_2 is essential for achieving unrestricted growth of *E. coli*. Therefore, CO_2 was added to the air supply in the following *E. coli* cultivation experiments.

4.3.5 *E. coli* Growth in Constant and Homogeneous O_2 Environments

The fabricated double-layer cultivation device, as well as the optimized cultivation conditions, were first employed to cultivate *E. coli* MG1655 under a range of constant O_2 levels, between 0% and 21%. *E. coli* is a facultative anaerobic bacterium that can grow under aerobic, microaerobic, and anaerobic conditions. As known, the O_2-limited growth is slower than the growth under O_2-rich environments [34]. The cultivations under constant O_2 levels were conducted to determine whether the impact of various O_2 levels on microbial growth can be spatiotemporally resolved at the single-cell level.

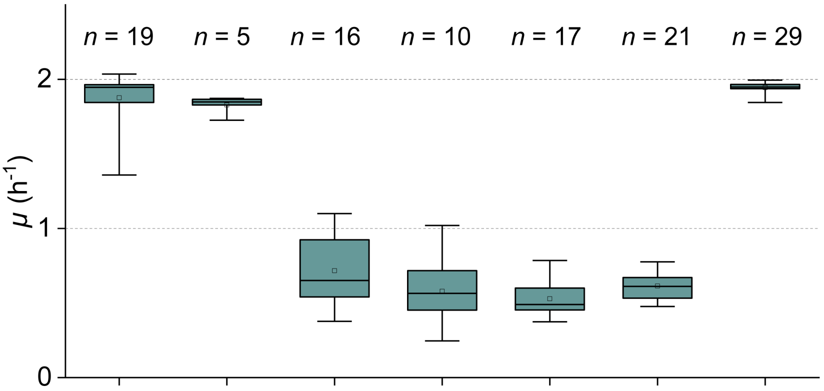

Condition no.	1	2	3	4	5	6	7
Temperature (°C)	37	40	37	37	37	40	37
Total mass flow rate N_2 & O_2 (mL/min)	0 (ambient)		600	100	20	600	600
CO_2 supplementation to gas supply	not applicable		w/o	w/o	w/o	w/o	w/

Figure 4.12: *E. coli* growth rate under different cultivation conditions. Boxes have the meaning of 25 and 75% quartile around the population median value (middle line), error bars indicate maximum and minimum, and squares indicate mean values. w/ and w/o indicate with and without, respectively.

Fig. 4.13A and B show representative time series of phase contrast images of *E. coli* cultivated under aerobic (21% O_2) and anaerobic (0% O_2) conditions. Both cultivations started with a single cell at 00:00 h, with a resulting larger colony area at 21% after 03:00 h cultivation time.

To further investigate whether various O_2 concentrations also result in a corresponding decrease in cell growth in the microfluidic growth chambers, *E. coli* was cultivated under constant O_2 concentrations, at 0%, 0.1%, 0.5%, 1%, 5%, 10%, and 21% O_2 in separate experiments. As shown in Fig. 4.14, the colony areas (A_{colony}), the sum of the individual cell areas, are quantified from the phase contrast time-lapse images. As the plot shows, A_{colony} exhibits exponential growth, with the lowest rate being observed at 0% O_2.

In Fig. 4.15, the exponential growth rates μ were quantified based on A_{colony} in the exponential growth phase, showing comparable growth at O_2 concentrations between

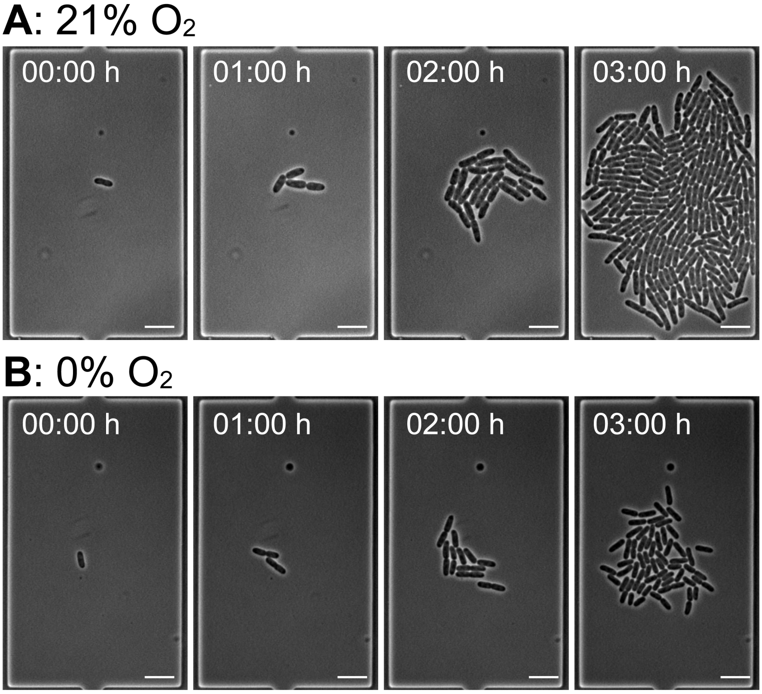

Figure 4.13: *E. coli* cultivation under steady O_2 supplies. **(A)** Phase-contrast images of *E. coli* cultivated under 21% O_2 supply (scale bars 5 µm). **(B)** Phase-contrast images of *E. coli* cultivated under 0% O_2 supply (scale bars 5 µm).

21% and 1%. The aerobic growth rate of around 2 fits the growth rate suggested in previous literature [124]. Conversely, μ strongly decreases when the O_2 level is below 0.5%. The relation of growth rate and O_2 concentration was modeled by an adapted Monod kinetic, which resulted in K_{O_2} of 0.07 ± 0.02%. As K_{O_2} describes the O_2 concentration in percentage at which the growth rate is reduced to half of the maximum growth under sufficient O_2, the low K_{O_2} indicates a substantial decrease in growth rate at very low O_2 levels. These results indicate that an O_2 level of at least 0.5% or below is necessary to observe a measurable shift between aerobic and anaerobic growth of *E. coli* within the device. Based on the gas exchange characterization described in Fig. 4.10B, a minimum switching time of approximately 15 seconds would be required to reduce the O_2 concentration below 0.5%.

the minimum switching time necessary to decrease O_2 concentration below 0.5% and observe a detectable change between aerobic and anaerobic growth was approximately

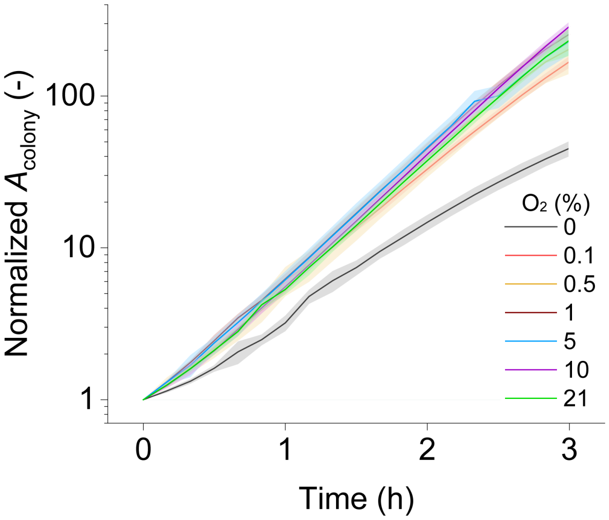

Figure 4.14: Growth curve based on colony area (A_{colony}) under various O_2 supplies. Data are expressed as mean ± S.D. n = 35 colonies (0%), 27 (0.1%), 21 (0.5%), 16 (1%), 13 (5%), 13 (10%), 29 (21%).

15 seconds. The slower growth observed at low O_2 concentration is in agreement with the Pasteur point (1% of the present atmospheric O_2 level), below which is thought to inhibit heterotrophic aerobic respiration [125].

Furthermore, beyond colony growth, the data can also be obtained at the level of single-cell area. Each gray plot in Fig. 4.16 represents a single-cell area ($A_{\text{single cell}}$) of each cell from images at t = 2 h, and red dots represent mean values. The mean values increase as oxygen concentration increases. This increase in cell size is reasonable, considering that cells with higher growth rates possess larger cell sizes [79, 126, 127]. More interestingly, there was a broad variation in single-cell area, ranging up to 14 μm^2. This wide distribution of single-cell areas suggests cell size heterogeneity within the population. Such heterogeneity in cell size might arise from a mixture of cells at different stages: smaller cells immediately post-division, larger cells just before division, and extensively sized cells with fewer division cycles. Such intra-population diversity can be effectively resolved using microfluidic cultivation combined with time-lapse imaging at the single-cell resolution.

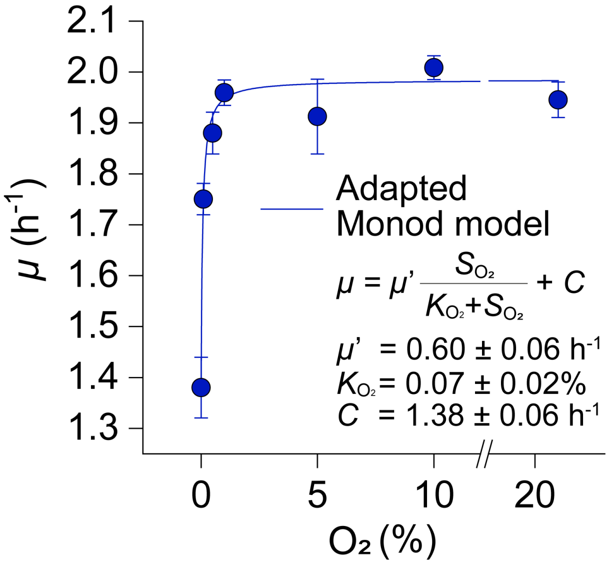

Figure 4.15: Exponential growth rate (μ) under various O_2 supplies. The fitted Monod kinetic model is shown with the blue line. Data are expressed as mean ± S.D. n = 35 colonies (0%), 27 (0.1%), 21 (0.5%), 16 (1%), 13 (5%), 13 (10%), 29 (21%).

4.3.6 *E. coli* Growth in Periodically Oscillating O_2 Environments

Next, *E. coli* was cultivated under oscillating O_2 environments to investigate the effect of O_2 oscillations on bacterial growth. Experiments were performed with various oscillation half periods T' = 60, 30, 10, 5, 2, and 1 min. Fig. 4.17 and 4.18 show representative time series of phase contrast images of *E. coli* cultivated under oscillating O_2 with various *T'*. While noticeable growth was observed from images acquired at longer *T'*, it was more challenging to qualitatively evaluate microbial growth from images acquired at shorter *T'*. Therefore, the growth was quantitatively analyzed from the acquired images and summarized in Fig. 4.19A-F (top: A_{colony}, bottom: instantaneous growth rate $\mu_{\Delta t}$).

In Fig. 4.19A (top), the distinct growth phases under aerobic and anaerobic gassing phases every *T'* = 60 min are evident from A_{colony}. The rate at which A_{colony} increased was further analyzed by $\mu_{\Delta t}$, which is the first derivative of $\ln\left(A_{\text{colony}}\right)$. In Fig. 4.19A (middle), an oscillation-specific growth behavior is revealed, where $\mu_{\Delta t}$ decreases suddenly right after the switch from aerobic to anaerobic gassing phase, much lower (128% decrease) than the growth rate at constant 0% O_2 concentration ($\mu_{0\%}$ = 1.38 ± 0.06 h^{-1}),

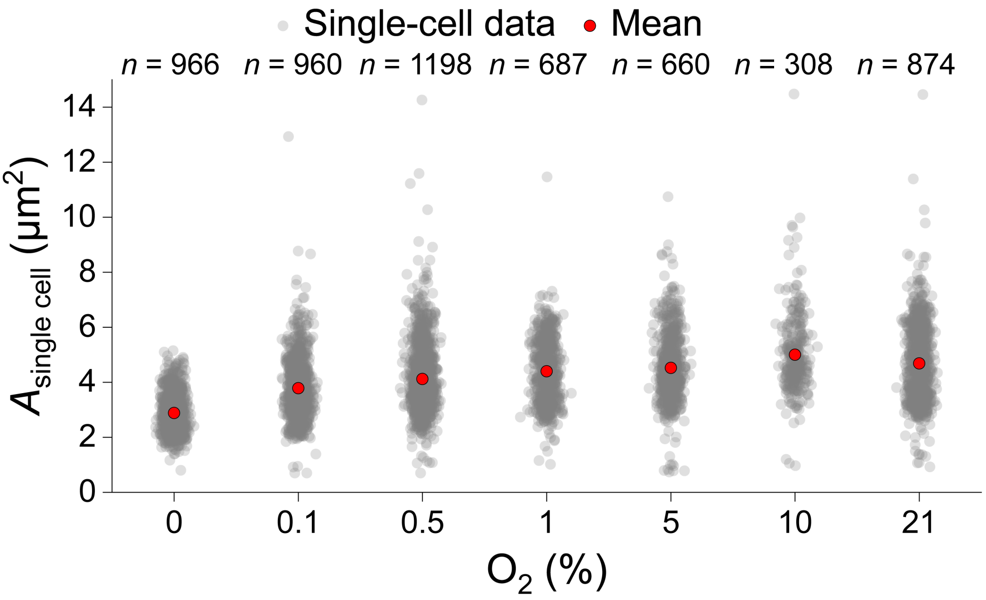

Figure 4.16: Single-cell area ($A_{\text{single cell}}$) under various O_2 supplies at t = 2 h. The gray dots represent single-cell data. Mean is expressed as red dots. The analyzed numbers of cells are presented in the plot.

then gradually increases to reach around $\mu_{0\%}$. Several characteristic values were determined, such as t_{response} (the time to hit the lowest $\mu_{\Delta t}$), and t_{recovery} (the time required to recover up to $\mu_{0\%}$, the reference growth rate obtained under constant conditions), both counting from the switch from aerobic to anaerobic gassing phase. t_{response} and t_{recovery} are determined to be 1.3 ± 0.1 minutes and 35.2 ± 4.9 minutes, respectively. After t_{recovery}, the growth was stabilized around $\mu_{0\%}$ till the end of the anaerobic gassing phase. After the switch from anaerobic to aerobic gassing phase, in contrast, A_{colony} increased rapidly, reaching the growth rate at constant 21% O_2 concentration ($\mu_{21\%} = 1.95 \pm 0.03$ h^{-1}) within a minute.

At T' = 30 min, $\mu_{\Delta t}$ shows a growth tendency similar to T' = 60 min, characterized by the steep decrease right after the switch from aerobic to anaerobic conditions, and the following growth recovery till the end of the anaerobic gassing phase, as shown in Fig. 4.19B. At T' = 10, 5, and 2 min, $\mu_{\Delta t}$ hit the lowest value followed by the gradual recovery phase, but never reached $\mu_{0\%}$, simply due to insufficient time for recovery and adaptation, as shown in Fig. 4.19C-E. In the case of T' = 2 min, only a brief recovery

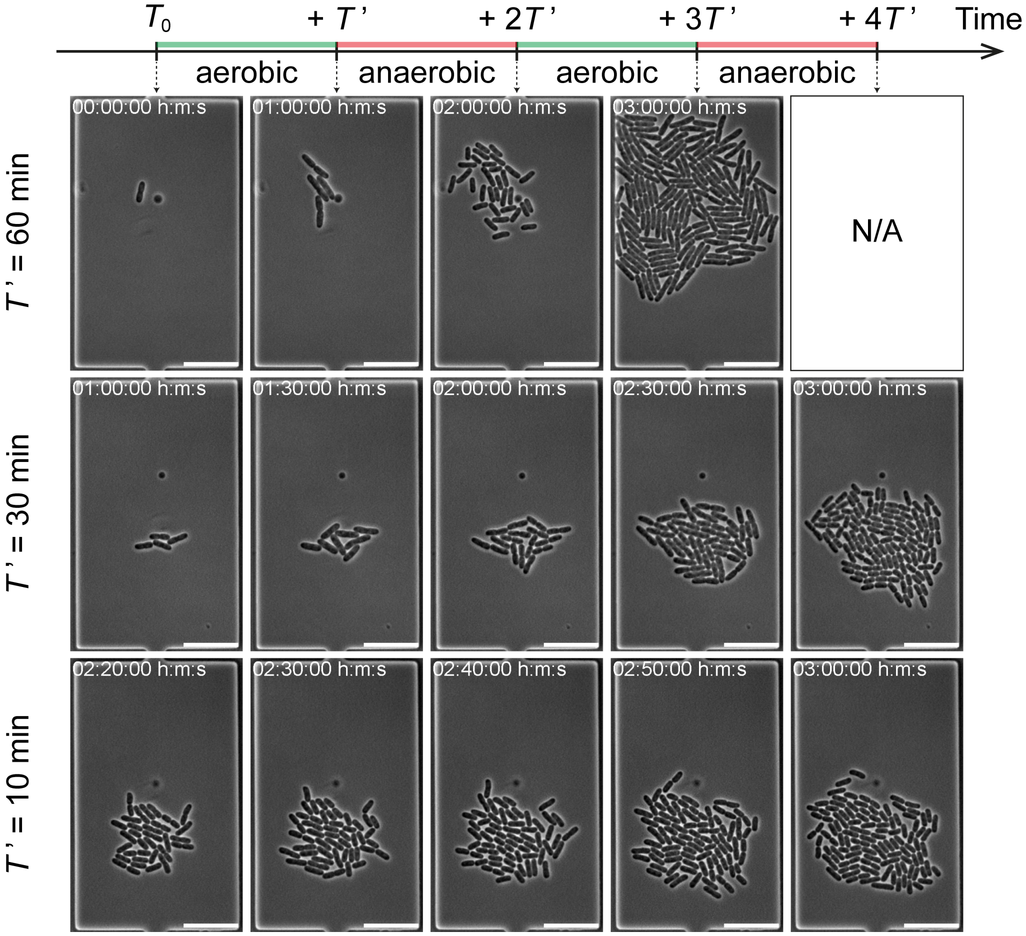

Figure 4.17: Phase-contrast images of *E. coli* cultivated under oscillating O_2 supplies with $T' = 60$, 30, and 10 min (scale bars 10 µm).

phase is observed after the response phase. At T' = 1 min, the steep decrease after the switch from aerobic to anaerobic conditions is observed without a recovery phase, followed by a fast increase right after the switch from anaerobic to aerobic conditions, as shown in Fig. 4.19F. As a result, the $\mu_{\Delta t}$ line plots at T' = 2 min and 1 min represent simpler waveforms (monotonous up and down), compared to the other cases.

The single-cell area also exhibited a distinct increase under aerobic and anaerobic gassing phases. Figure 4.20A-F are plotted with $A_{\text{single cell}}$ obtained from every cell grow-

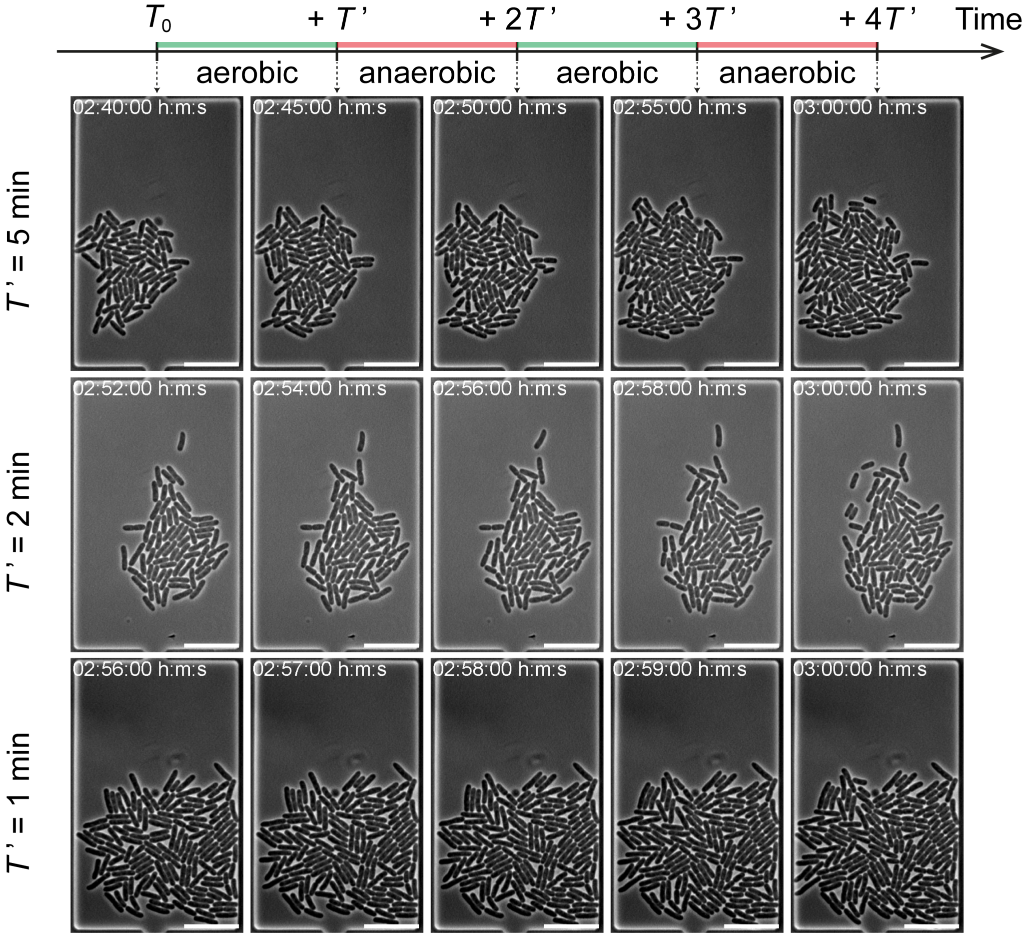

Figure 4.18: Phase-contrast images of *E. coli* cultivated under oscillating O_2 supplies with $T' = 5$, 2, and 1 min (scale bars 10 µm).

ing in a representative chamber of each oscillation condition. Figure 4.20 allows speculating how single cells increase their cell size by following neighboring plots without needing cell tracking that requires more complicated analytical setups. As for overall tendencies, the plots show a faster area increase rate under aerobic than anaerobic gassing phases, similar to colony-area analysis. A quick response in the increase rate was observed right after the gassing phase switch in all the oscillation conditions. An apparent cell area recovery was observed when oscillation half periods were sufficiently long in comparison to t_{response} (T' = 60, 30, and 10 min).

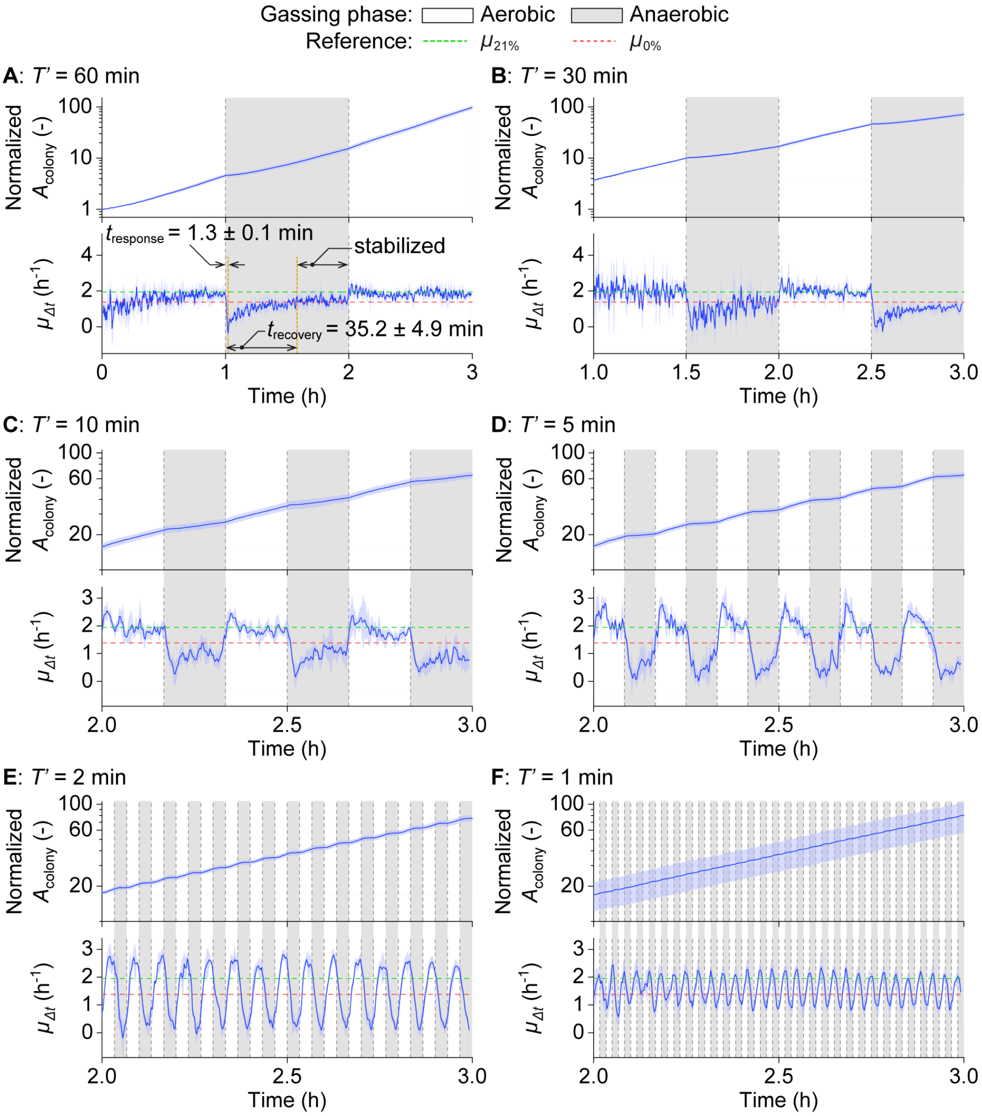

Figure 4.19: *E. coli* growth analysis cultivated under oscillating O_2 supplies. **(A - F)** Growth curves based on colony area (A_{colony}, top) and instantaneous growth rate ($\mu_{\Delta t}$, bottom) over time, under various oscillation half period, T' = 60, 30, 10, 5, 2, and 1 min. Data are expressed as mean ± S.D. n = 5 colonies (60 min), 3 (30 min), 4 (10 min), 4 (5 min), 4 (2 min), 5 (1 min).

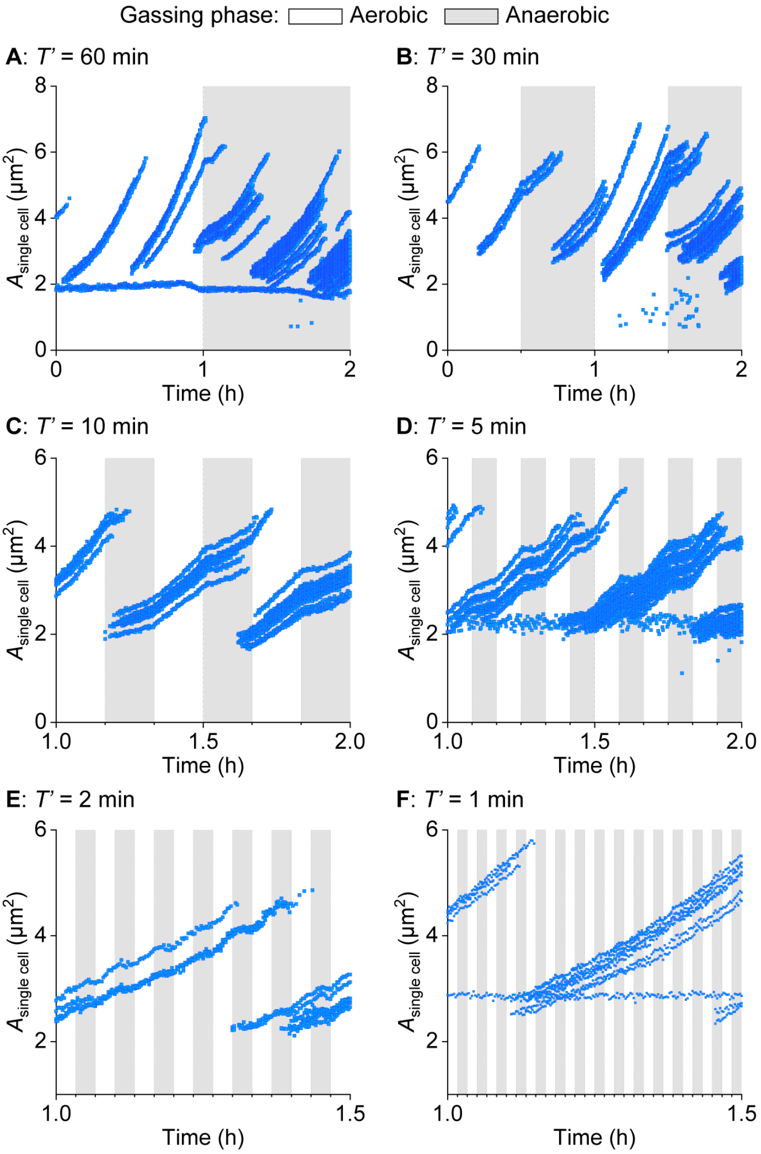

Figure 4.20: Single-cell area ($A_{\text{single cell}}$) plotted over time under oscillating O_2 environments at various oscillation half periods (T').

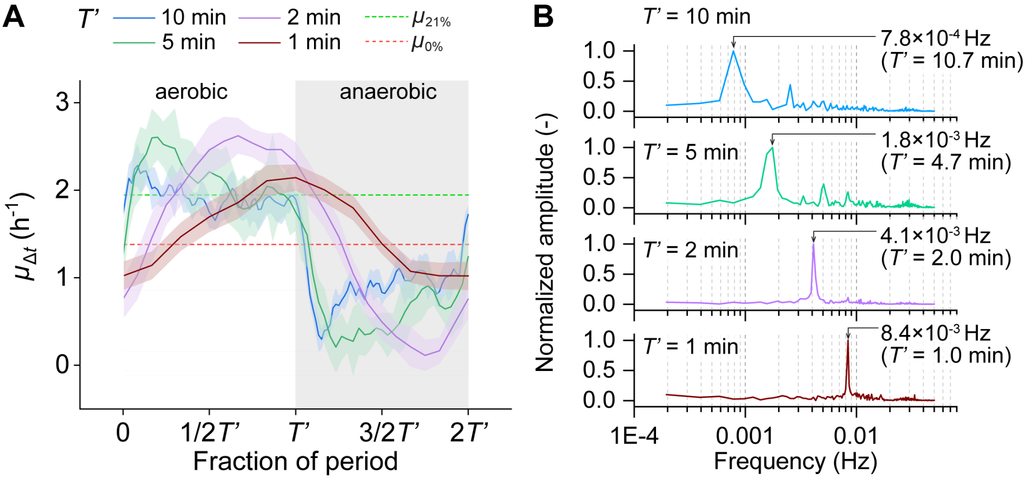

Figure 4.21: Periodic growth dynamics synchronized to applied O_2 oscillations with various *T'*. **(A)** $\mu_{\Delta t}$ across fraction of period (2*T'*). Data are expressed as mean ± S.D. over periods. n = 6 (10 min), 12 (5 min), 30 (2 min), 60 (1 min). **(B)** The frequency spectrum of $\mu_{\Delta t}$ at *T'* = 10, 5, 2, and 1 min determined by the fast Fourier transform (FFT).

4.3.7 Periodic Growth Synchronized with Applied O_2 Oscillations

To compare and examine further the periodic growth behavior induced by different O_2 oscillations, growth data is averaged over periods and plotted over the period fraction, as shown in Fig. 4.21A. Growth data with more than three periods (*T'* = 10, 5, 2, and 1 min) were analyzed.

The periodical comparison suggests that $\mu_{\Delta t}$ line plots from *T'* = 2 and 1 min have simpler waveforms compared to the other *T'* that are longer enough than t_{response}. To examine the waveform complexity of $\mu_{\Delta t}$ line plots at various *T'*, the frequency spectrum of $\mu_{\Delta t}$ line plots were analyzed using the fast Fourier transform (FFT) as shown in Fig. 4.21B. Several frequency peaks were observed at *T'* = 10 and 5 min. These several peaks imply that the complicated waveform of $\mu_{\Delta t}$ line plots from these *T'* are expressed by adding several trigonometric functions due to the existence of response and recovery phases. In contrast, only one frequency peak at *T'* = 2 and 1 min. The single peaks imply that the $\mu_{\Delta t}$ line plots are expressed by simple trigonometric functions, representing only the response phase. Notably, the highest peaks from FFT corresponded to applied

O_2 oscillation half periods *T'*, showing that the periodic growth dynamics were synchronized with applied O_2 oscillation periods (*T'* = 10 min: 7.8×10^{-4} Hz, *T'* = 5 min: 1.8×10^{-3} Hz, *T'* = 2 min: 4.1×10^{-3} Hz, *T'* = 1 min: 8.4×10^{-3} Hz).

The periodic growth behavior can also be visualized and compared with polar plots in a circular coordinate system, as shown in Fig. 4.22. Each point in the plot is defined by a radius ($\mu_{\Delta t}$) and an angle (fraction of period, 2π radian = $2T'$). The polar plot summarizes periodic microbial responses in a single chart, making it useful for pattern recognition. It is recognizable from the polar plots that $\mu_{\Delta t}$ from different periods overlap with each other, showing the reproducible growth behavior over periods.

4.3.8 Distinct Growth Behavior Dependent on Aerobic/Anaerobic Gassing Phases

To further analyze the O_2-oscillation-dependent growth behavior, phase-averaged growth rates were determined under aerobic and anaerobic gassing phases ($\bar{\mu}_{\text{aerobic}}, \bar{\mu}_{\text{anaerobic}}$) by calculating the growth rate for each T', as illustrated in Fig. 4.23A.

In Fig. 4.23B, $\bar{\mu}_{\text{aerobic}}$ and $\bar{\mu}_{\text{anaerobic}}$ for each T' are summarized. At *T'* = 60 min, $\bar{\mu}_{\text{aerobic}}$ and $\bar{\mu}_{\text{anaerobic}}$ are comparable to $\mu_{21\%}$ and $\mu_{0\%}$ respectively, indicating the sufficient recovery time and growth stabilization after the gassing phase shift. At *T'* = 30 and 10 min, $\bar{\mu}_{\text{aerobic}}$ is comparable to $\mu_{21\%}$, but $\bar{\mu}_{\text{anaerobic}}$is below $\mu_{0\%}$. This is due to insufficient recovery time under the anaerobic phases ($t_{\text{response}} < T' < t_{\text{recovery}}$), resulting in an overall lower growth rate over anaerobic phases. This trend became more evident at *T'* = 5 and 2 min, with lower $\bar{\mu}_{\text{anaerobic}}$ because of less time for growth recovery. Interestingly, $\bar{\mu}_{\text{aerobic}}$ was higher than $\mu_{21\%}$ at *T'* = 5 and 2 min. This high $\bar{\mu}_{\text{aerobic}}$ is the result of the steep increase in growth rate right after the switch from anaerobic to aerobic gassing phases and insufficient time to adjust the growth rate to around $\mu_{21\%}$, as shown in Fig. 4.19D and E. Lastly, $\bar{\mu}_{\text{aerobic}}$ and $\bar{\mu}_{\text{anaerobic}}$ at *T'* = 1 min were close to each other, implying the growth adaptation attempt back and forth between aerobic and anaerobic phases, although insufficient time to adapt to either of gassing phases ($T' < t_{\text{response}}$). These results demonstrate a phase- and oscillation-period-dependent growth behavior that can be classified into several cases by growth characteristic values, t_{response} and t_{recovery}.

Furthermore, the phase-averaged growth rates were compared over periods to examine the growth robustness under repeated O_2 oscillations. Growth data with more than 3 periods were analyzed (*T'* = 10, 5, 2, and 1 min). As shown in Fig. 4.23C, $\bar{\mu}_{\text{aerobic}}$ and $\bar{\mu}_{\text{anaerobic}}$ plotted over periods exhibit robust and steady trends, even with repetitive 60 pe-

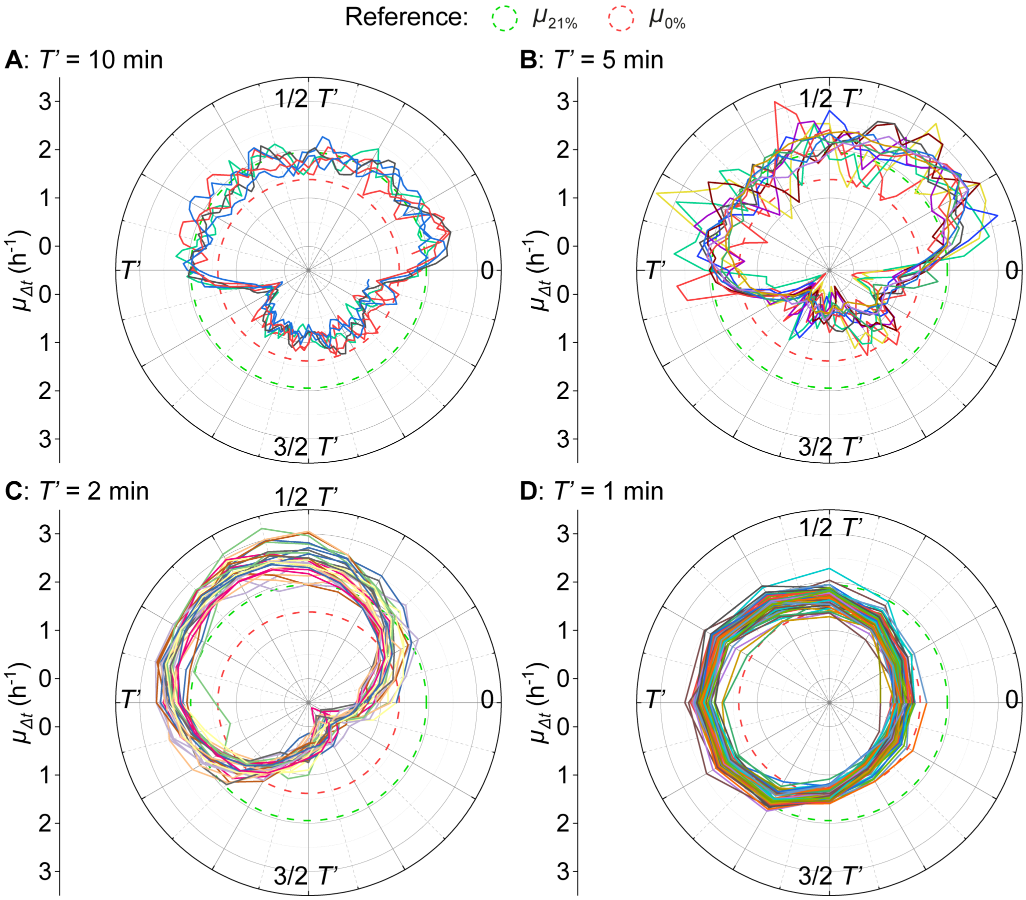

Figure 4.22: Periodic growth dynamics visualized on polar plots. **(A - D)** The instantaneous growth rate $\mu_{\Delta t}$ visualized on polar plots. The angle coordinate represents the fraction of a period (2π radian = $2T'$). Each solid line represents data from each period. The growth rates under constant 21% ($\mu_{21\%}$) and 0% O_2 ($\mu_{0\%}$) are plotted with dashed lines for comparison. The number of solid lines is as follows: 6 (**A**, 10 min), 12 (**B**, 5 min), 30 (**C**, 2 min), 60 (**D**, 1 min).

riods at T' = 1 min. This result indicates the versatility of the developed platform to stably create O_2 oscillating conditions and analyze microbial growth under such conditions.

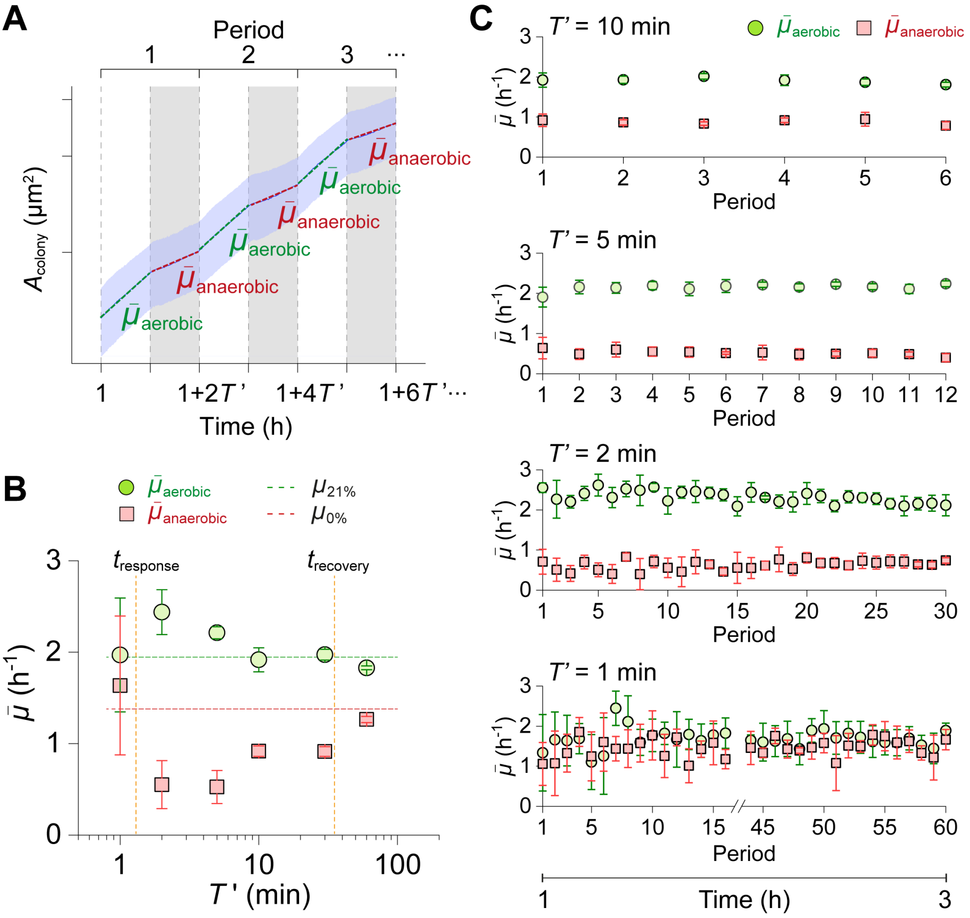

Figure 4.23: Comparison of phase-averaged growth data across different *T'*. **(A)** Phase-averaged growth rates, the average growth rate for each *T'*, are calculated under aerobic gassing phases ($\bar{\mu}_{\text{aerobic}}$) and anaerobic gassing phases ($\bar{\mu}_{\text{anaerobic}}$). **(B)** $\bar{\mu}_{\text{aerobic}}$ and $\bar{\mu}_{\text{anaerobic}}$ at various *T'*. The plotted values are from periods starting at $t = 2$ h. For *T'* = 60 min, values from half-periods starting at $t = 1$ h and 2 h were used for anaerobic and aerobic plots, respectively. The growth rates under constant 21% ($\mu_{21\%}$) and 0% O_2 ($\mu_{0\%}$) are plotted with dashed lines for comparison. **(C)** $\bar{\mu}_{\text{aerobic}}$ and $\bar{\mu}_{\text{anaerobic}}$ over periods showing the robust growth behavior. **(B, C)** Data are expressed as mean ± S.D. n = 5 colonies (60 min), 3 (30 min), 4 (10 min), 4 (5 min), 4 (2 min), 5 (1 min).

4.4 Discussion

This study aimed to investigate the growth dynamics of *E. coli* under fluctuating O_2 environments. Previous research on microbial growth response to gaseous environmental changes was conducted extensively, but only with single shifts of O_2 availability. This restriction has resulted in our limited understanding of microbial growth response to continuously fluctuating environments. To facilitate further investigation, the double-layer microfluidic platform was developed for the time-lapse monitoring of microbes under rapidly oscillating O_2 environments. The platform enabled the cultivation of microbes under well-defined on-chip O_2 oscillating environments and simultaneous observation of microbial behavior at high spatiotemporal resolution. The platform enabled the thorough analysis of the growth dynamics of *E. coli* based on growth rates in different time scales (μ, $\bar{\mu}$, $\mu_{\Delta t}$). While single-cell analysis is known for its high workload required to extract biological information such as growth rates at the single-cell level, it was crucial to establish fully automated image analysis and data extraction before developing the microfluidic device. These analysis procedures enabled quick iteration, adaptation of microfluidic chip prototypes, and direct verification of the effects based on the biological outputs with only overnight delay. This high walkaway time and high throughput experimentation allowed focus primarily on optimizing the microfluidic chip design and experiment preparation while biological insights were automatically extracted. Such a single-cell analysis of continuous microbial growth under oscillating O_2 environments with high temporal resolution was not feasible with conventional analytical platforms.

The thorough growth analysis presented here demonstrates distinct growth dynamics induced by O_2 oscillations, which are characterized by an immediate decrease in $\mu_{\Delta t}$ after the switch from aerobic to anaerobic gassing phases (response), followed by gradual increase (recovery), and later stabilized state. These distinguished cell behaviors occur depending on oscillation half periods *T'*. This is reasonable, considering that the change from one metabolic pathway to another requires a series of biological events, such as signal transduction (in milliseconds), enzymatic reaction (in seconds), transcription (in minutes), and translation (in minutes), occurring at different time scales [68, 128, 129]. For example, the O_2 oscillation with *T'* = 1 min was sufficient to rapidly and strongly decrease the *E. coli* growth rates in the respective anaerobic gassing phase (Fig. 4.19F). This observation could be explained by the rapid depletion of the adenosine triphosphate (ATP) pool under O_2 limitation, which occurs within the time scale of microbial responses to environmental fluctuations associated with enzymatic reactions and metabolite turnover under minute [68]. A recurring increase in the *E. coli* growth rates were observed when $T' > t_{\text{response}}$ (Fig. 4.19A-D). This adaptation to prolonged anaerobic phases is most likely the result of specific regulatory processes that alter gene expression patterns, leading to a gradual change in cell metabolism in minutes [37]. Under the switch from anaerobic to aerobic gassing phases, the initial peak and the subsequent gradual decrease of $\mu_{\Delta t}$ was also observed. This temporal change in growth rate may be attributed to transient accumulation or excretion of metabolites due to maintaining homeostasis upon the gaseous transition in minutes [35, 130]. Lastly, the FFT and phase-averaged growth rate analyses revealed periodic and robust growth dynamics synchronized with the applied O_2 oscillation periods. This result implies the cellular capability to respond and adapt to corresponding extracellular O_2 environments and highlights the importance of O_2 in determining cellular growth behavior. Regarding the metabolic switching under aerobic and anaerobic conditions, hybrid metabolism has been reported under microaerobic conditions, where both aerobic and anaerobic metabolisms are utilized [37, 131]. Therefore, metabolic switching is a continuous process that may not be clearly divided into aerobic and anaerobic states. Rather, the switching time of *E. coli* can be characterized and determined by various biological events, as mentioned earlier. For instance, the timescales of enzymatic reaction, transcription, and translation would fit this study. Follow-up studies would be valuable to further investigate the correlation between the biological timescales and O_2 fluctuation timescales.

The demonstrated experiment and analysis platform can be strengthened with further improvements. In the developed platform, we measured the fluorescence lifetimes at 0% and 0.1% O_2, which can be distinguished from each other. However, no further measurements in the range below 0.1% have been conducted. Obviously, O_2 sensing with the O_2 indicator and FLIM has its limits in terms of sensitivity, which is a complex technical issue that depends on several parameters. For example, the measurement may be affected by the accuracy and resolution of the O_2 control. A set of mass flow controllers connected to pure N_2 and O_2 gas supply was used in the setup, which also has limitations in resolution, especially at lower O_2 concentrations below 0.1%, where the mass flow rate has to be set very low compared to an ideal operating range. A follow-up study should consider using a gas supply with a lower O_2 concentration (for instance, 1%) instead of pure O_2 gas so that the mass flow controller can operate in the recommended flow range when controlling O_2 concentrations below 0.1%. FLIM and the O_2 sensing dye can be characterized with such an improved setup for O_2 control. Finally, sensitivity can be determined with finer resolution at low O_2 concentrations. Another factor is the two-point calibration at known O_2 availability. This calibration was done by flushing synthetic air containing either 0% or 21% of O_2. While controlling the O_2 availability to 21% was credible, achieving a strict O_2 control at 0% remained challenging due to potential disturbances from high air permeability and the possibility of residual air remaining within the PDMS. By improving the calibration method to ensure strict 0% O_2 availability, such as by using chemical O_2 scavengers [91, 92, 132] compatible with the O_2-sensitive chemical or by using a mini-incubator that allows flushing O_2 depleted gas around the PDMS chip [103], more precise on-chip O_2 control and sensing under anaerobic conditions may be possible to achieve.

The developed device and the finding regarding microbial behavior under O_2 fluctuation have the potential to be applied to a wide range of research fields. Regarding practical applications, the findings help characterize and improve industrial bioprocesses. The fluctuating environments resulting from heterogeneous conditions in large-scale bioreactors have been widely reported, which result in unexpected inefficiency and yield losses [24–26]. Such fluctuations in industrial bioreactors, specifically O_2 fluctuations, can occur in a time range below one minute [27]. To address this issue, it is of the utmost importance to further understand microbial behavior under rapidly fluctuating environments. The developed device provides an on-chip environment miming rapid O_2 fluctuations inside bioreactors. This enables the analysis of O_2 fluctuation-specific microbial behavior, including the emerging phenotypic heterogeneity at single-cell resolution, which was previously impossible.

A comparable approach to recreate fluctuating O_2 environments and live-cell imaging could also prove beneficial in fundamental biology and biomedicine. For instance, it is of interest to investigate pathogenic microorganisms (for example, *Salmonella typhimurium*) and their mechanism on virulence expression and host-cell infection. It has been recognized that pathogens use O_2 as a signal to trigger their virulence, yet the underlying mechanism is elusive [32, 133]. Our analysis platform provides an optimal environment for such a study, where microbial behavior can be resolved at single-cell resolution under a well-defined O_2 environment. Another example is to study the interaction of gastrointestinal host cells and microbial communities under fluctuating O_2 environments. There has been growing evidence that O_2 dynamics play a pivotal role in maintaining intestinal homeostasis [134, 135]. The intricate regulatory mechanisms at the interface of host cells and the microbiome and the role of O_2 are of great interest since these interactions are linked to various diseases [135]. Moreover, several reports imply the existence of O_2 fluctuations in the intestine and the intestinal epithelial-microbiome interface that arise from periodic ingestion of nutrients or intermittent changes in O_2 availability in the blood [136–138]. Based on these previous reports, it is reasonable to assume that the timescale of O_2 fluctuations for gut microbiome would be in the range of hours. In fact, previous research reported fluctuating bacterial abundance in wild meerkats throughout the day, with the relative abundance of aerobic (*Cellulomonas*) and anaerobic microbes (*Clostridium*) varying due to changes in O_2 availability during that time [139]. The presented device and analysis could be applied to study the interplay between host epithelial cells and microbiomes by emulating such an O_2 fluctuating environment.

5 Investigating Growth of *C. glutamicum* under Oscillating Oxygen Environments

In Chapter 4, the double-layer microfluidic device enabling precise and rapid O_2 control was presented. Here in Chapter 5, the device is used to investigate anaerobic growth of *Corynebacterium glutamicum* (*C. glutamicum*), showcasing the use-case of the developed device and its advantage over conventional cultivation setups.

5.1 Introduction

C. glutamicum is a gram-positive bacteria often used for industrial amino acid production such as glutamate and lysine [140, 141]. While *C. glutamicum* produces amino acids in the presence of O_2, it is also known as a facultative anaerobe capable of growing anaerobically by nitrate respiration or fermentation [142–144]. *C. glutamicum* utilizes carbon sources like glucose under anaerobic conditions in the absence of nitrate, producing fermented products such as lactate, acetate, and succinate, which can be used as bio-based plastic monomers (Fig. 5.1, [145]). Depending on the O_2 availability, *C. glutamicum* uses different metabolic pathways, leading to different products. Therefore, it is important to understand the O_2-dependent growth of *C. glutamicum* and the resulting products for achieving efficient industrial bioprocessing.

Considering the heterogeneous environment often observed in industrial bioreactors [24–27], *C. glutamicum* is assumed to encounter different ranges of O_2 availability during cultivation. This is not trivial since such a fluctuating environment can affect cell growth and production yield. However, there is currently little knowledge on how such a fluctuating O_2 environment affects the growth of *C. glutamicum* and how cells respond and adapt to such conditions.

Therefore, in this chapter, the growth of *C. glutamicum* ATCC 13032 under oscil-

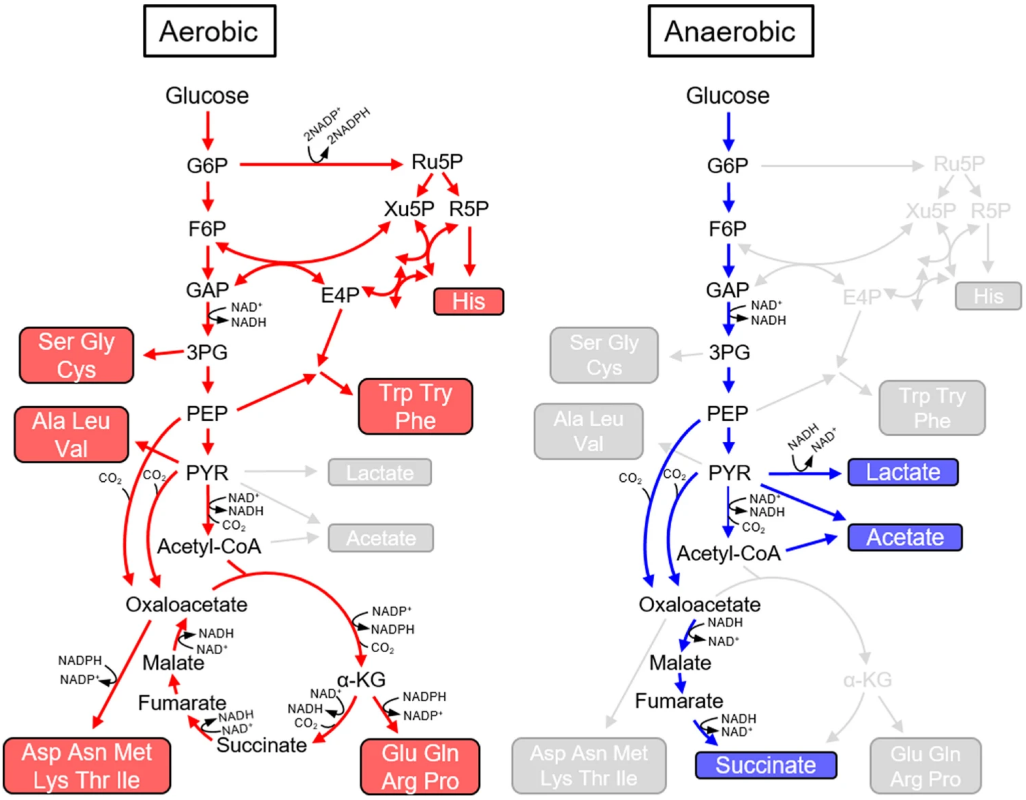

Figure 5.1: Metabolic pathways in *C.glutamicum* under aerobic and anaerobic conditions. Grey pathways suggest that they are not used. Abbreviations are defined as follows: G6P, glucose 6-phosphate; F6P, fructose 6-phosphate; GAP, glyceraldehyde 3-phosphate; 3PG, 3-phosphoglycerate; PEP, phosphoenolpyruvate; PYR, pyruvate; Ru5P, ribulose 5-phosphate; R5P, ribose 5-phosphate; Xu5P, xylulose 5-phosphate; E4P, erythrose 4-phosphate; α-KG, α-ketoglutarate (adapted with permission from [145]).

lating O_2 environments is examined using the developed double-layer microfluidic platform. According to a previous report that investigated anaerobic growth of *C. glutamicum* [144], the anaerobic growth was negligible only with glucose, but supplementation of tryptone or peptone improved growth strongly ($\mu = 0.10 \pm 0.01$ h^{-1} with 15 g/L tryptone). Moreover, adding a mixture of amino acids also rescued the growth ($\mu = 0.10 \pm 0.01$ h^{-1}). Based on this previous study, several conditions are tested: (i) without supplement, (ii) with peptone, and (iii) with amino acids. Growth rates (instantaneous and phase-averaged) are calculated to analyze aerobic/anaerobic growth and growth response to the repeated gassing switch. This chapter aims to showcase the application of the double-layer microfluidic chip to different microorganisms and to prove the platform's versatility for broad research purposes.

5.2 Materials and Methods

5.2.1 Medium and Cell Preparation

C. glutamicum ATCC 13032 was stored in a ROTI Store cryo vial. Brain heart infusion (BHI) complex medium was prepared by suspending 37 g (BD, US) in 1 L distilled water and autoclaving. Standard CGXII minimal medium was supplemented with 20 g/L glucose (Carl Roth, Germany) [146].

The cultivation was performed in three steps: two pre-cultures and a main culture. The first pre-culture was initiated by transferring a single ROTI bead to a 20 mL BHI medium and cultured at 30°C, 120 rpm for around 8 hours. 1 mL from the first pre-culture was inoculated to the second pre-culture with CGXII medium. After overnight cultivation, the main culture with CGXII was initiated by inoculating the second pre-culture with an initial optical density of 0.2. The main culture was cultivated for around 6 hours to reach an optical density of 1 to 1.5. When supplementing CGXII with peptone, 15 g/L (Carl Roth, Germany) was added to the CGXII medium. In the case of amino acids supplementation, 20 essential amino acids were supplemented in a concentration of 0.8 mM. Amino acids are as follows: alanine, arginine, asparagine, aspartate, cysteine, glutamine, glutamate, glycine, histidine, isoleucine, leucine, lysine, methionine, phenylalanine, proline, serine, threonine, tryptophan, tyrosine, valine.

5.2.2 Microfluidic cultivation, Imaging, and Growth Analysis

C. glutamicum cultivation in the double-layer microfluidic chip, microscopic time-lapse imaging, and subsequent image analysis were performed as described in Chapter 4 unless otherwise mentioned. An optical density of around 1 was used to inoculate the chip. Images were acquired every 5 minutes. *C. glutamicum* was cultivated under aerobic conditions for the first hour, followed by aerobic and anaerobic gassing oscillations. Growth was therefore analyzed and plotted starting from one hour for all the conditions. Response time to the anaerobic gassing phase was determined from the second period of mean instantaneous growth rates ($\mu_{\Delta t}$).

5.2.3 Statistical Analysis

Statistical analyses were performed using the Student's t-test. A value of $p < 0.01$ was considered significant.

5.3 Results

5.3.1 *C. glutamicum* Growth in Oscillating O_2 Environments

To examine the *C. glutamicum* growth under aerobic, anaerobic, and switching regimes, on-chip cultivation was performed with the double-layer microfluidic platform. Here, three conditions were examined: (i) without supplements (control in figures), (ii) with peptone (+ peptone), and (iii) with amino acids (+ amino acids). The durations of aerobic and anaerobic cultivations were (i, ii) 0.5 h/2 h and (iii) 1 h/ 5 h, respectively. In Fig. 5.2, phase-contrast images of *C. glutamicum* are shown along with time. As expected, *C. glutamicum* formed larger colonies with the supplementation of peptone or amino acids, as anaerobic growth of *C. glutamicum* was improved, whereas *C. glutamicum* was unable to grow under anaerobic conditions solely on glucose.

To investigate further the aerobic/anaerobic growth in a time-resolved manner, the colony area (A_{colony}) and the instantaneous growth rate ($\mu_{\Delta t}$) were determined and plotted in Fig. 5.3 (control, + peptone, + amino acids).

It is visible from the growth curves based on A_{colony} (Fig. 5.3, top) that A_{colony} increases at different rates under aerobic and anaerobic gassing phases, for all three conditions. The *C. glutamicum* growth improved by supplementing either peptone or amino acids, resulting in larger colony areas after 13 hours of cultivation. The growth rate was further analyzed in a temporally resolved manner by calculating $\mu_{\Delta t}$ (Fig. 5.3, bottom). Apparent differences in $\mu_{\Delta t}$ under aerobic and anaerobic gassing phases were observed for all three conditions.

To compare the difference in growth rate under aerobic/anaerobic gassing phases and with different supplements, the phase-averaged growth rates for aerobic and anaerobic gassing phases ($\bar{\mu}_{\text{aerobic}}$ and $\bar{\mu}_{\text{anaerobic}}$) were calculated. As shown in Fig. 5.4, both $\bar{\mu}_{\text{aerobic}}$ and $\bar{\mu}_{\text{anaerobic}}$ exhibit the lowest values for control samples without supplements, with $\bar{\mu}_{\text{aerobic}} = 0.40 \pm 0.08\ \text{h}^{-1}$ and $\bar{\mu}_{\text{anaerobic}} = 0.02 \pm 0.01\ \text{h}^{-1}$. Improved growth was confirmed using the Student's t-test for the sample supplemented with amino acids (+ amino acids), with $\bar{\mu}_{\text{aerobic}} = 0.56 \pm 0.08\ \text{h}^{-1}$ and $\bar{\mu}_{\text{anaerobic}} = 0.06 \pm 0.01\ \text{h}^{-1}$. Further

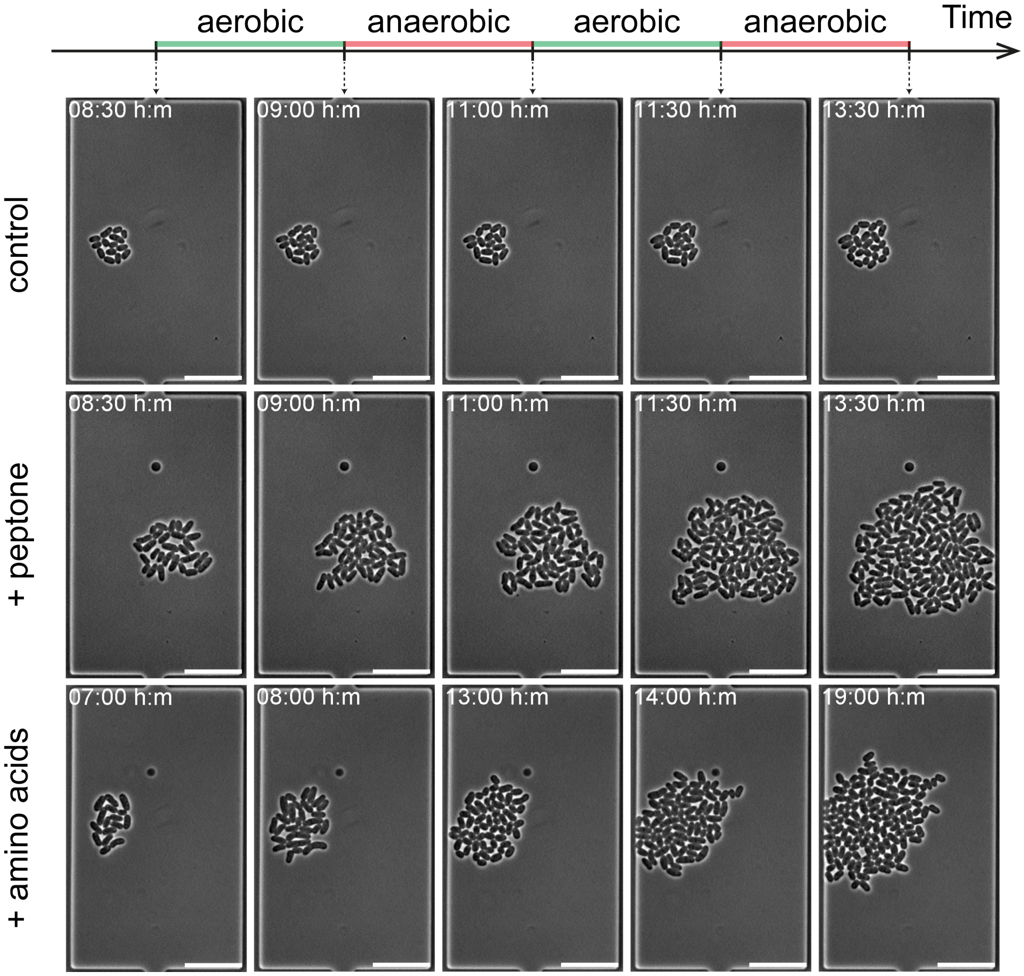

Figure 5.2: Phase-contrast images of *C. glutamicum* cultivated under oscillating O_2 supplies, with/without supplementing peptone or amino acids. The aerobic/anaerobic durations are 0.5 h/2 h for control and peptone, whereas 1 h/5 h for amino acids (scale bars 10 µm).

improved growth was also statistically confirmed for the sample supplemented with peptone (+ peptone), with $\bar{\mu}_{\text{aerobic}} = 0.96 \pm 0.07\ \text{h}^{-1}$ and $\bar{\mu}_{\text{anaerobic}} = 0.12 \pm 0.01\ \text{h}^{-1}$.

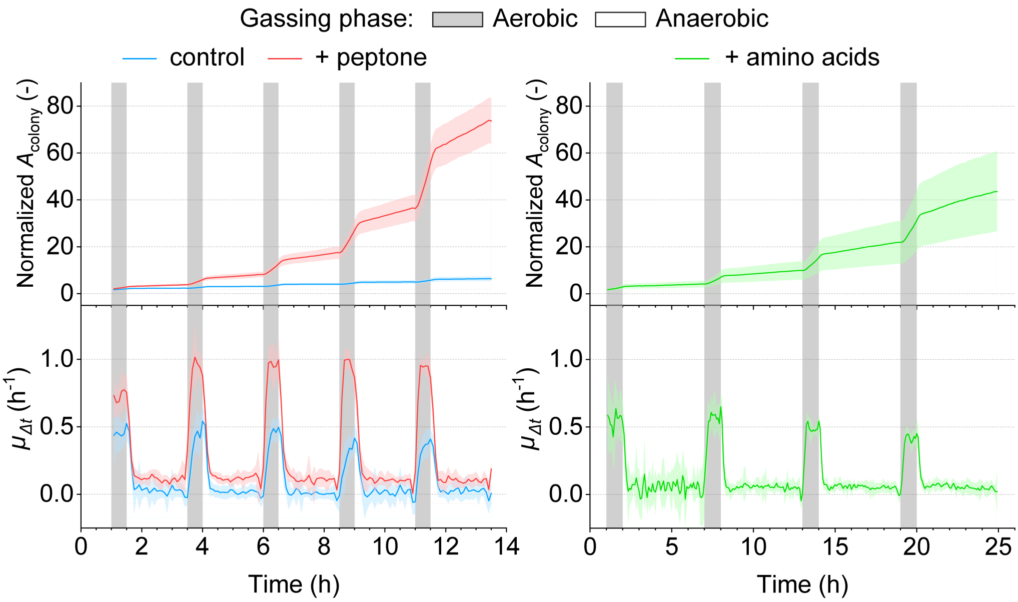

Figure 5.3: *C. glutamicum* growth analysis cultivated under oscillating O_2 supplies. Growth was evaluated by growth curves based on colony area (A_{colony}, top) and instantaneous growth rate ($\mu_{\Delta t}$, bottom) over time. Data are expressed as mean ± S.D., n = 31 colonies (control), 16 (+ peptone), 13 (+ amino acids).

5.3.2 Cell Size Development at Single-Cell Level

To investigate the growth dynamics of *C. glutamicum* at the single-cell level, single-cell areas ($A_{\text{single cell}}$) from single representative colonies from three conditions were plotted as shown in Fig. 5.5. The single-cell area development is visible under aerobic gassing phases for control samples (Fig. 5.5A). Still, there is almost no area gain under the anaerobic gassing phases. When the medium is added with peptone or amino acids (Fig. 5.5B, C), a more substantial increase in single-cell area is observed under both gassing phases. These results prove that the distinct growth behavior under oscillating O_2 conditions, as revealed in Fig. 5.3 at the population level, is the accumulation of growth behavior alteration at the single-cell level. The heterogeneous growth in a single colony can also be analyzed, making this experimental platform more suitable for heterogeneity studies than conventional cultivation setups.

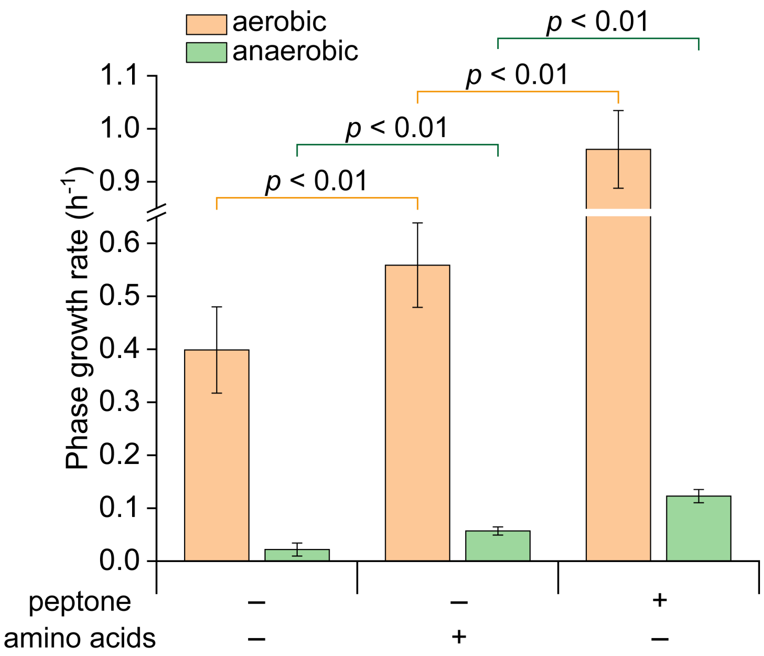

Figure 5.4: Comparison of phase-averaged growth rates with different supplements. The plotted values are from the second period. Data are expressed as mean ± S.D., $n = 31$ colonies (control), 16 (with peptone), 13 (with amino acids).

5.4 Discussion

This chapter investigated the growth of *C. glutamicum* under oscillating O_2 conditions using the developed double-layer microfluidic platform. The *C. glutamicum* cultivation and the following image analysis were performed successfully, proving the versatility of the developed experimental platform for diverse applications with various microorganisms. The growth rate analysis showed improved *C. glutamicum* growth when the medium was supplemented with peptone or amino acids.

The use of the developed platform enables an efficient experimental design. In a previous study, a 1.4 L bioreactor containing 600 mL medium was used for one condition, leading to a large volume of samples being consumed [144]. Moreover, the dynamic O_2 control is practically difficult to achieve, limiting the growth investigation to only under constantly maintained gaseous conditions. The developed platform requires only a small volume of medium (100 nL/min × 24 hours = 144 µL/day) and achieves precise growth

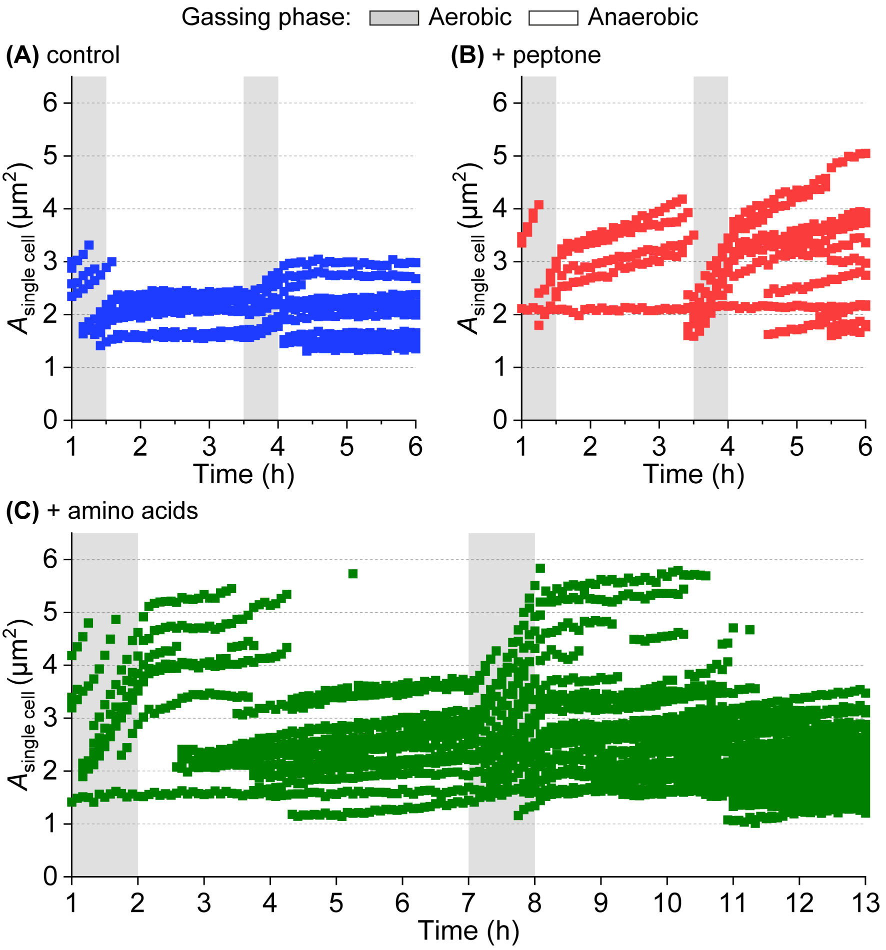

Figure 5.5: *C. glutamicum* single-cell area ($A_{\text{singlecell}}$) plotted over time under oscillating O_2 environments for **(A)** control, **(B)** with peptone, and **(C)** with amino acids.

rate analysis. Also, the platform enables introducing oscillating O_2 conditions, making it a suitable platform for investigating microbial growth in various settings. The growth analyses at the population and single-cell levels provide a comprehensive perspective on microbial growth at different scales.

Potential future work involves using the obtained growth data for growth modeling. With precise growth data from different O_2 availabilities and oscillations, a growth model might be extended from a steady-state model to a time-dependent model capable of describing the cellular response to fluctuating O_2 conditions. This would benefit not only fundamental microbiology research but also industrial bioprocessing development. As such, a new growth model allows a finer estimation of cell growth in an often environmentally heterogeneous bioreactor.

6 Microfluidic Chip Development for Spatial Oxygen Control

The spatial O_2 environment in nature is crucial for microbial behavior and interactions and in shaping diverse microbial communities. However, many aspects of spatially structured microenvironments impacting microbial communities remain poorly understood. An innovative approach to studying these O_2 microenvironments involves using microfluidic devices. This technology enables the precise reproduction of specific O_2 environments found in nature, allowing for the observation and analysis of how microorganisms adapt to these conditions and form communities. Specifically, by artificially constructing environments with O_2 gradients, various research questions can be addressed, such as: How do microorganisms adjust their spatial distribution in response to O_2 gradients? How does O_2 supply influence microbial interactions and competition? How does O_2 availability contribute to forming symbiotic relationships and metabolic cooperation in constrained environments? In addition to recreating spatial O_2 microenvironments, achieving high-throughput analysis of microbial behavior under various O_2 conditions is a critical challenge for efficient experiment execution.

This chapter discusses the development of microfluidic devices to replicate O_2 microenvironments and achieve high-throughput analysis. The primary focuses are on the fabrication, principles, preliminary O_2 control experiments, and outlooks for microbial single-cell analysis in spatiotemporal O_2 environments.

6.1 General Concept

PDMS, a primary material used for microfluidics, is known for its high air permeability. Leveraging this property, gas control in microfluidic chips is often based on gas diffusion. Several diffusion-based spatial O_2 control approaches have been explored in this chapter, as illustrated in Fig. 6.1. Four different chip designs are characterized in the following sections: (i) side gas channels, (ii) a double-layer chip with large gas channels (mm-

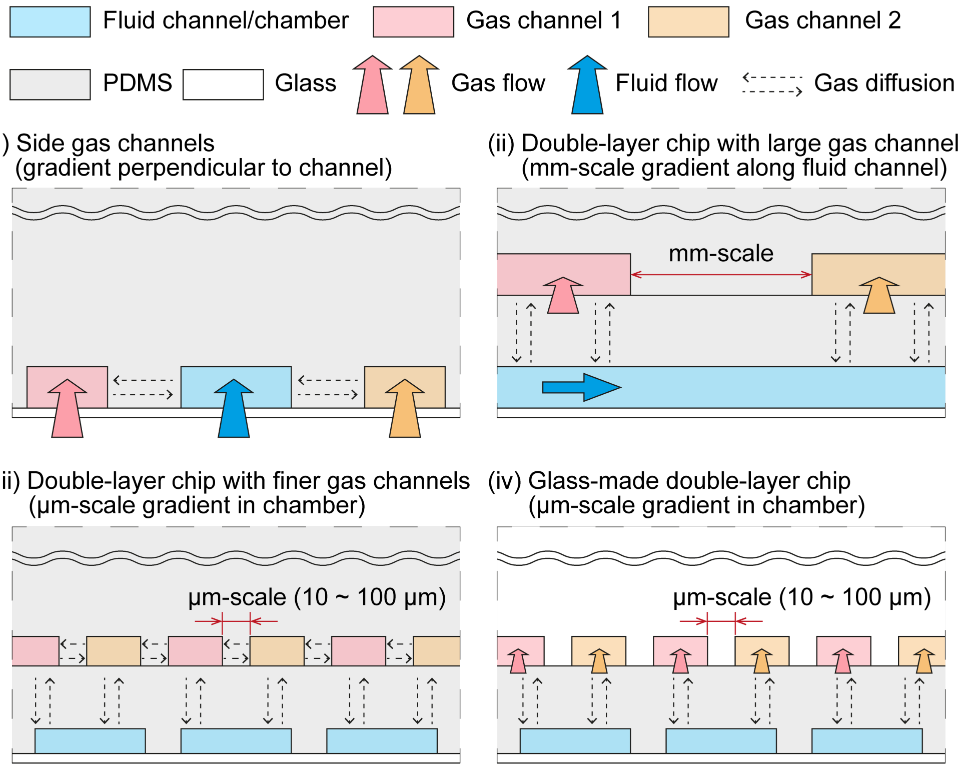

Figure 6.1: Different approaches for spatial O_2 control in the fluid channel and chambers.

scale), (iii) a double-layer chip with finer gas channels (µm-scale), and (iv) a double-layer chip with a glass-made top layer. Starting with side gas channels, the design is developed into a double-layer system to enable high-throughput and finer spatial control. In the final design, glass is introduced as a material for the top layer to achieve better O_2 control.

6.2 Design 1: Side Gas Channels

6.2.1 Technical Concept

The first approach is to prepare side gas channels adjacent to the fluid channel as illustrated in Fig. 6.2. In this setting, gas in the gas channels diffuses through the PDMS walls into the fluid channel. By flushing different gases with different O_2 concentrations in two side channels, an O_2 gradient can be structured perpendicularly to the fluid channel and

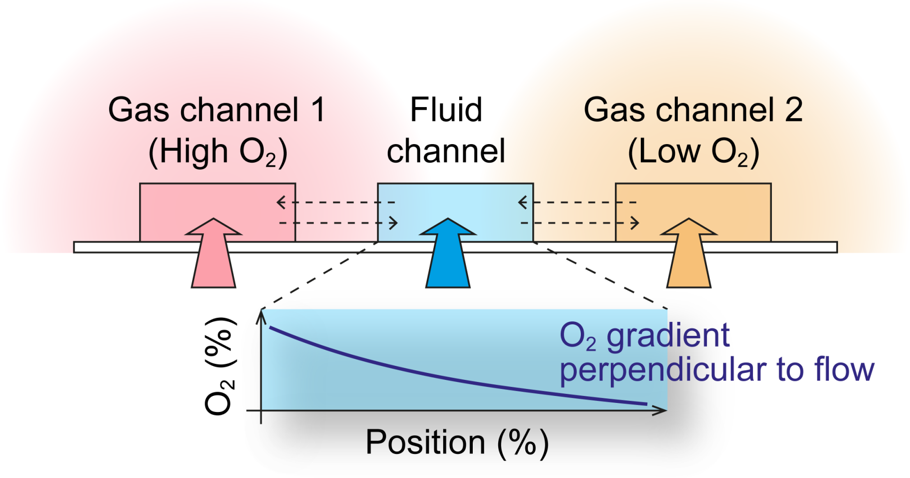

Figure 6.2: Conceptual illustration of spatial O_2 control with side gas channels.

chambers. One of the advantages of this approach with side gas channels is its ease of fabricating PDMS chips, as it only requires PDMS molding on a master mold with microstructures. The drawback is that the side-gas channels have to be designed before the master mold fabrication, limiting the flexibility in designing. Another drawback is the inefficiency of gas diffusion. The height of a standard microfluidic chip for microbial single-cell analysis is around 10 µm for fluid channels and about 1 µm for fluid chambers. Thus, the surface area for gas exchange is relatively small, leading to inefficient gas diffusion. Still, this approach is simple and straightforward and, therefore, has been applied broadly [53, 147].

6.2.2 Materials and Methods

Chip Preparation

The chip used in Chapter 3 was used for testing spatial O_2 control using side gas channels. The chip was prepared as described in Chapter 3.2.1, with a detailed design in Fig. 3.2.

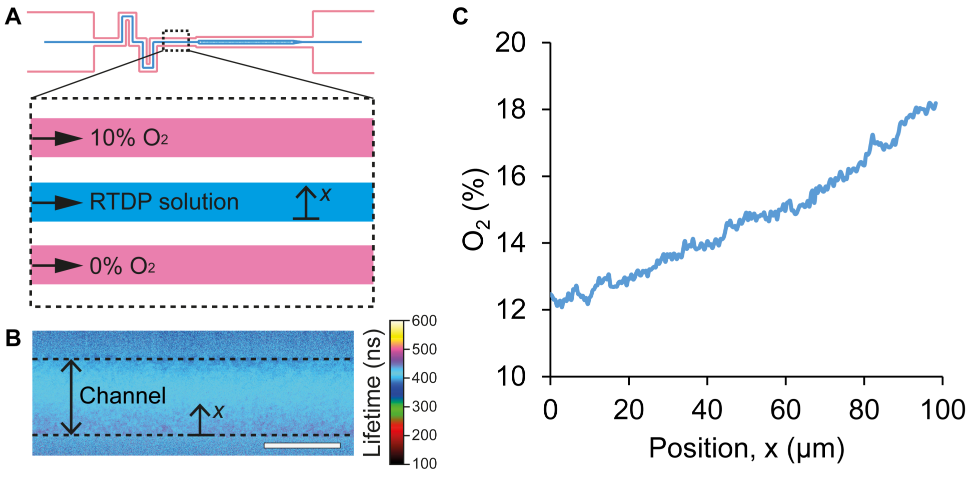

Figure 6.3: O_2 gradient in the fluid channel with side gas channels. **(A)** Gassing setting in the side gas channels. **(B)** FLIM image showing lifetime gradient across the channel width (scale bar 100 μm). **(C)** Determined O_2 gradient across the fluid channel.

O_2 Control and Sensing

O_2 was controlled by adjusting the volumetric ratio of O_2 and N_2, with 5 mL/min total mass flow rate in each gas channel. FLIM imaging and associated referencing, O_2-sensitive sensor (RTDP) calibration, and image analysis were performed as described in Chapter 4 unless otherwise mentioned. The temperature was set to 25°C. A 20X objective lens (Plan Apo λ, Nikon, Japan) was utilized for O_2 sensing in channels. The RTDP calibration yielded $K_q = 2.58$. RTDP solution of 3 mM was perfused at a constant flow rate of 400 nL/min.

6.2.3 Results

O_2 gradient was structured in the fluid channel using the side gas channels as depicted in Fig. 6.3A. Gases with different O_2 concentrations (10% and 0%) were flushed through the side channels. RTDP solution was perfused in the fluid channel for O_2 sensing. Fig. 6.3B shows a FLIM image of RTDP in the fluid channel with pseudo coloring based on fluorescence lifetime, from which a gradient is observed in the perpendicular direction of the channel. The O_2 concentration was determined from the lifetime image as depicted in

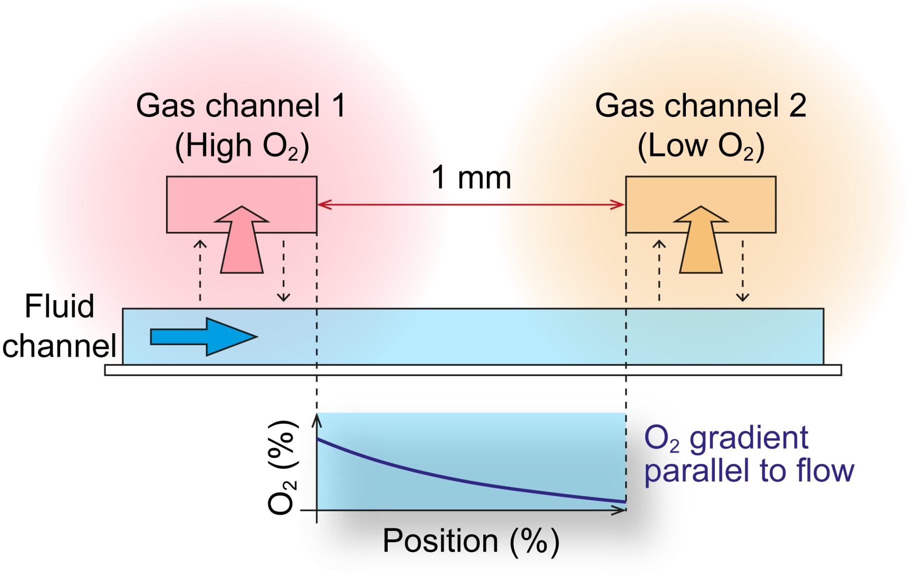

Figure 6.4: Conceptual illustration of spatial O_2 control with large gas channels in the double-layer chip for high throughput.

Fig. 6.3C. The gradient in the fluid channel started from 12% and increased up to 18% on the other side of the channel. The measured O_2 concentrations were higher than the applied O_2 concentrations by about 10%. This could be explained by the air diffusion from the surrounding PDMS into the fluid. Although the gradient was structured, the effect of air diffusion was high, resulting in different O_2 conditions from applied conditions.

6.3 Design 2: Double-Layer Chip with Large Gas Channels for High Throughput

6.3.1 Technical Concept

The following approach is the double-layer microfluidic chip introduced in Chapter 4. The exchangeable top layer design has various advantages over a bulk PDMS chip, such as flexibility in design and large surface area for gas diffusion compared to side-gas channels. To recreate a mm-scale O_2 gradient over the chip, two separate gas channels are designed in the top layer. This allows gas diffusion from each gas channel into the beneath fluid channels/chambers, creating an O_2 gradient along the fluid channel (Fig. 6.4). Two gas channels are supplied with gases with different O_2 concentrations. The gas in the gas channels diffuses into the fluid channel, creating an O_2 gradient parallel to the flow in the fluid channel. The first purpose of testing the double-layer chip with large gas channels at the mm scale is to examine whether the double-layer chip system can spatially control O_2. However, such an mm-scale O_2 gradient along the fluid channel would allow controlling O_2 concentrations in a gradient manner over a series of cultivation chambers, enabling high-throughput analysis where microbial growth under various O_2 concentrations is investigated in one experiment. Therefore, this design is not only for validating the diffusion-based O_2 control concept but also for achieving high-throughput analysis.

6.3.2 Materials and Methods

Chip Preparation

The chip described in Chapter 4.3.1was utilized. The chip was prepared as described in Chapter 4.2.1, with a detailed design in Fig. 4.8C, D.

O_2 Control and Sensing

O_2 was controlled by adjusting the volumetric ratio of O_2 and N_2 with a total flow rate of 20 mL/min in each gas channel. Unless otherwise mentioned, FLIM imaging and associated referencing, RTDP calibration, and image analysis were performed as described in Chapter 4. The temperature was set to 37°C. A 20X objective lens (Plan Apo λ, Nikon, Japan) was utilized for O_2 sensing in channels. The RTDP calibration yielded $K_q = 2.68$. RTDP solution of 3 mM was perfused at constant flow rates at 400 nL/min.

6.3.3 Results

The double-layer chip with two separated large gas channels was utilized, as shown in Fig. 6.5. Figure 6.6 depicts chip observation and O_2 measurement using microscopy. A phase-contrast image is shown in Fig. 6.6A, where the fluid channels, chambers, and top gas channels are observed. The FLIM image of RTDP in the fluid channel is depicted in Fig. 6.6B (Gas_2: 20% O_2). It is visible from the FLIM image that an O_2 gradient was structured in parallel to the fluid channel. The O_2 availability was finally determined from the FLIM image as shown in Fig. 6.6C. The O_2 gradient initially started from 0%, then linearly increased up to 10% or 20%. These results prove that a mm-scale O_2 gradient

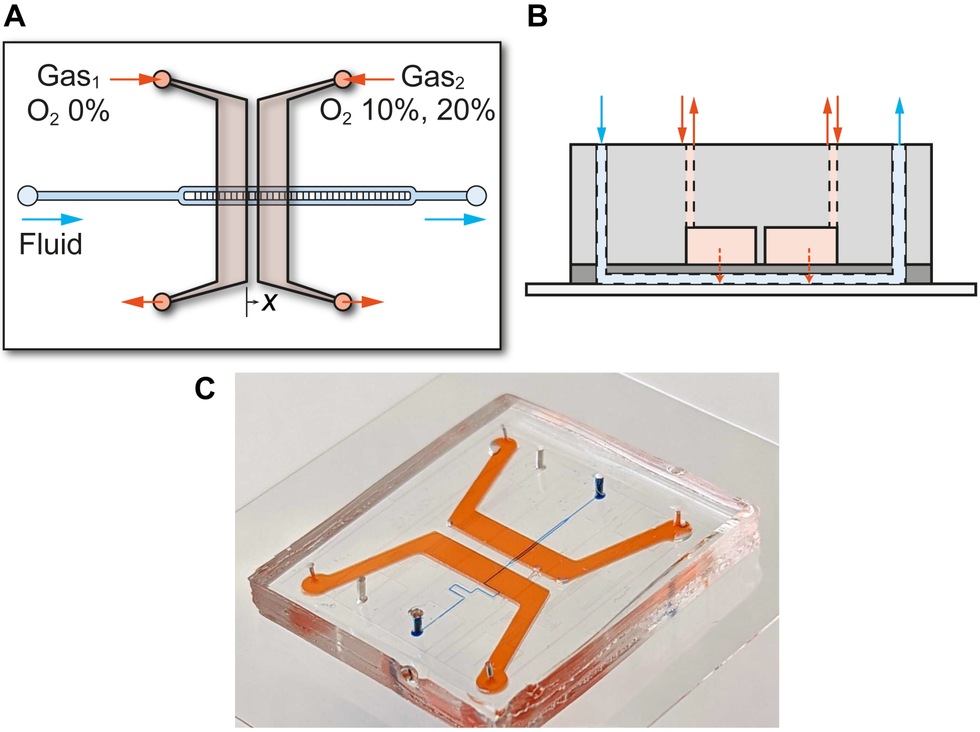

Figure 6.5: Setup for structuring O_2 gradient in the fluid channel with the double-layer chip. **(A)** Schematic describing the experimental setup. **(B)** Cross-sectional illustration of the experimental setup. **(C)** The image of the double-layer chip for creating a gradient along the fluid channel.

can be linearly structured using the double-layer chip with two separate gas channels based on gas diffusion from the top layer to the fluid in the bottom layer.

6.4 Design 3: Double-Layer Chip with Finer Gas Channels for µm-Scale Gradient

6.4.1 Technical Concept

The previous approach is suited for high throughput analysis, yet the O_2 gradient inside a single cultivation chamber (30 to 60 µm in size) is subtle. Thus, the design for the top layer is also microfabricated in the third approach to allow for finer spatial O_2 control, as illustrated in Fig. 6.7. A master mold for the top layer is fabricated with microstruc-

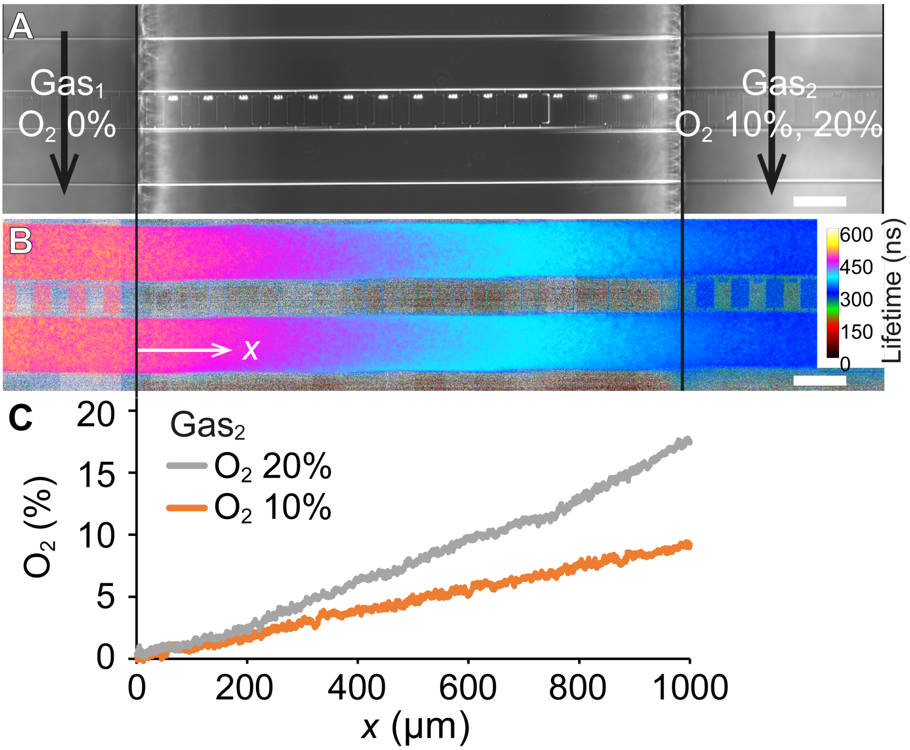

Figure 6.6: O_2 gradient structured in the fluid channel with the double-layer chip. **(A)** The phase-contrast image of the fluid channel in the double-layer chip covered with two separate gas channels with different O_2 concentrations (scale bar 100 µm). **(B)** FLIM image of the O_2 gradient structured along the fluid channel, with O_2 concentration of 20% in the Gas$_2$ (scale bar 100 µm). **(C)** O_2 level along the fluid channel determined from the FLIM measurement.

tures. The top layer has a series of gas channels, and every second channel is connected to a different gas supply. These micro gas channels allow for structuring O_2 gradients at the micro-scale. A potential drawback is that all the parts are fabricated with high air-permeable PDMS, leading to gas diffusion between adjacent gas channels and gas mixing. Also, gas channels cannot overlap each other due to the soft-lithography approach that only allows microstructure fabrication in the same focal plane, limiting the efficiency of gas control and spatial flexibility. For instance, a mono-layer gas channel design in Fig. 6.8A has two main gas channels and branching sub-channels. The branching sub-channels are dead-end since they cannot cross the other main channel. Therefore,

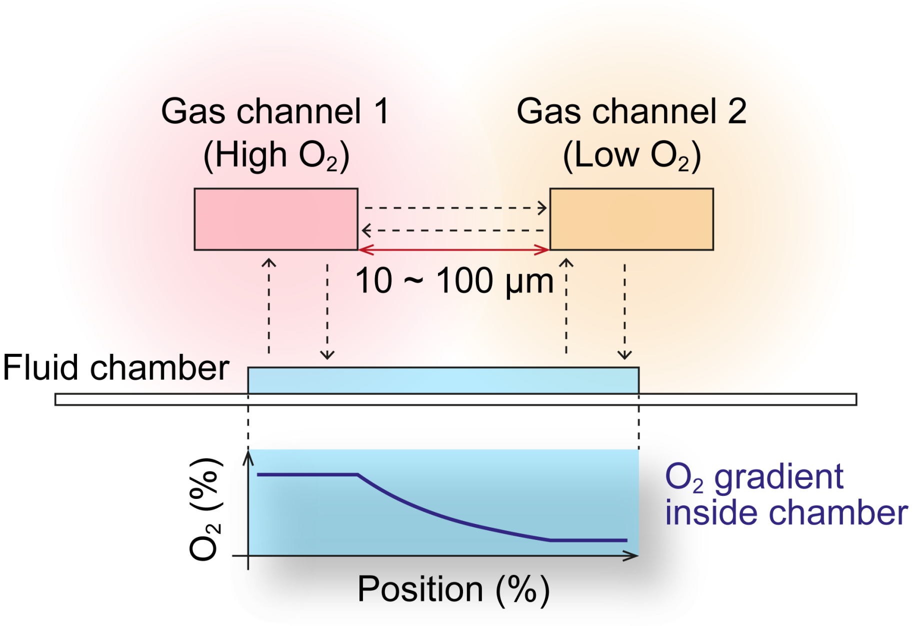

Figure 6.7: Conceptual illustration of spatial O_2 control with finer gas channels in the double-layer chip for recreating µm-scale gradient.

the gas exchange in the branching sub-channels is also based on diffusion. Without the gas flow, the diffusion from surrounding PDMS and adjacent gas channels is expected to play a role, potentially leading to uncontrolled gas mixing.

6.4.2 Materials and Methods

Chip Preparation

For the top and bottom layer, Si-wafers with microstructures were prepared by maskless lithography, where SU-8 photo-resist coated on the wafer were selectively and directly exposed to UV laser (DWL 66+, Heidelberg Instruments, Germany). The design of the wafers was produced by Clewin5, as depicted in Fig. 6.9. The bottom layer consists of a series of cultivation chambers (l 60 × w 60 × h 1 µm, 8 rows × 40 columns) connected to medium supply channels at both sides. The top layer consists of two separate gas channels. The distance (d) and the width (w) were designed to be 100, 50, or 10 µm. The

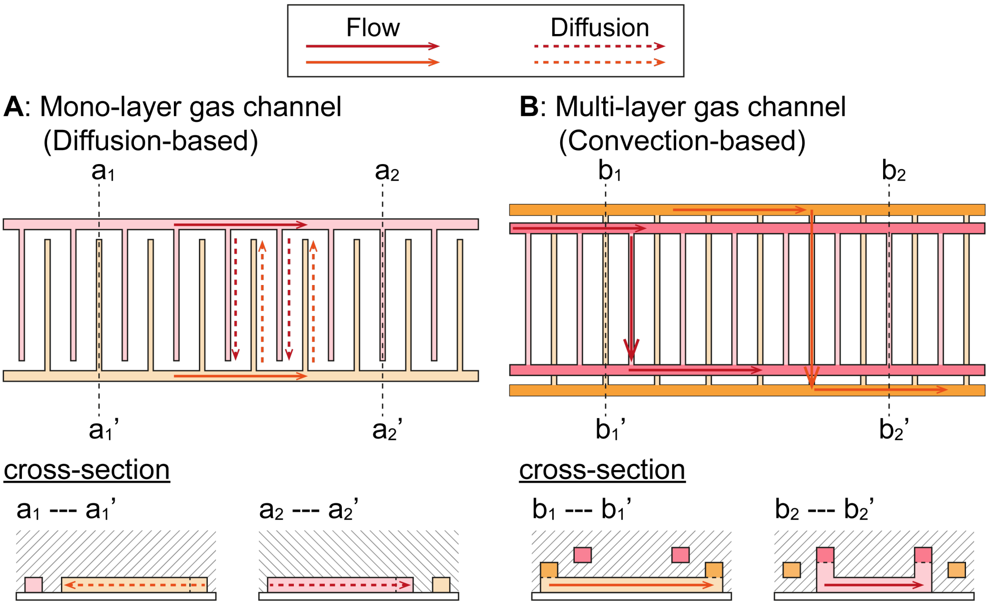

Figure 6.8: Top layer designs of the double-layer chip to recreate µm-scale O_2 gradients. **(A)** Top layer design with mono-layer gas channels, with cross-sections. **(B)** Top layer design with multi-layer gas channels, with cross-sections.

following fabrication procedure was the same as in Chapter 4.2.1.

O_2 Control and Sensing

O_2 was controlled by adjusting the volumetric ratio of O_2 and N_2, with a total of 50 mL/min mass flow rate in each gas channel. Unless otherwise mentioned, FLIM imaging and associated referencing, RTDP calibration, and image analysis were performed as described in Chapter 4. The temperature was set to 37°C. A 100X objective lens (Plan Apo λ Oil, Nikon, Japan) was utilized for O_2 sensing in chambers, with an exposure time of 500 ms to compensate for low signal. Since the RTDP calibration yielded a non-linear Stern-Volmer equation, a calibration curve with negative deviation in Eq. 2.2 was utilized. This yielded $K_q = 9.06$ and $\alpha = 0.58$. RTDP solution of 3 mM was perfused at constant flow rates of 400 nL/min.

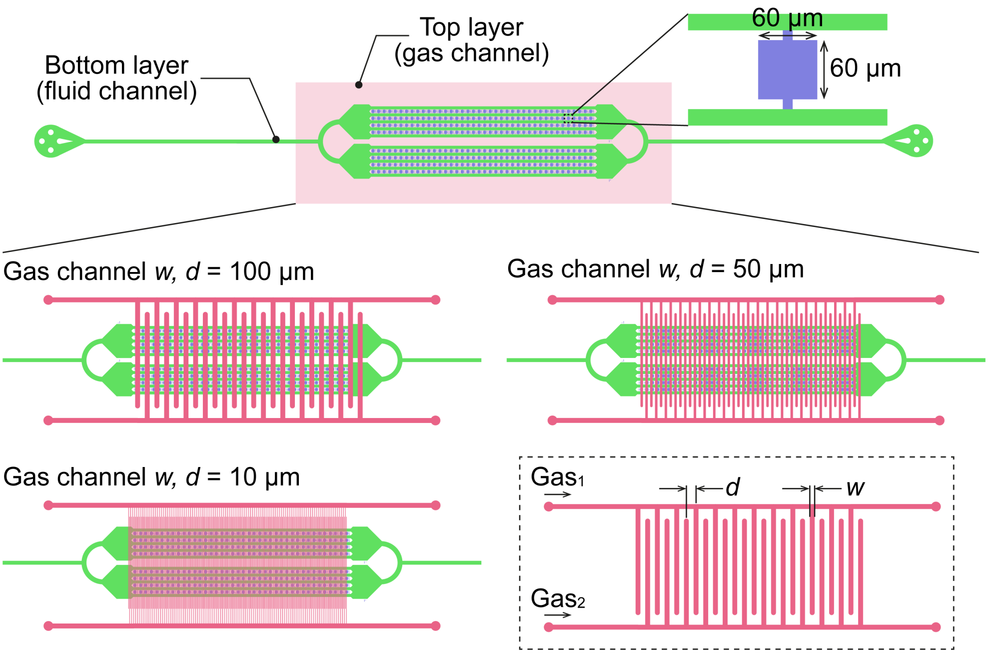

Figure 6.9: Dimension of the top layer with finer channels.

6.4.3 Results

The fabricated double-layer chip with finer gas channels is depicted in Fig. 6.10. Two separated gas channels are colored orange and blue, and the bottom fluid channel is colored light blue for visualization. The chip contains three independent fluid channels covered with top gas channels of different widths and distances (w, d = 100, 50, 10 µm, Fig. 6.10A). An enlarged image of the chip with gas channels of w, d = 10 µm in Fig. 6.10B and a phase contrast image of the gas channels in Fig. 6.10C show the capability to fabricate finer gas channels with soft lithography.

The width of the fabricated gas channels in the double-layer chip was measured and summarized in Fig. 6.11. The measured width was in close agreement with the designed width (shown by a dashed line in the figure), proving the accurate fabrication capability of the gas channels down to the width of 10 µm.

A preliminary O_2 control and sensing experiment was conducted using the fabricated chip. Gas channels with w and d of 100 µm were examined. Randomly selected two

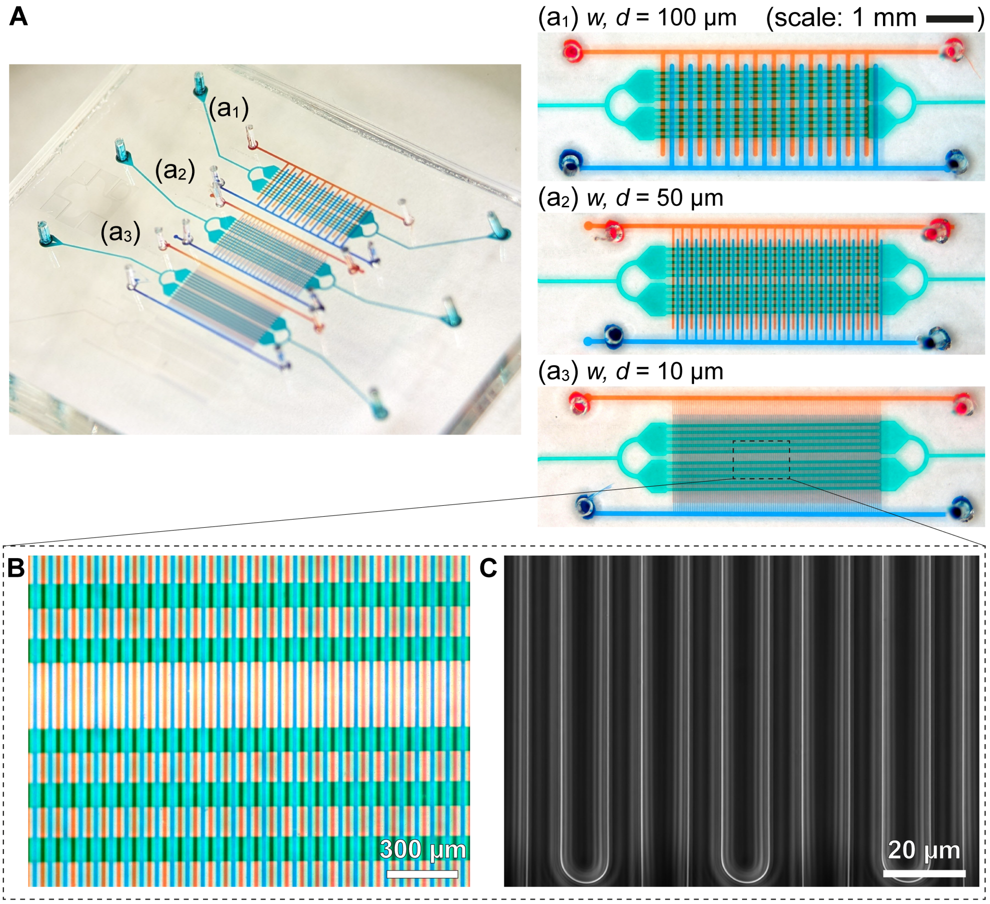

Figure 6.10: Image of the fabricated double-layer chip with finer gas channels. **(A)** Two separated gas channels are colored orange and blue, and the fluid channel at the bottom is colored light blue for visualization. Enlarged images for different widths and distances of gas channels are shown in (a_1) - (a_3). **(B)** Enlarged image of the chip, with gas channels of w, d = 10 µm. **(C)** Phase-contrast image of the chip, with gas channels of w, d = 10 µm.

chambers were observed, and O_2 concentration in the chambers was determined. The position of the first chamber and overlapping gas channels is illustrated in Fig. 6.12A, showing the right side of the chamber covered by a gas channel connected to the gas source without O_2. The O_2 concentration was measured in the chamber, resulting in a pseudo-color image of fluorescence lifetime in the chamber as depicted in Fig. 6.12B. The O_2 concentration in the chamber was determined from the lifetime using the non-linear

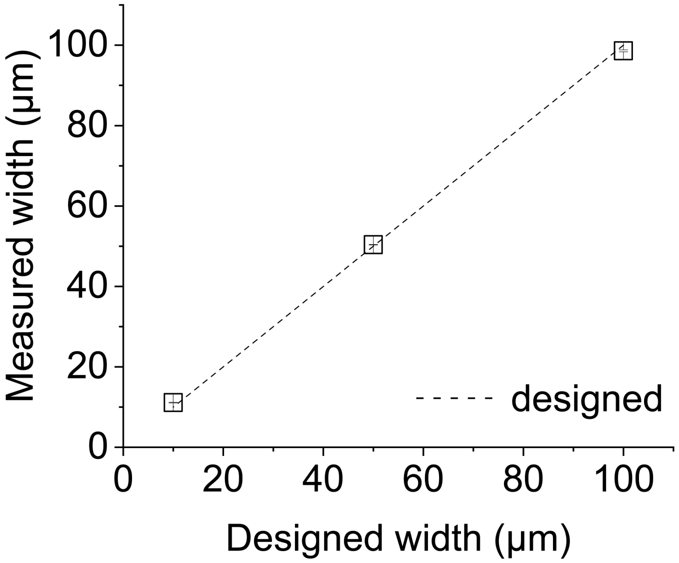

Figure 6.11: Measured channel width of the fabricated double-layer chip with fine structures. The dashed line depicts a desired width, where the measured width equals the designed width. Data are expressed as mean ± S.D (*n* = 3 measurements from different positions).

Stern-Volmer calibration curve and summarized in Fig. 6.12C. Note that the hatched areas in Fig. 6.12C were not considered due to disturbed FLIM imaging near the chamber walls (5 µm from each side of the chamber wall). The determined O_2 profile shows a gradual gradient in the chamber, starting with 9.0% O_2 at the left and ending with 6.2% O_2 at the right of the chamber.

The O_2 concentration in the second chamber was also determined following the same procedure. The position of the second chamber and overlapping gas channels is illustrated in Fig. 6.13A, showing the left side of the chamber covered by a gas channel connected to the gas source with 21% O_2. The O_2 concentration was measured in the chamber, resulting in a pseudo-color image of fluorescence lifetime as depicted in Fig. 6.13B. The O_2 concentration in the chamber was determined from the lifetime using the non-linear Stern-Volmer calibration curve and summarized in Fig. 6.13C. As is the same with the first chamber, the areas marked with diagonal lines in Fig. 6.13C were not considered due to disturbed FLIM imaging near the chamber walls (5 µm from each side of the

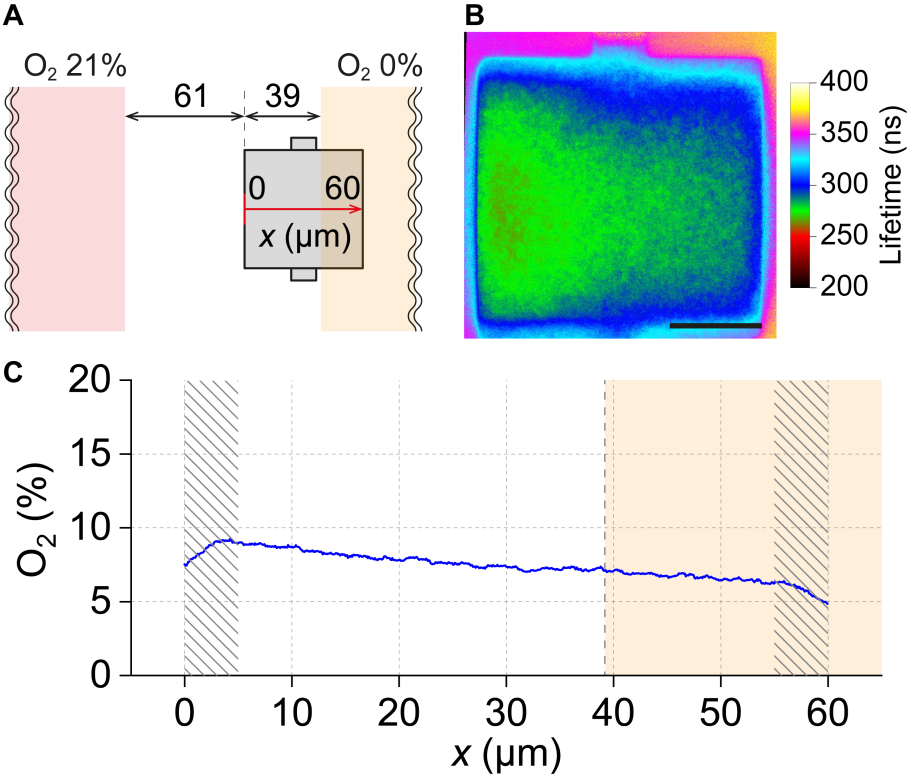

Figure 6.12: O_2 measurement with FLIM in the double-layer chip with finer gas channels (chamber 1). **(A)** Schematic illustrating the position of the measured chamber and surrounding gas channels. **(B)** FLIM image of the chamber filed with RTDP (scale bar 20 μm). **(C)** Determined O_2 level in the chamber. The hatched areas were not considered due to disturbed FLIM imaging near the chamber walls.

chamber wall). The determined O_2 profile in the second chamber shows a more homogeneous O_2 distribution in the chamber, starting with 16.9% O_2 at the right of the chamber and ending with 17.7% O_2.

These O_2 measurement results from two selected chambers imply the capability to recreate μm-scale O_2 gradient inside the chamber depending on the position of the chamber and overlapping gas channels, as well as the O_2 availability in the gas source. However, uncontrolled gas diffusion exists between adjacent gas channels and surrounding PDMS, making it complicated for the system to control the range of O_2 concentration to a desired range. A system that prohibits such an uncontrolled gas diffusion would be

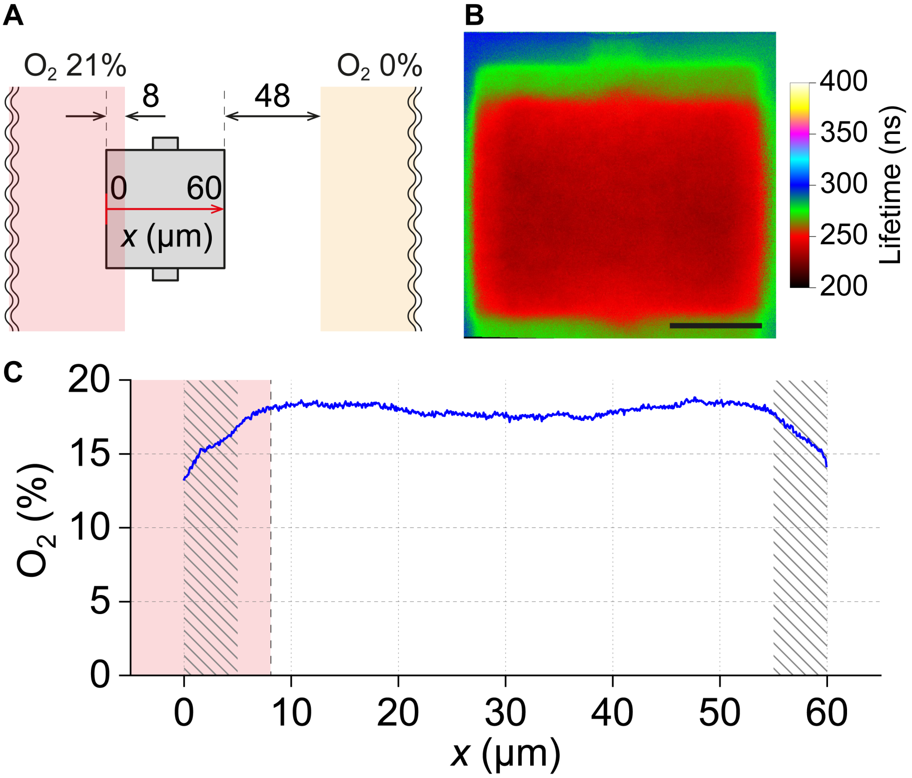

Figure 6.13: O_2 measurement with FLIM in the double-layer chip with finer gas channels (chamber 2). **(A)** Schematic illustrating the position of the measured chamber and surrounding gas channels. **(B)** FLIM image of the chamber filed with RTDP (scale bar 20 µm). **(C)** Determined O_2 level in the chamber. The hatched areas were not considered due to disturbed FLIM imaging near the chamber walls.

required for a better O_2 control at the scale of µm.

6.5 Design 4: Double-Layer Chip with Glass-Made Top Layer

6.5.1 Technical Concept

To eliminate the uncontrolled gas diffusion between adjacent gas channels, as mentioned in the previous section, a top layer is fabricated by glass microfabrication and used for gas supply (Fig. 6.14). The glass-made top layer restricts the gas diffusion between gas

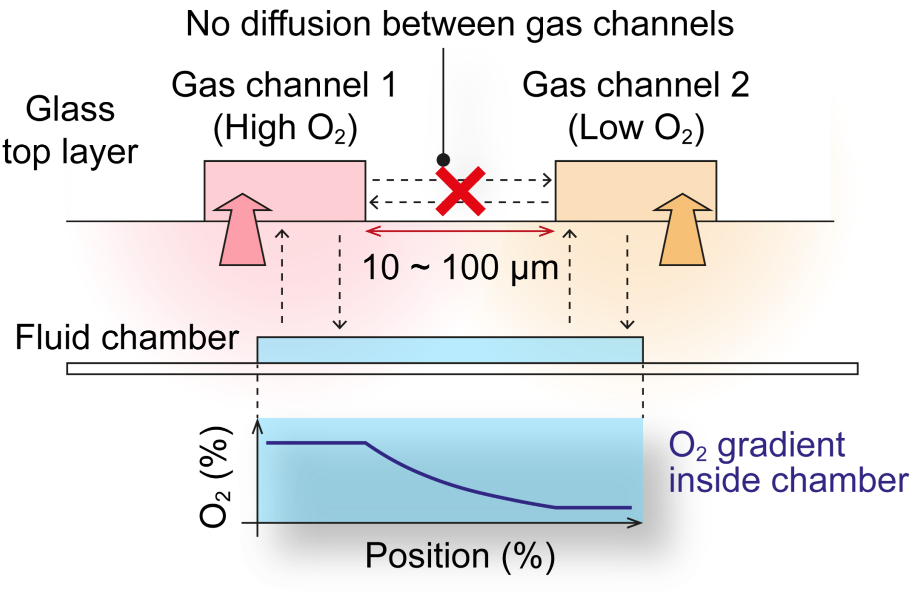

Figure 6.14: Conceptual illustration of spatial O_2 control with a glass-made top layer in the double-layer chip.

channels, enabling more precise gas control at the micro-scale when compared to high air-permeable PDMS. The glass top layer is fabricated by selective laser-induced etching (SLE), where glass is selectively modified by focusing femtosecond laser radiation and wet-chemical etching [148–151]. The SLE technique also enables the manufacturing of multi-layer channels thanks to its multiphoton process. This feature is advantageous over conventional photo-lithography-based microfabrication that limits structures only on the same focal plane as illustrated in Fig. 6.8A as the mono-layer gas channel. With SLE, multi-layer gas channels overlapping each other can be designed, allowing more flexibility in channel designs. An example design is shown in Fig. 6.8B, where both sides of the sub-channels are connected to the main channels. This configuration allows gas flow through sub-channels and always provides fresh gas with desired O_2 concentration, minimizing the uncontrolled disruption in O_2 concentration due to gas diffusion. The gas diffusion between adjacent gas channels is also restricted as the top layer is made of glass. This chip concept with the glass-made top layer would provide more precise spatial O_2 control at the μm-scale compared to PDMS-based chips.

Note that the double-layer chip with the glass-made top layer rather serves as an outlook toward better spatial O_2 control at µm-scale. Therefore, this section explains the conceptualization and fabrication of the device.

6.5.2 Materials and Methods

Chip Preparation

The same master mold as in Chapter 4.2.1 was utilized for the bottom layer. The glass top layer was fabricated by SLE; a glass bulk (l 22 × w 18 × h 5 mm) was first selectively irradiated and modified by a laser via a multiphoton absorption process (LightFab 3D Printer, LightFab, Germany). This is followed by wet chemical etching with KOH, subtracting the selectively modified glass volume, and resulting in 3D channels in the glass substrate. The glass top layer was designed with Solidworks CAD software, as depicted in Fig. 6.15. The top layer comprises two separate gas channels (A and B). Both sides of the middle subchannels are connected to the main channels, enabling gas flow through subchannels. This is possible because the main channel B crosses over the subchannels A. Two through holes C were also designed for fluid supplies. Detailed dimensions of the top layer (shown as (I) and (II) in Fig. 6.15) are depicted in Fig. 6.16. Various channel widths (w) between 100 µm and 2 µm were prepared; for channels with w = 100, 50, and 25 µm, the width and the distance between channels were set the same (DETAIL (I) in Fig. 6.16). The distance between channels was 50 µm for channels with smaller widths, w = 10, 5, and 2 µm (DETAIL (II) in Fig. 6.16).

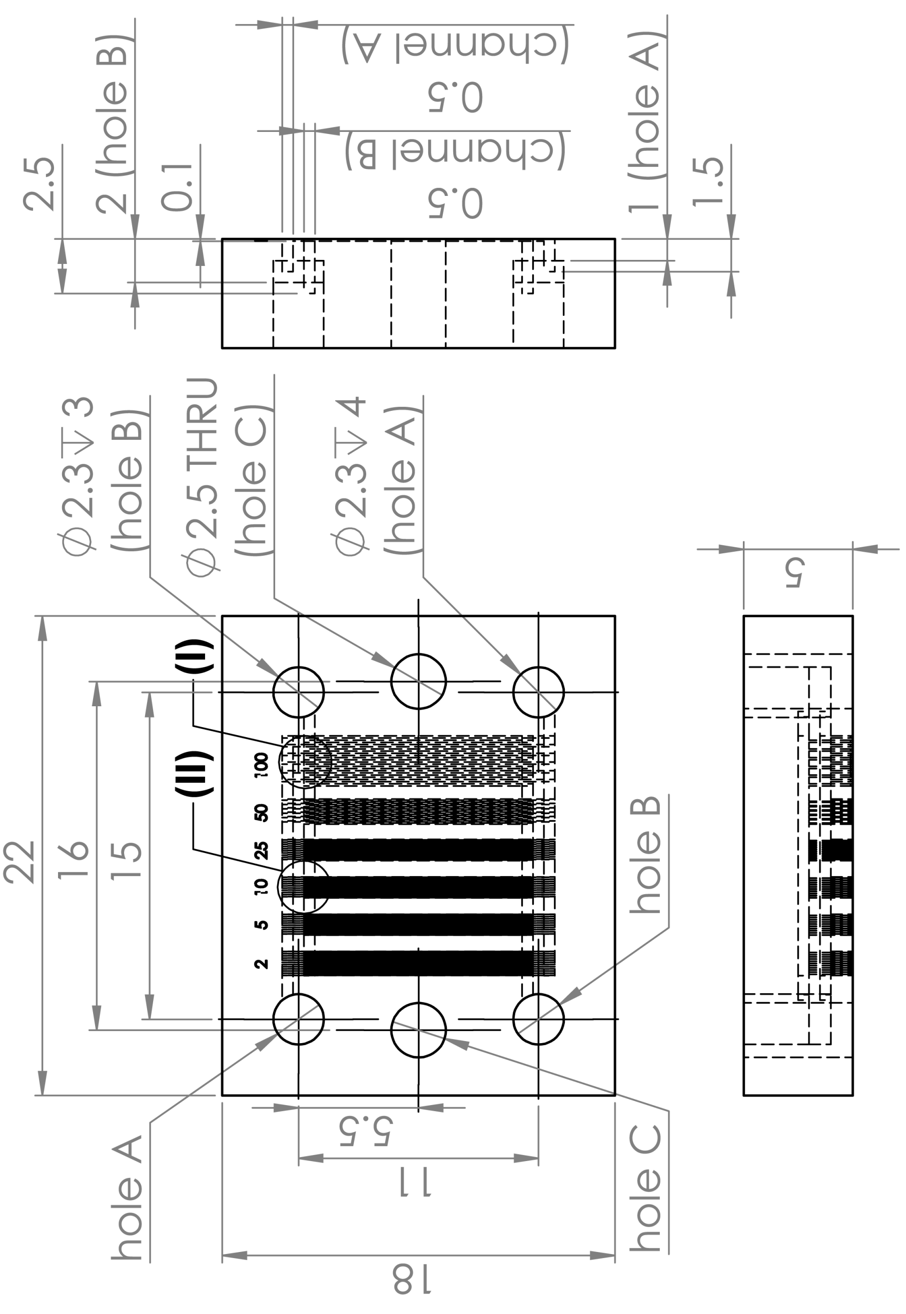

Figure 6.15: Dimension of the glass-made top layer. Detailed views (I and II) are provided in Fig. 6.16 (in mm).

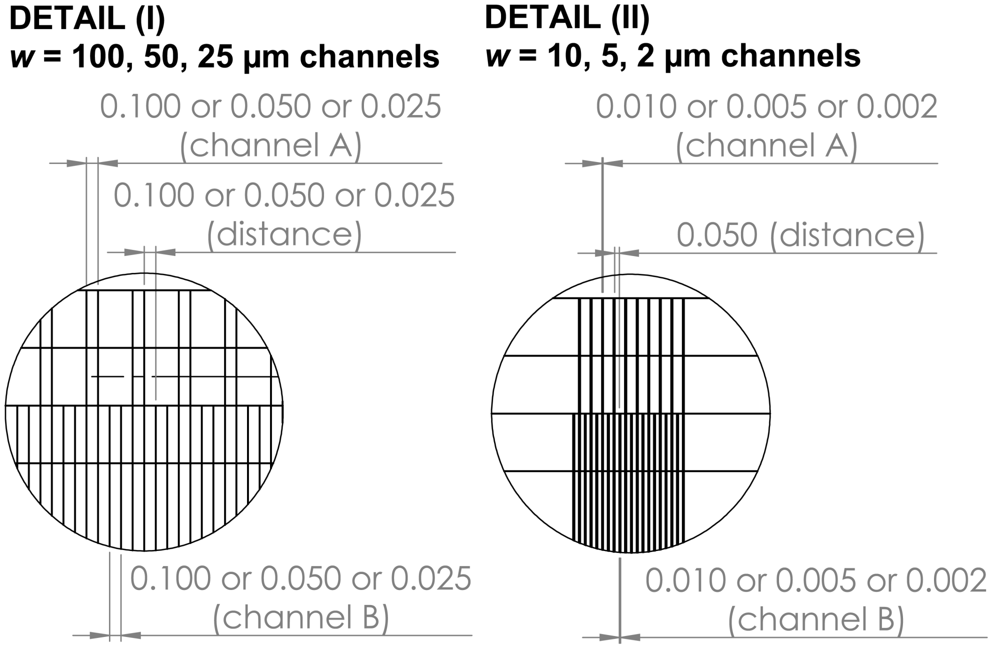

Figure 6.16: Detailed dimension of the glass-made top layer described in Fig. 6.15 (in mm).

The fabrication procedure of the double-layer chip with the glass top layer is illustrated in Fig. 6.17. The process is divided into (i) PDMS membrane preparation and (ii) assembly. First, PDMS was spin-coated onto the Si-wafer mold with microstructures of fluid channels. After heating at 80°C for 1 h, the cured PDMS membrane was carefully peeled from the mold. The PDMS membrane was then placed onto a slide glass covered with Parafilm. Parafilm was added as an intermediate layer to ease the process of chip peeling later on. Isopropyl alcohol (IPA) was used to place the PDMS membrane without wrinkles. The PDMS membrane was finally prepared by drying the remaining IPA at room temperature (RT).

Then, the glass-made top layer and the prepared PDMS membrane were plasma-bonded. This bonding treatment gives an irreversible attachment of two parts. The chip was peeled off, then uncured PDMS was filled into the holes for fluid supply (hole C in Fig. 6.15). The added PDMS was cured at 80°C for 2 h. Holes with ϕ = 0.75 mm were punched to prepare fluid inlet and outlet at the cured PDMS in hole C and bonded to a glass substrate.

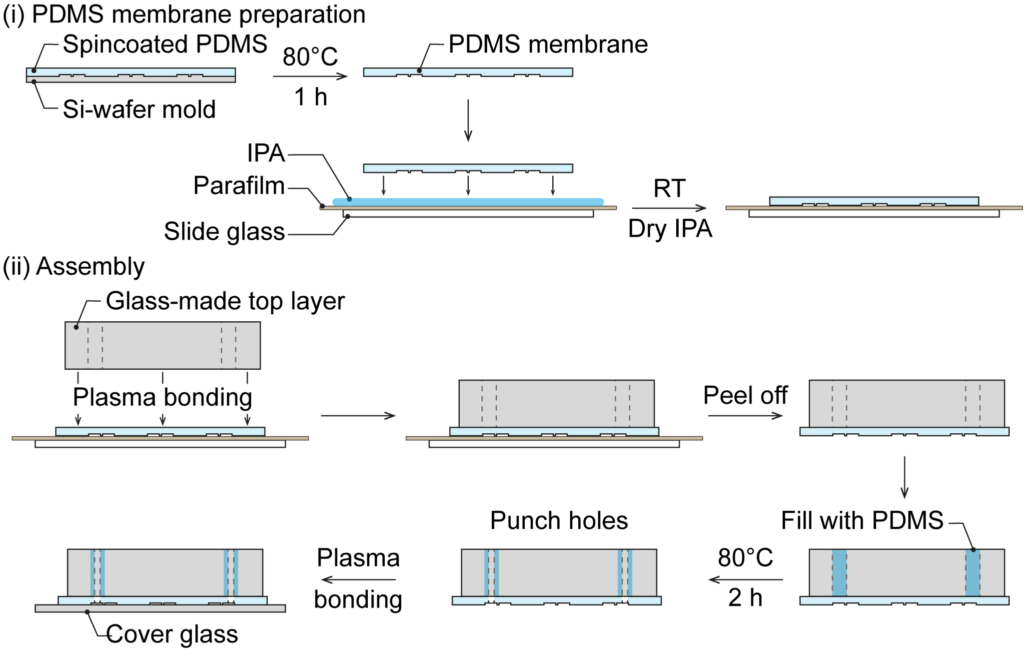

Figure 6.17: Fabrication procedure of the double-layer chip with glass top layer.

6.5.3 Results

The fabricated double-layer chip with the glass top layer is depicted in Fig. 6.18. The entire chip image in Fig. 6.18A successfully assembles two different materials, the glass-made top layer and the PDMS-made bottom layer. The enlarged image of the glass top layer in Fig. 6.18B depicts two separated and multi-layer gas channels. Both sides of the sub-channels are connected to the main channels, allowing gas flow through sub-channels. This is a huge advantage over PDMS-made mono-layer gas channels, where only one side of the sub-channels is connected to the main channels, and gas exchange in the sub-channels is only performed by diffusion.

The gas sub-channels fabricated in the glass top layer were observed by phase-contrast microscopy to evaluate the fabrication accuracy. Phase-contrast images of the gas sub-channels are summarized in Fig. 6.19. The images were taken at the top and the bottom of the channels since it was revealed during the observation that the fabricated channels were taper-shaped. Microscopy observation showed that the channel width at the top was narrower than at the bottom, featuring a tapered shape for all the different

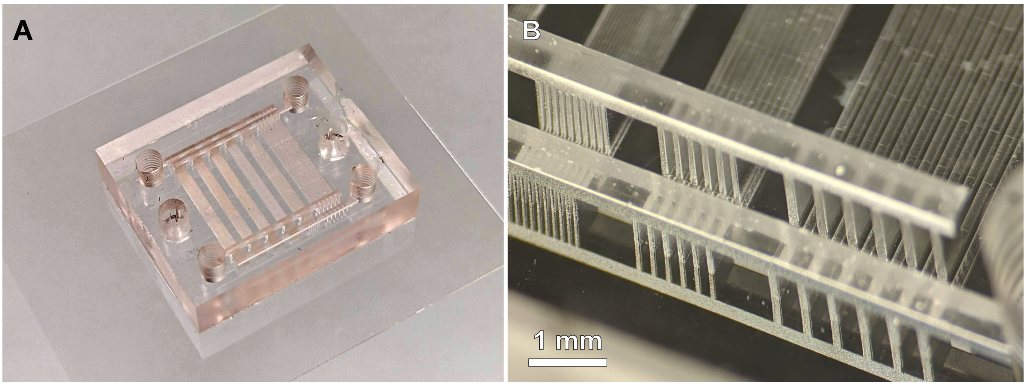

Figure 6.18: Image of the fabricated double-layer chip with the glass top layer. **(A)** The image of the entire chip. **(B)** Enlarged image of the gas channels in the glass top layer.

designed widths.

The channel width at the top and bottom of the channels was measured from the phase-contrast images and summarized in Fig. 6.20. The graph on the left shows all the measured width against the primarily designed width, and the area marked with a gray rectangle is supplemented with an enlarged graph on the right. The measurement results show that the measured width was wider than the designed width at any measured channels. The channel width at the top was always narrower than at the bottom, representing a taper-shaped channel. This tapered shape of the channels was probably caused by wet chemical etching with KOH after selective laser irradiation, which is typical for such a fabrication process. The SLE process should be optimized further, for instance, by adjusting the duration of wet etching and concentration of KOH solution to achieve more precise fabrication of gas channels on glass. Nevertheless, it was confirmed that the fabrication of the double-layer chip with the glass-made top layer was durable, and it is expected to be utilized for finer spatial O_2 control.

6.6 Discussion

Four different chip designs were examined to enable spatial O_2 control, and various insights were gained through the development process. The first design with side gas channels successfully recreated the O_2 gradient perpendicular to fluid flow within the fluid channel. This preliminary result demonstrates the ability to control O_2 via diffusion

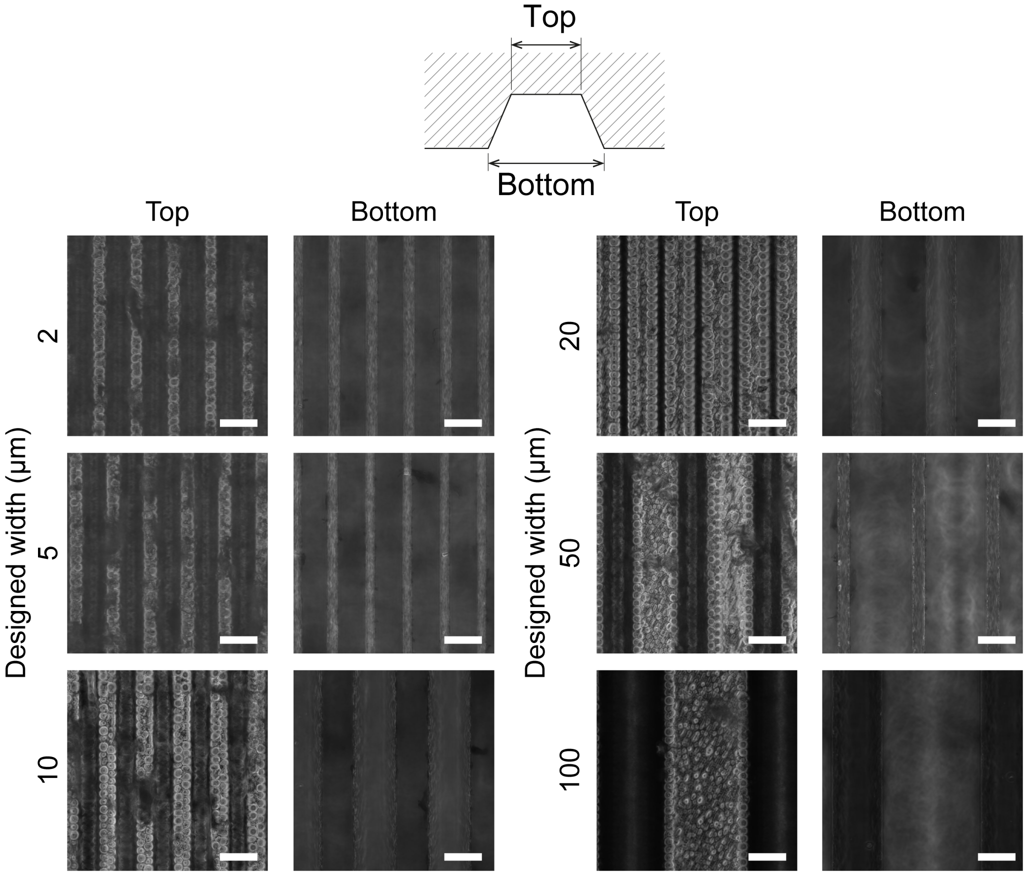

Figure 6.19: Phase-contrast images of the fabricated channels in the glass-made top layer. The images were taken at the top and bottom of the channels (scale bar 50 µm).

through PDMS walls. However, this design also experienced significant deviations in O_2 concentration from the intended conditions (the O_2 gradient was structured between 12% and 18%, while the side gas channels were supplied with gas containing 10% and 0% O_2). This was primarily due to air diffusion from the surrounding PDMS and the low diffusion efficiency resulting from the small surface area available for gas exchange between the gas and fluid channels.

The outcome from the side gas channel informed the subsequent design of a double-layer chip structure. This double-layer chip, with larger gas channels, was initially prepared to evaluate gas exchange efficiency between the top gas channels and bottom fluid

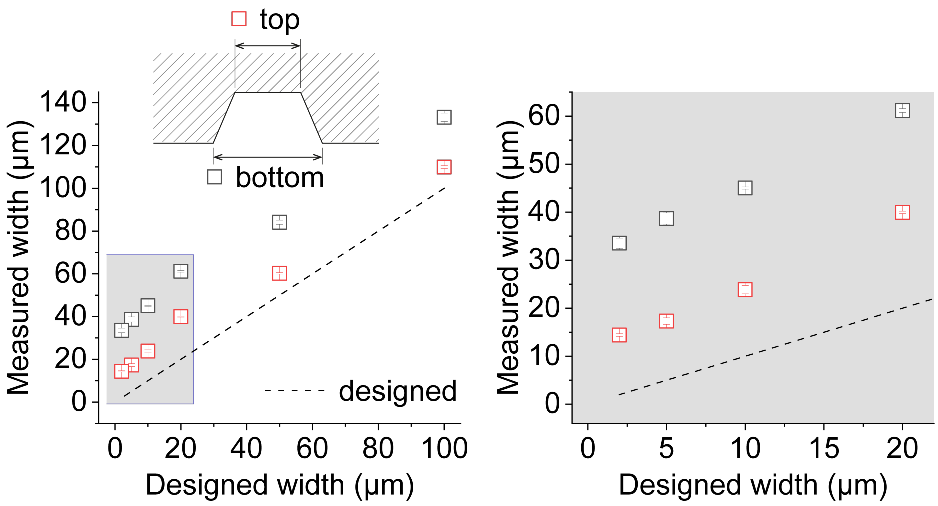

Figure 6.20: Measured channel width of the glass-made top layer. Channel width was measured at the top and bottom of the channels. The dashed line depicts a desired width, where the measured width equals the designed width. The area marked with a gray rectangle (left) is supplemented with an enlarged graph (right). Data are expressed as mean ± S.D (*n* = 3 measurements from different positions).

channels through a thin intermediate PDMS membrane. Additionally, this chip design aimed to control O_2 concentration in a gradient across a series of cultivation chambers for high-throughput analysis. The result showed a successful O_2 gradient recreation parallel to the fluid flow, with precise O_2 control compared to the applied conditions.

The next aim was to use the double-layer chip structure to recreate the O_2 gradient at a smaller scale inside chambers in the range of µm. To achieve this, the top layer was also microstructured by soft lithography. The results implied the capability to recreate the O_2 gradient at the µm-scale inside the chamber depending on the position of the chamber and overlapping gas channels. However, this chip design with finer gas channels suffered greatly from uncontrolled gas diffusion between adjacent gas channels and surroundings.

The results from these two double-layer chip designs with large and fine gas channels imply that the gas channel width and flow matter for precise O_2 control. These two aspects allow for alleviating the O_2 concentration disturbance caused by diffusion from the surroundings. While keeping the gas channel width narrow would be indispensable for recreating µm-scale O_2, the flow in the gas channels should be implemented into the

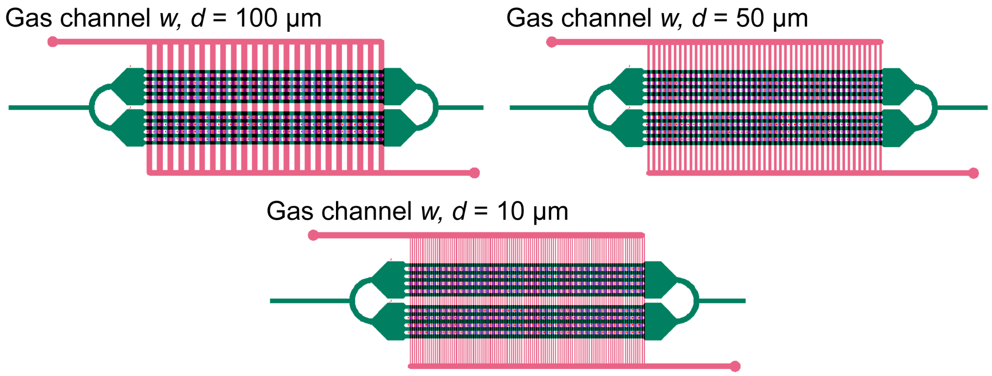

Figure 6.21: Recommended designs of finer gas channels in the top layer when combined with the mini-incubator.

system to provide a fresh gas source with controlled O_2 concentrations.

Therefore, the fourth design, the double-layer chip with the glass-made top layer, was introduced. The fabrication of the glass top layer with the SLE technique allowed the fabrication of the multi-layer gas channels, which was not feasible with the conventional microfabrication process based on soft lithography. The top and bottom layers made of different materials (glass and PDMS) were successfully assembled into a single chip. The SLE fabrication procedure has room for optimization for more accurate channel fabrication. The double-layer chip with the glass top layer is expected to solve issues regarding uncontrolled gas diffusion in PDMS-based chips and finally achieve spatial O_2 control at the µm scale.

Although the third design with fine gas channels resulted in low capability in O_2 control, a few more setups are worthwhile examining with the same chip design. A recommendation is to use the double-layer chip in combination with the mini-incubator described in Chapter 3. In this setup, O_2-limited gas should be supplied either in the mini-incubator or gas channels in the chip, and O_2-containing gas should be provided to the other. This setup might offer better control over spatial O_2 distribution at an aimed range without disturbance from ambient air. The gas channel design does not have to be separated into two channels in such a setup. As depicted in Fig. 6.21, only a gas channel might be necessary, which allows gas flow through sub-gas channels and fresh gas supply.

Further consideration is necessary regarding reusing the double-layer chip with the glass-made top layer. Unlike the soft-lithography approach, which allows multiple chip fabrication from a single PDMS molding, glass-made top layers are fabricated one by one with SLE, limiting the number of chips that can be fabricated. Moreover, the glass-made top layer and the PDMS bottom layer are irreversibly bonded by plasma treatment, so the top layer cannot be easily separated and reused for the next chip assembly. Establishing a procedure for thoroughly washing and cleaning the chip would be a straightforward solution. With such improvements in characterization, fabrication, and operation, the proposed double-layer chip with the glass-made top layer would be more influential.

Furthermore, O_2 measurement using FLIM in a µm-range chamber also requires improvement. As shown in Fig. 6.12B and 6.13B, the lifetime measurement was disturbed at the edge of the chamber. Several factors could contribute to this issue, such as optical distortions and reflections near the PDMS walls, fluorophore adsorption to PDMS, scattering, and autofluorescence from PDMS. Some of these factors might be less significant if additional treatment is used, such as passivating PDMS with coatings such as bovine serum albumin (BSA) or polyethylene glycol (PEG). More investigation is necessary to achieve precise O_2 measurement in a µm-scale environment in microfluidics.

7 Conclusions and Outlook

7.1 Conclusions

Microbial single-cell analysis in microfluidics is a promising approach to investigate microbial growth behavior in greater detail under precisely defined environments. Yet little effort has been made to implement spatiotemporal O_2 control for microbial single-cell analysis, an essential factor determining microbial growth and physiology. In this thesis, various approaches were examined to achieve (1) a straightforward O_2 control platform, (2) temporal O_2 control in the range of seconds to minutes, and (3) spatial O_2 control in the range of µm.

In the first attempt, a comprehensive experimental platform was developed that is easily transferable to microbial single-cell analysis within various formats of microfluidic devices (Chapter 3). By utilizing a low-cost 3D-printed mini-incubator surrounding the air-permeable PDMS microfluidic chip, the O_2 concentration in the microfluidic chip was successfully controlled straightforwardly. The O_2 sensing method with FLIM and the O_2-sensitive dye was also implemented, allowing direct measurement of O_2 availability inside fluid channels. The following imaging with time-lapse microscopy and deep-learning-assisted image analysis provided a solid platform for data analysis. The presented system offers a method easily transferable by various researchers, for instance, microbiologists interested in investigating microbial single-cell behavior under precisely controlled O_2 environments. Yet, this platform was limited by the incapability to recreate spatiotemporal O_2 environments often observed in natural microbial habitats.

To solve the limitations, double-layer microfluidic chips are developed with various designs. The first design primarily tackled the limitation in temporal O_2 control (Chapter 4). The newly developed microfluidic platform allowed recreating O_2 oscillations occurring within seconds to minutes, enabling temporally resolved microbial growth analysis at single-cell resolution. The case studies were performed, where aerobic and anaerobic growth and adaptation of *E. coli* (Chapter 4) and *C. glutamicum* (Chapter 5) were investigated. The growth analysis results of these microbes revealed aerobic/anaerobic specific growth and growth adaptation in response to O_2 oscillations, insights that cannot be gained through conventional cultivation setups.

The following device development aimed to achieve spatial O_2 control in microbial single-cell analysis using microfluidics (Chapter 6). Four different designs, (i) side gas channels, (ii) double-layer chip with large gas channels, (iii) double-layer chip with finer gas channels, and (iv) double-layer chip with the glass-made top layer, were examined to recreate O_2 gradient at a large scale (in mm) for high-throughput, and at a smaller scale (in µm) for fine spatial O_2 control. The experiment results showed the capability of spatial O_2 control by diffusion. The designs with finer gas channels suffered from uncontrolled gas diffusion effects from surrounding environments. Therefore, the double-layer chip with the glass-made top layer was introduced, and the device prototype was successfully developed.

In summary, three key aspects of this thesis were tackled throughout the thesis. The first (Straightforward O_2 control platform) and the second aspects (temporal O_2 control in the range of seconds to minutes) were investigated thoroughly. In contrast, the third aspect (spatial O_2 control in the range of µm) was examined with preliminary experiments and recommendations for further improvement. The thesis promoted the development of microfluidic devices for microbial single-cell analysis under controlled O_2 and paves the way toward recreating spatiotemporally controlled O_2 microenvironments.

7.2 Outlook

7.2.1 Technical Aspects

The demonstrated experiment and analysis platform can be further enhanced through additional improvements. The first aspect concerns the calibration procedure of the O_2-sensitive dye, RTDP. The O_2 measurement using FLIM and the O_2-sensitive dye requires a two-point calibration at known O_2 levels. This calibration was performed by flushing synthetic air containing either 0% or 21% O_2. While controlling 21% O_2 availability was reliable, achieving strict control at 0% O_2 posed challenges due to potential disturbances from high air permeability and residual air within the PDMS. Enhancing the calibration method to ensure precise 0% O_2 availability, such as incorporating chemical O_2 scavengers that are compatible with the O_2-sensitive dye [91, 92, 132], could enable more accurate on-chip O_2 control under anaerobic conditions.

Another aspect to be dealt with is characterizing the double-layer chip with the glass-made top layer. The gas channel chip design and the SLE fabrication process should be optimized to achieve µm-scale O_2 gradient recreation. The chip is to be characterized using FLIM and the O_2 sensitive dye. This designing, characterization, and optimization process is to be performed iteratively.

7.2.2 Biological Aspects

The microbial cultivation experiments in the thesis primarily served as proof of principles for demonstrating developed microfluidic experimental platforms. These results, however, also raised various biological questions and further cultivation outlooks.

Does *E. coli* exhibit a higher growth rate immediately after a switch from anaerobic to aerobic conditions? Is this growth advantage consistent across biological replicates or potentially different strains? How long does this growth advantage persist, and does it depend on the oscillation period or O_2 level? Is the recovery time after the overshoot from anaerobic to aerobic conditions comparable to the recovery time after the undershoot after a switch from aerobic to anaerobic conditions? Compared to the other oscillations/static conditions, is the overall yield larger under constant switching between aerobic and anaerobic? Does the growth adaptation (recovery time, overshoot, undershoot) change if a mutant strain lacking O_2 sensing capability (for example *E. coli* Δfnr) is cultivated under oscillating O_2 conditions and to what degree? Can a strict anaerobic microorganism be cultivated and investigated using the same microfluidic platform? Can a microbial community be spatiotemporally structured inside spatiotemporally controlled O_2 microenvironments?

Furthermore, implementing tracking analysis would bring more insight into the acquired data and be critical to answering some of the biological questions mentioned above (Fig. 7.1). Most of the data was currently investigated at the colony level, limiting the single-cell perspectives. Tracking analysis enables the investigation at the single-cell level, leveraging the advantage of the developed microfluidic platform to observe microbial growth at the single-cell resolution.

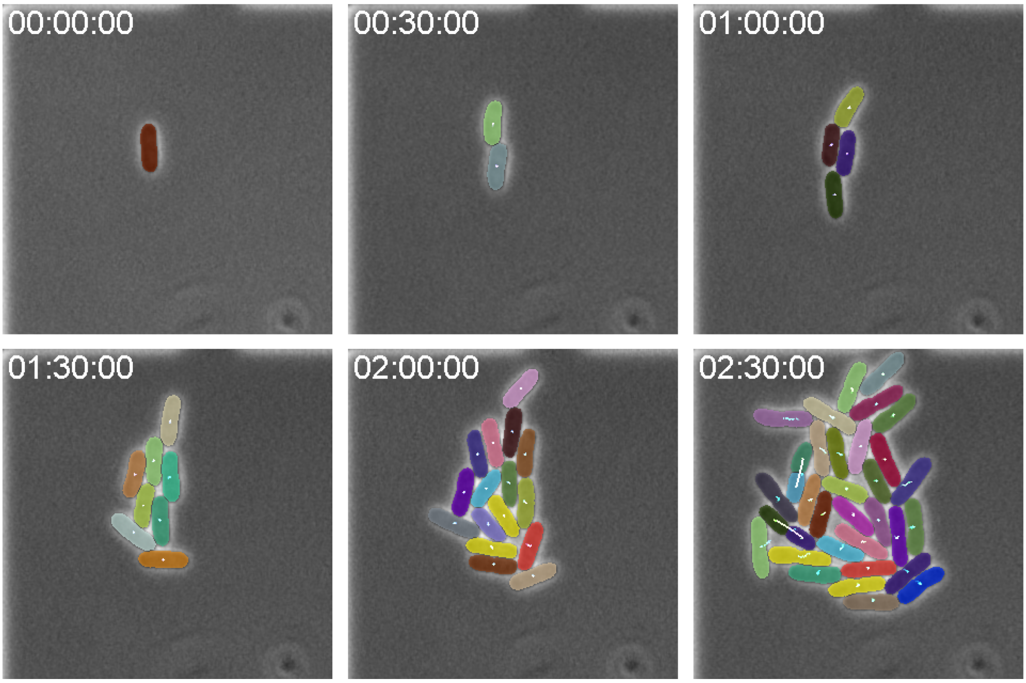

Figure 7.1: Example of cell tracking analysis. Different colors visualize the segmented cells. A white dot represents the center of mass, and cell division is represented by a white line connecting two cells.

Acknowledgements

This doctoral research was conducted at Forschungszentrum Jülich between February 2022 and June 2025. I must say that completing this journey was impossible without the help of many people.

First, I would like to thank the head of the Microscale Bioengineering Group, Dr. Dietrich Kohleyer, who supervised my Ph.D. research. I first contacted Dietrich in 2019 while looking for a half-year internship. Dietrich graciously welcomed me and continued to host me as a Ph.D. student later on. He has been a great mentor with whom I can openly discuss research progress, my future career, and more. Dietrich also helped me settle in Germany and quickly adapt to a different culture.

The next thank you goes to Prof. Dr. Wolfgang Wiechert for hosting me at the Institute of Bio- and Geosciences 1 (IBG-1) and being my Doktorvater. Wolfgang helped me a lot with the university admission process. I would also like to thank Prof. Dr. Jørgen Magnus for letting me give a talk at BioVT and for a great discussion as my second reviewer. I would like to express my gratitude to Prof. Marek Behr, Ph.D., for serving as the chairman of the doctoral defense committee.

The research involved extensive image analysis, and I would like to thank Dr. Katharina Nöh, Johannes Seiffarth, and Karina Ruzaeva for their help in providing the image analysis platform. In addition to image analysis, I always enjoyed spontaneous discussions with Katharina and Johannes in the hallway. From the same building, Prof. Dr. Eric von Lieres and Birgit Stute worked with me on the simulation, for which I am grateful. I would also like to thank Prof. Dr. Thomas Drepper from the Institute of Molecular Enzyme Technology (IMET) for always having positive and cordial discussions and reviews.

I sincerely appreciate all the Microscalers who made my life at FZJ colorful and memorable. First, Agnes Müller-Schröer helped me at every opportunity, making my research run smoothly. Lennart Witting, Matthias Pesch, and Michelle Bund were always with me at the research center. Your hard work made me think I should keep up with you. I enjoyed our seasonal events, lunches, big and small chats, and the daily walk to the Seecasino. I would also like to thank Markus Leygeber for his support in starting my research and life in Germany, and Matthias Rieb and Bastian Wollenhaupt for being good senior Ph.D. students and giving me lots of tips at IBG-1. Furthermore, I thank Flavio Kunert, Nina Dolfen, Arne Kayserling, and Aurian Andree for the comfortable time at the office.

I would also like to thank the people from the manufacturing workshop and the infrastructure, especially Daniel Klein, Erik Kranz, and Horst Kiel, for their help in setting up experimental and surrounding setups. I would also like to thank Nadja Glöck from the Helmholtz Nano Facility for excellently doing the microfabrication.

I want to thank the Japan Student Services Organization (JASSO, Japan) for providing me with a scholarship for my research stay in Germany, the Chemical and Biological Microsystems Society (CBMS, US), and the Company of Biologists (UK) for generously funding my attendance at the µTAS 2024 international conference as part of my Ph.D. research.

Finally, I would like to thank my parents and Nana in Japan for always encouraging me. Without their support, I would not have been able to complete this exciting but sometimes challenging journey.

I cannot mention all the people, but I would like to express my appreciation to all of them. With all my great memories and experiences in Jülich, I am excited to move on to the next chapter of my life.

June 2025
Keitaro Kasahara

Bibliography

1. Lalejini, A., Ferguson, A. J., Grant, N. A. & Ofria, C. Adaptive phenotypic plasticity stabilizes evolution in fluctuating environments. *Front. Ecol. Evol.* **9** (2021).
2. Fusi, M., Rigaud, S., Guadagnin, G., Barausse, A., Marasco, R., Daffonchio, D., Régis, J., Huchet, L., Camin, C., Pettit, L., Vina-Herbon, C. & Giomi, F. Ideas and perspectives: The fluctuating nature of oxygen shapes the ecology of aquatic habitats and their biogeochemical cycles – the aquatic oxyscape. *Biogeosciences* **20,** 3509–3521 (2023).
3. Stocker, R. Marine microbes see a sea of gradients. *Science* **338,** 628–633 (2012).
4. Dedrick, S., Akbari, M. J., Dyckman, S. K., Zhao, N., Liu, Y.-Y. & Momeni, B. Impact of temporal pH fluctuations on the coexistence of nasal bacteria in an in silico community. *Front. Microbiol.* **12,** 613109 (2021).
5. Zhang, Y., Li, J.-T., Xu, X., Chen, H.-Y., Zhu, T., Xu, J.-J., Xu, X.-N., Li, J.-Q., Liang, C., Li, B., Fang, C.-M. & Nie, M. Temperature fluctuation promotes the thermal adaptation of soil microbial respiration. *Nat. Ecol. Evol.* **7,** 205–213 (2023).
6. Cohen Susan E. & Golden Susan S. Circadian rhythms in cyanobacteria. *Microbiol. Mol. Biol. Rev.* **79,** 373–385 (2015).
7. Borer, B., Tecon, R. & Or, D. Spatial organization of bacterial populations in response to oxygen and carbon counter-gradients in pore networks. *Nat. Commun.* **9,** 769 (2018).
8. Seymour, J. R., Amin, S. A., Raina, J.-B. & Stocker, R. Zooming in on the phycosphere: the ecological interface for phytoplankton-bacteria relationships. *Nat. Microbiol.* **2,** 17065 (2017).
9. McCallum, G. & Tropini, C. The gut microbiota and its biogeography. *Nat. Rev. Microbiol.* **22,** 105–118 (2024).

10. Portell, X., Pot, V., Garnier, P., Otten, W. & Baveye, P. C. Microscale heterogeneity of the spatial distribution of organic matter can promote bacterial biodiversity in soils: Insights from computer simulations. *Front. Microbiol.* **9,** 1583 (2018).

11. Nunan, N., Schmidt, H. & Raynaud, X. The ecology of heterogeneity: soil bacterial communities and C dynamics. *Philos. Trans. R. Soc. Lond. B Biol. Sci.* **375,** 20190249 (2020).

12. Gravuer, K., Eskelinen, A., Winbourne, J. B. & Harrison, S. P. Vulnerability and resistance in the spatial heterogeneity of soil microbial communities under resource additions. *Proc. Natl. Acad. Sci. U. S. A.* **117,** 7263–7270 (2020).

13. Kuzyakov, Y. & Blagodatskaya, E. Microbial hotspots and hot moments in soil: Concept & review. *Soil Biol. Biochem.* **83,** 184–199 (2015).

14. Mondragón-Palomino, O., Poceviciute, R., Lignell, A., Griffiths, J. A., Takko, H. & Ismagilov, R. F. Three-dimensional imaging for the quantification of spatial patterns in microbiota of the intestinal mucosa. *Proc. Natl. Acad. Sci. U. S. A.* **119,** e2118483119 (2022).

15. Nadell, C. D., Drescher, K. & Foster, K. R. Spatial structure, cooperation and competition in biofilms. *Nat. Rev. Microbiol.* **14,** 589–600 (2016).

16. Martín-Rodríguez, A. J. Respiration-induced biofilm formation as a driver for bacterial niche colonization. *Trends Microbiol.* (2022).

17. Cremin, K., Duxbury, S. J. N., Rosko, J. & Soyer, O. S. Formation and emergent dynamics of spatially organized microbial systems. *Interface Focus* **13,** 20220062 (2023).

18. Lodge, D. J., McDowell, W. H. & McSwiney, C. P. The importance of nutrient pulses in tropical forests. *Trends Ecol. Evol.* **9,** 384–387 (1994).

19. Smriga, S., Fernandez, V. I., Mitchell, J. G. & Stocker, R. Chemotaxis toward phytoplankton drives organic matter partitioning among marine bacteria. *Proc. Natl. Acad. Sci. U. S. A.* **113,** 1576–1581 (2016).

20. Blackburn, N., Fenchel, T. & Mitchell, J. Microscale nutrient patches in planktonic habitats shown by chemotactic bacteria. *Science* **282,** 2254–2256 (1998).

21. Taylor, J. R. & Stocker, R. Trade-offs of chemotactic foraging in turbulent water. *Science* **338,** 675–679 (2012).

22. Formenti, F., Bommakanti, N., Chen, R., Cronin, J. N., McPeak, H., Holopherne-Doran, D., Hedenstierna, G., Hahn, C. E. W., Larsson, A. & Farmery, A. D. Respiratory oscillations in alveolar oxygen tension measured in arterial blood. *Sci. Rep.* **7,** 1–10 (2017).

23. Lozupone, C. A., Stombaugh, J. I., Gordon, J. I., Jansson, J. K. & Knight, R. Diversity, stability and resilience of the human gut microbiota. *Nature* **489,** 220–230 (2012).

24. Enfors, S. O., Jahic, M., Rozkov, A., Xu, B., Hecker, M., Jürgen, B., Krüger, E., Schweder, T., Hamer, G., O'Beirne, D., Noisommit-Rizzi, N., Reuss, M., Boone, L., Hewitt, C., McFarlane, C., Nienow, A., Kovacs, T., Trägårdh, C., Fuchs, L., Revstedt, J., Friberg, P. C., Hjertager, B., Blomsten, G., Skogman, H., Hjort, S., Hoeks, F., Lin, H. Y., Neubauer, P., van der Lans, R., Luyben, K., Vrabel, P. & Manelius, A. Physiological responses to mixing in large scale bioreactors. *J. Biotechnol.* **85,** 175–185 (2001).

25. Takors, R. Scale-up of microbial processes: Impacts, tools and open questions. *J. Biotechnol.* **160,** 3–9 (2012).

26. Bisgaard, J., Muldbak, M., Tajsoleiman, T., Rydal, T., Rasmussen, T., Huusom, J. K. & Gernaey, K. V. Characterization of mixing performance in bioreactors using flow-following sensor devices. *Chem. Eng. Res. Des.* **174,** 471–485 (2021).

27. Nauha, E. K., Kálal, Z., Ali, J. M. & Alopaeus, V. Compartmental modeling of large stirred tank bioreactors with high gas volume fractions. *Chem. Eng. J.* **334,** 2319–2334 (2018).

28. Lara, A. R., Galindo, E., Ramírez, O. T. & Palomares, L. A. Living with heterogeneities in bioreactors: understanding the effects of environmental gradients on cells. *Mol. Biotechnol.* **34,** 355–381 (2006).

29. Nieß, A., Löffler, M., Simen, J. D. & Takors, R. Repetitive short-term stimuli imposed in poor mixing zones induce long-term adaptation of *E. coli* cultures in large-scale bioreactors: Experimental evidence and mathematical model. *Front. Microbiol.* **8,** 1195 (2017).

30. Miethke, M. & Marahiel, M. A. Siderophore-based iron acquisition and pathogen control. *Microbiol. Mol. Biol. Rev.* **71,** 413–451 (2007).

31. Partridge, J. D., Scott, C., Tang, Y., Poole, R. K. & Green, J. *Escherichia coli* transcriptome dynamics during the transition from anaerobic to aerobic conditions. *J. Biol. Chem.* **281,** 27806–27815 (2006).

32. André, A. C., Debande, L. & Marteyn, B. S. The selective advantage of facultative anaerobes relies on their unique ability to cope with changing oxygen levels during infection. *Cell. Microbiol.* **23,** e13338 (2021).

33. Ren, T., Jin, X., Deng, S., Guo, K., Gao, Y., Shi, X., Xu, L., Bai, X., Shang, Y., Jin, P. & Wang, X. C. Oxygen sensing regulation mechanism of *Thauera* bacteria in simultaneous nitrogen and phosphorus removal process. *J. Clean. Prod.* **434,** 140332 (2024).

34. Murashko, O. N. & Lin-Chao, S. *Escherichia coli* responds to environmental changes using enolasic degradosomes and stabilized DicF sRNA to alter cellular morphology. *Proc. Natl. Acad. Sci. U. S. A.* **114,** E8025–E8034 (2017).

35. Yasid, N. A., Rolfe, M. D., Green, J. & Williamson, M. P. Homeostasis of metabolites in *Escherichia coli* on transition from anaerobic to aerobic conditions and the transient secretion of pyruvate. *R. Soc. Open Sci.* **3,** 160187 (2016).

36. Von Wulffen, J., RecogNice-Team, Sawodny, O. & Feuer, R. Transition of an anaerobic *Escherichia coli* culture to aerobiosis: balancing mRNA and protein levels in a demand-directed dynamic flux balance analysis. *PLoS One* **11,** e0158711 (2016).

37. Pedraz, L., Blanco-Cabra, N. & Torrents, E. Gradual adaptation of facultative anaerobic pathogens to microaerobic and anaerobic conditions. *FASEB J.* **34,** 2912–2928 (2020).

38. Cabiscol, E., Tamarit, J. & Ros, J. Oxidative stress in bacteria and protein damage by reactive oxygen species. *Int. Microbiol.* **3,** 3–8 (2000).

39. Nguyen, J., Pepin, D. M. & Tropini, C. Cause or effect? The spatial organization of pathogens and the gut microbiota in disease. *Microbes Infect.* **23,** 104815 (2021).

40. Guo, R., Ma, X., Zhang, J., Liu, C., Thu, C. A., Win, T. N., Aung, N. L., Win, H. S., Naing, S., Li, H., Zhou, F. & Wang, P. Microbial community structures and important taxa across oxygen gradients in the Andaman Sea and eastern Bay of Bengal epipelagic waters. *Front. Microbiol.* **13,** 1041521 (2022).

41. Hibbing, M. E., Fuqua, C., Parsek, M. R. & Peterson, S. B. Bacterial competition: surviving and thriving in the microbial jungle. *Nat. Rev. Microbiol.* **8,** 15–25 (2010).

42. Kindler, O., Pulkkinen, O., Cherstvy, A. G. & Metzler, R. Burst statistics in an early biofilm quorum sensing model: the role of spatial colony-growth heterogeneity. *Sci. Rep.* **9,** 12077 (2019).

43. Long, A. M., Jurgensen, S. K., Petchel, A. R., Savoie, E. R. & Brum, J. R. Microbial ecology of oxygen minimum zones amidst ocean deoxygenation. *Front. Microbiol.* **12,** 748961 (2021).

44. Byndloss, M. X., Pernitzsch, S. R. & Bäumler, A. J. Healthy hosts rule within: ecological forces shaping the gut microbiota. *Mucosal Immunol.* **11,** 1299–1305 (2018).

45. Whitesides, G. M. The origins and the future of microfluidics. *Nature* **442,** 368–373 (2006).

46. Mashaghi, S., Abbaspourrad, A., Weitz, D. A. & van Oijen, A. M. Droplet microfluidics: a tool for biology, chemistry and nanotechnology. *Trends Analyt. Chem.* **82,** 118–125 (2016).
47. Leung, C. M., de Haan, P., Ronaldson-Bouchard, K., Kim, G.-A., Ko, J., Rho, H. S., Chen, Z., Habibovic, P., Jeon, N. L., Takayama, S., Shuler, M. L., Vunjak-Novakovic, G., Frey, O., Verpoorte, E. & Toh, Y.-C. A guide to the organ-on-a-chip. *Nat. Rev. Methods Primers* **2,** 1–29 (2022).
48. Chang, C.-W., Cheng, Y.-J., Tu, M., Chen, Y.-H., Peng, C.-C., Liao, W.-H. & Tung, Y.-C. A polydimethylsiloxane–polycarbonate hybrid microfluidic device capable of generating perpendicular chemical and oxygen gradients for cell culture studies. *Lab Chip* **14,** 3762–3772 (2014).
49. Koens, R., Tabata, Y., Serrano, J. C., Aratake, S., Yoshino, D., Kamm, R. D. & Funamoto, K. Microfluidic platform for three-dimensional cell culture under spatiotemporal heterogeneity of oxygen tension. *APL Bioeng* **4,** 016106 (2020).
50. Polinkovsky, M., Gutierrez, E., Levchenko, A. & Groisman, A. Fine temporal control of the medium gas content and acidity and on-chip generation of series of oxygen concentrations for cell cultures. *Lab Chip* **9,** 1073–1084 (2009).
51. Skolimowski, M., Nielsen, M. W., Emnéus, J., Molin, S., Taboryski, R., Sternberg, C., Dufva, M. & Geschke, O. Microfluidic dissolved oxygen gradient generator biochip as a useful tool in bacterial biofilm studies. *Lab Chip* **10,** 2162–2169 (2010).
52. Abaci, H. E., Devendra, R., Soman, R., Drazer, G. & Gerecht, S. Microbioreactors to manipulate oxygen tension and shear stress in the microenvironment of vascular stem and progenitor cells. *Biotechnol. Appl. Biochem.* **59,** 97–105 (2012).
53. Funamoto, K., Zervantonakis, I. K., Liu, Y., Ochs, C. J., Kim, C. & Kamm, R. D. A novel microfluidic platform for high-resolution imaging of a three-dimensional cell culture under a controlled hypoxic environment. *Lab Chip* **12,** 4855–4863 (2012).
54. Lam, S. F., Shirure, V. S., Chu, Y. E., Soetikno, A. G. & George, S. C. Microfluidic device to attain high spatial and temporal control of oxygen. *PLoS One* **13,** e0209574 (2018).
55. Lindemann, D., Westerwalbesloh, C., Kohlheyer, D., Grünberger, A. & von Lieres, E. Microbial single-cell growth response at defined carbon limiting conditions. *RSC Adv.* **9,** 14040–14050 (2019).

56. Mustafi, N., Grünberger, A., Mahr, R., Helfrich, S., Nöh, K., Blombach, B., Kohlheyer, D. & Frunzke, J. Application of a genetically encoded biosensor for live cell imaging of L-valine production in pyruvate dehydrogenase complex-deficient *Corynebacterium glutamicum* strains. *PLoS One* **9,** e85731 (2014).

57. Burmeister, A., Hilgers, F., Langner, A., Westerwalbesloh, C., Kerkhoff, Y., Tenhaef, N., Drepper, T., Kohlheyer, D., von Lieres, E., Noack, S. & Grünberger, A. A microfluidic co-cultivation platform to investigate microbial interactions at defined microenvironments. *Lab Chip* **19,** 98–110 (2018).

58. Mukherjee, S. & Bassler, B. L. Bacterial quorum sensing in complex and dynamically changing environments. *Nat. Rev. Microbiol.* **17,** 371–382 (2019).

59. Burmeister, A. & Grünberger, A. Microfluidic cultivation and analysis tools for interaction studies of microbial co-cultures. *Curr. Opin. Biotechnol.* **62,** 106–115 (2020).

60. Schito, S., Zuchowski, R., Bergen, D., Strohmeier, D., Wollenhaupt, B., Menke, P., Seiffarth, J., Nöh, K., Kohlheyer, D., Bott, M., Wiechert, W., Baumgart, M. & Noack, S. Communities of Niche-optimized Strains (CoNoS) – Design and creation of stable, genome-reduced co-cultures. *Metab. Eng.* **73,** 91–103 (2022).

61. Ren, J., Wang, N., Guo, P., Fan, Y., Lin, F. & Wu, J. Recent advances in microfluidics-based cell migration research. *Lab Chip* **22,** 3361–3376 (2022).

62. Scheidweiler, D., Bordoloi, A. D., Jiao, W., Sentchilo, V., Bollani, M., Chhun, A., Engel, P. & de Anna, P. Spatial structure, chemotaxis and quorum sensing shape bacterial biomass accumulation in complex porous media. *Nat. Commun.* **15,** 191 (2024).

63. Gupta, S., Ross, T. D., Gomez, M. M., Grant, J. L., Romero, P. A. & Venturelli, O. S. Investigating the dynamics of microbial consortia in spatially structured environments. *Nat. Commun.* **11,** 2418 (2020).

64. Wu, H. M., Lee, T. A., Ko, P. L., Chiang, H. J., Peng, C. C. & Tung, Y. C. Review of microfluidic cell culture devices for the control of gaseous microenvironments in vitro. *J. Micromech. Microeng.* **28** (2018).

65. Täuber, S., Golze, C., Ho, P., von Lieres, E. & Grünberger, A. dMSCC: a microfluidic platform for microbial single-cell cultivation of *Corynebacterium glutamicum* under dynamic environmental medium conditions. *Lab Chip* **20,** 4442–4455 (2020).

66. Nguyen, J., Fernandez, V., Pontrelli, S., Sauer, U., Ackermann, M. & Stocker, R. A distinct growth physiology enhances bacterial growth under rapid nutrient fluctuations. *Nat. Commun.* **12,** 3662 (2021).

67. Tang, Q., Wang, D., Cui, J., Zhang, Y., Mei, J., Du, J., Xia, A., Sun, Q., Luo, D., Han, B., Gan, M. & Liu, P. Microfluidic-based spatiotemporal control of oxygen concentration in bacteria suspension culture from bulk to the single cells. *Nano Today* **54,** 102067 (2024).

68. Nguyen, J., Lara-Gutiérrez, J. & Stocker, R. Environmental fluctuations and their effects on microbial communities, populations and individuals. *FEMS Microbiol. Rev.* **45** (2021).

69. Menolascina, F., Rusconi, R., Fernandez, V. I., Smriga, S., Aminzare, Z., Sontag, E. D. & Stocker, R. Logarithmic sensing in *Bacillus subtilis* aerotaxis. *NPJ Syst. Biol. Appl.* **3,** 16036 (2017).

70. Kirkegaard, J. B., Bouillant, A., Marron, A. O., Leptos, K. C. & Goldstein, R. E. Aerotaxis in the closest relatives of animals. *Elife* **5** (2016).

71. Adler, M., Erickstad, M., Gutierrez, E. & Groisman, A. Studies of bacterial aerotaxis in a microfluidic device. *Lab Chip* **12,** 4835–4847 (2012).

72. Lindström, S. & Andersson-Svahn, H. Overview of single-cell analyses: microdevices and applications. *Lab Chip* **10,** 3363–3372 (2010).

73. Stuart, T. & Satija, R. Integrative single-cell analysis. *Nat. Rev. Genet.* **20,** 257–272 (2019).

74. Armbrecht, L. & Dittrich, P. S. Recent advances in the analysis of single cells. *Anal. Chem.* **89,** 2–21 (2017).

75. Murphy, T. W., Zhang, Q., Naler, L. B., Ma, S. & Lu, C. Recent advances in the use of microfluidic technologies for single cell analysis. *Analyst* **143,** 60–80 (2018).

76. Gao, D., Jin, F., Zhou, M. & Jiang, Y. Recent advances in single cell manipulation and biochemical analysis on microfluidics. *Analyst* **144,** 766–781 (2019).

77. Campos, M., Surovtsev, I. V., Kato, S., Paintdakhi, A., Beltran, B., Ebmeier, S. E. & Jacobs-Wagner, C. A constant size extension drives bacterial cell size homeostasis. *Cell* **159,** 1433–1446 (2014).

78. Grünberger, A., Probst, C., Helfrich, S., Nanda, A., Stute, B., Wiechert, W., von Lieres, E., Nöh, K., Frunzke, J. & Kohlheyer, D. Spatiotemporal microbial single-cell analysis using a high-throughput microfluidics cultivation platform. *Cytometry A* **87,** 1101–1115 (2015).

79. Taheri-Araghi, S., Bradde, S., Sauls, J. T., Hill, N. S., Levin, P. A., Paulsson, J., Vergassola, M. & Jun, S. Cell-size control and homeostasis in bacteria. *Curr. Biol.* **25,** 385–391 (2015).

80. Xia, Y. & Whitesides, G. M. Soft lithography. *Annu. Rev. Mater. Sci.* **28,** 153–184 (1998).

81. Qin, D., Xia, Y. & Whitesides, G. M. Soft lithography for micro- and nanoscale patterning. *Nat. Protoc.* **5,** 491–502 (2010).

82. Vollmer, A. P., Probstein, R. F., Gilbert, R. & Thorsen, T. Development of an integrated microfluidic platform for dynamic oxygen sensing and delivery in a flowing medium. *Lab Chip* **5,** 1059–1066 (2005).

83. Markov, D. A., Lillie, E. M., Garbett, S. P. & McCawley, L. J. Variation in diffusion of gases through PDMS due to plasma surface treatment and storage conditions. *Biomed. Microdevices* **16,** 91–96 (2014).

84. Wang, P., Robert, L., Pelletier, J., Dang, W. L., Taddei, F., Wright, A. & Jun, S. Robust growth of *Escherichia coli*. *Curr. Biol.* **20,** 1099–1103 (2010).

85. Choudhary, D., Lagage, V., Foster, K. R. & Uphoff, S. Phenotypic heterogeneity in the bacterial oxidative stress response is driven by cell-cell interactions. *Cell Rep.* **42,** 112168 (2023).

86. Westerwalbesloh, C., Grünberger, A., Stute, B., Weber, S., Wiechert, W., Kohlheyer, D. & von Lieres, E. Modeling and CFD simulation of nutrient distribution in picoliter bioreactors for bacterial growth studies on single-cell level. *Lab Chip* **15,** 4177–4186 (2015).

87. Clark Jr, L. C. & Lyons, C. Electrode systems for continuous monitoring in cardiovascular surgery. *Ann. N. Y. Acad. Sci.* **102,** 29–45 (1962).

88. Grist, S. M., Chrostowski, L. & Cheung, K. C. Optical oxygen sensors for applications in microfluidic cell culture. *Sensors (Basel)* **10,** 9286–9316 (2010).

89. Wu, C.-C., Yasukawa, T., Shiku, H. & Matsue, T. Fabrication of miniature Clark oxygen sensor integrated with microstructure. *Sens. Actuators B Chem.* **110,** 342–349 (2005).

90. Suresh, S., Srivastava, V. C. & Mishra, I. M. Techniques for oxygen transfer measurement in bioreactors: a review. *J. Chem. Technol. Biotechnol.* **84,** 1091–1103 (2009).

91. Wang, W., Li, L., Ding, M., Luo, G. & Liang, Q. A microfluidic hydrogel chip with orthogonal dual gradients of matrix stiffness and oxygen for cytotoxicity test. *Biochip J.* **12,** 93–101 (2018).

92. Sun, W., Chen, Y., Wang, Y., Luo, P., Zhang, M., Zhang, H. & Hu, P. Interaction study of cancer cells and fibroblasts on a spatially confined oxygen gradient microfluidic chip to investigate the tumor microenvironment. *Analyst* **143,** 5431–5437 (2018).

93. Liu, P., Fu, L., Li, B., Man, M., Ji, Y., Kang, Q., Sun, X., Shen, D. & Chen, L. Dissolved oxygen gradient on three dimensionally printed microfluidic platform for studying its effect on fish at three levels: cell, embryo, and larva. *Environ. Sci. Pollut. Res. Int.* **30,** 21978–21989 (2023).

94. Ungerböck, B., Charwat, V., Ertl, P. & Mayr, T. Microfluidic oxygen imaging using integrated optical sensor layers and a color camera. *Lab Chip* **13,** 1593–1601 (2013).

95. Gerritsen, H. C., Sanders, R., Draaijer, A., Ince, C. & Levine, Y. K. Fluorescence lifetime imaging of oxygen in living cells. *J. Fluoresc.* **7,** 11–15 (1997).

96. Wu, H. M., Lee, T. A., Ko, P. L., Liao, W. H., Hsieh, T. H. & Tung, Y. C. Wide-field frequency domain fluorescence lifetime imaging microscopy (FD-FLIM) for accurate measurement of oxygen gradients within microfluidic devices. *Analyst* **144,** 3494–3504 (2019).

97. Hsu, H.-H., Ko, P.-L., Wu, H.-M., Lin, H.-C., Wang, C.-K. & Tung, Y.-C. Study 3D endothelial cell network formation under various oxygen microenvironment and hydrogel composition combinations using upside-down microfluidic devices. *Small* **17,** e2006091 (2021).

98. Gehlen, M. H. The centenary of the Stern-Volmer equation of fluorescence quenching: from the single line plot to the SV quenching map. *J. Photochem. Photobiol. C: Photochem. Rev.* **42,** 100338 (2020).

99. Hartmann, P., Leiner, M. J. P. & Lippitsch, M. E. Luminescence quenching behavior of an oxygen sensor based on a Ru(II) complex dissolved in polystyrene. *Anal. Chem.* **67,** 88–93 (1995).

100. Htun, T. A negative deviation from stern-volmer equation in fluorescence quenching. *J. Fluoresc.* **14,** 217–222 (2004).

101. Lakowicz, J. R. *Principles of fluorescence spectroscopy* 3rd ed. (Springer, 2006).

102. McNeil, C. L. & D'Asaro, E. A. A calibration equation for oxygen optodes based on physical properties of the sensing foil: new calibration equation for optodes. *Limnol. Oceanogr. Methods* **12,** 139–154 (2014).

103. Kasahara, K., Leygeber, M., Seiffarth, J., Ruzaeva, K., Drepper, T., Nöh, K. & Kohlheyer, D. Enabling oxygen-controlled microfluidic cultures for spatiotemporal microbial single-cell analysis. *Front. Microbiol.* **14,** 1198170 (2023).

104. Seiffarth, J., Scherr, T., Wollenhaupt, B., Neumann, O., Scharr, H., Kohlheyer, D., Mikut, R. & Nöh, K. ObiWan-Microbi: OMERO-based integrated workflow for annotating microbes in the cloud. *SoftwareX* **26,** 101638 (2024).

105. Schindelin, J., Arganda-Carreras, I., Frise, E., Kaynig, V., Longair, M., Pietzsch, T., Preibisch, S., Rueden, C., Saalfeld, S., Schmid, B., Tinevez, J. Y., White, D. J., Hartenstein, V., Eliceiri, K., Tomancak, P. & Cardona, A. Fiji: an open-source platform for biological-image analysis. *Nat. Methods* **9,** 676–682 (2012).

106. Parslow, A., Cardona, A. & Bryson-Richardson, R. J. Sample drift correction following 4D confocal time-lapse imaging. *J. Vis. Exp.* (2014).

107. Allan, C., Burel, J.-M., Moore, J., Blackburn, C., Linkert, M., Loynton, S., MacDonald, D., Moore, W. J., Neves, C., Patterson, A., Porter, M., Tarkowska, A., Loranger, B., Avondo, J., Lagerstedt, I., Lianas, L., Leo, S., Hands, K., Hay, R. T., Patwardhan, A., Best, C., Kleywegt, G. J., Zanetti, G. & Swedlow, J. R. OMERO: flexible, model-driven data management for experimental biology. *Nat. Methods* **9,** 245–253 (2012).

108. Cutler, K. J., Stringer, C., Lo, T. W., Rappez, L., Stroustrup, N., Brook Peterson, S., Wiggins, P. A. & Mougous, J. Omnipose: a high-precision morphology-independent solution for bacterial cell segmentation. *Nat. Methods* **19,** 1438–1448 (2022).

109. Albrecht, W., Moers, J. & Hermanns, B. HNF - Helmholtz Nano Facility. *JLSRF* **3,** A112–A112 (2017).

110. Kalinina, S., Breymayer, J., Schäfer, P., Calzia, E., Shcheslavskiy, V., Becker, W. & Rück, A. Correlative NAD(P)H-FLIM and oxygen sensing-PLIM for metabolic mapping. *J. Biophotonics* **9,** 800–811 (2016).

111. Ruzaeva, K., Cohrs, J.-C., Kasahara, K., Kohlheyer, D., Nöh, K. & Berkels, B. *Cell tracking for live-cell microscopy using an activity-prioritized assignment strategy* in *2022 IEEE 5th International Conference on Image Processing Applications and Systems (IPAS)* (IEEE, 2022), 1–7.

112. Kirby, B. J. *Micro- and nanoscale fluid mechanics* (Cambridge University Press, 2010).

113. Hansen, M. C., Palmer, R. J., Udsen, C., White, D. C. & Molin, S. Assessment of GFP fluorescence in cells of *Streptococcus gordonii* under conditions of low pH and low oxygen concentration. *Microbiology* **147,** 1383–1391 (2001).

114. Stolpera, D. A., Revsbech, N. P. & Canfield, D. E. Aerobic growth at nanomolar oxygen concentrations. *Proc. Natl. Acad. Sci. U. S. A.* **107,** 18755–18760 (2010).

115. Grünberger, A., van Ooyen, J., Paczia, N., Rohe, P., Schiendzielorz, G., Eggeling, L., Wiechert, W., Kohlheyer, D. & Noack, S. Beyond growth rate 0.6: *Corynebacterium glutamicum* cultivated in highly diluted environments. *Biotechnol. Bioeng.* **110,** 220–228 (2013).

116. Berg, J. S., Ahmerkamp, S., Pjevac, P., Hausmann, B., Milucka, J. & Kuypers, M. M. M. How low can they go? Aerobic respiration by microorganisms under apparent anoxia. *FEMS Microbiol. Rev.* **46,** fuac006 (2022).

117. Ishii, S., Tago, K. & Senoo, K. Single-cell analysis and isolation for microbiology and biotechnology: methods and applications. *Appl. Microbiol. Biotechnol.* **86,** 1281–1292 (2010).

118. Czechowska, K., Johnson, D. R. & van der Meer, J. R. Use of flow cytometric methods for single-cell analysis in environmental microbiology. *Curr. Opin. Microbiol.* **11,** 205–212 (2008).

119. Joensson, H. N. & Andersson Svahn, H. Droplet microfluidics–a tool for single-cell analysis. *Angew. Chem. Int. Ed Engl.* **51,** 12176–12192 (2012).

120. Grünberger, A., Paczia, N., Probst, C., Schendzielorz, G., Eggeling, L., Noack, S., Wiechert, W. & Kohlheyer, D. A disposable picolitre bioreactor for cultivation and investigation of industrially relevant bacteria on the single cell level. *Lab Chip* **12,** 2060–2068 (2012).

121. Zhang, W. Y., Ferguson, G. S. & Tatic-Lucic, S. *Elastomer-supported cold welding for room temperature wafer-level bonding* in *17th IEEE International Conference on Micro Electro Mechanical Systems. Maastricht MEMS 2004 Technical Digest* (IEEE, 2004), 741–744.

122. Merlin, C., Masters, M., McAteer, S. & Coulson, A. Why is carbonic anhydrase essential to *Escherichia coli*? *J. Bacteriol.* **185,** 6415–6424 (2003).

123. Couvert, O., Divanac'h, M.-L., Lochardet, A., Thuault, D. & Huchet, V. Modelling the effect of oxygen concentration on bacterial growth rates. *Food Microbiol.* **77,** 21–25 (2019).

124. Tuttle, A. R., Trahan, N. D. & Son, M. S. Growth and Maintenance of *Escherichia coli* Laboratory Strains. *Curr. Protoc.* **1,** e20 (2021).

125. Goldblatt, C., Lenton, T. M. & Watson, A. J. Bistability of atmospheric oxygen and the Great Oxidation. *Nature* **443,** 683–686 (2006).

126. Schaechter, M., Maaloe, O. & Kjeldgaard, N. O. Dependency on medium and temperature of cell size and chemical composition during balanced grown of *Salmonella typhimurium*. *J. Gen. Microbiol.* **19,** 592–606 (1958).

127. Bertaux, F., von Kügelgen, J., Marguerat, S. & Shahrezaei, V. A bacterial size law revealed by a coarse-grained model of cell physiology. *PLoS Comput. Biol.* **16,** e1008245 (2020).

128. Partridge, J. D., Sanguinetti, G., Dibden, D. P., Roberts, R. E., Poole, R. K. & Green, J. Transition of *Escherichia coli* from aerobic to micro-aerobic conditions involves fast and slow reacting regulatory components. *J. Biol. Chem.* **282,** 11230–11237 (2007).

129. Von Wulffen, J., Ulmer, A., Jäger, G., Sawodny, O. & Feuer, R. Rapid sampling of *Escherichia coli* after changing oxygen conditions reveals transcriptional dynamics. *Genes* **8** (2017).

130. Beauchene, N. A., Mettert, E. L., Moore, L. J., Keleş, S., Willey, E. R. & Kiley, P. J. O_2 availability impacts iron homeostasis in *Escherichia coli*. *Proc. Natl. Acad. Sci. U. S. A.* **114,** 12261–12266 (2017).

131. Rolfe, M. D., Ocone, A., Stapleton, M. R., Hall, S., Trotter, E. W., Poole, R. K., Sanguinetti, G., Green, J. & SysMO-SUMO Consortium. Systems analysis of transcription factor activities in environments with stable and dynamic oxygen concentrations. *Open Biol.* **2,** 120091 (2012).

132. Wu, H. M., Lee, T. A., Ko, P. L., Liao, W. H., Hsieh, T. H. & Tung, Y. C. Wide-field frequency domain fluorescence lifetime imaging microscopy (FD-FLIM) for accurate measurement of oxygen gradients within microfluidic devices. *Analyst* **144,** 3494–3504 (2019).

133. Marteyn, B., Scorza, F. B., Sansonetti, P. J. & Tang, C. Breathing life into pathogens: the influence of oxygen on bacterial virulence and host responses in the gastrointestinal tract. *Cell. Microbiol.* **13,** 171–176 (2011).

134. Henson, M. A. & Phalak, P. Microbiota dysbiosis in inflammatory bowel diseases: in silico investigation of the oxygen hypothesis. *BMC Syst. Biol.* **11,** 145 (2017).

135. Singhal, R. & Shah, Y. M. Oxygen battle in the gut: Hypoxia and hypoxia-inducible factors in metabolic and inflammatory responses in the intestine. *J. Biol. Chem.* **295,** 10493–10505 (2020).

136. Ward, J. B. J., Keely, S. J. & Keely, S. J. Oxygen in the regulation of intestinal epithelial transport. *J. Physiol.* **592,** 2473–2489 (2014).

137. Zheng, L., Kelly, C. J. & Colgan, S. P. Physiologic hypoxia and oxygen homeostasis in the healthy intestine. A review in the theme: cellular responses to hypoxia. *Am. J. Physiol. Cell Physiol.* **309,** C350–60 (2015).

138. Moreno-Indias, I., Torres, M., Montserrat, J. M., Sanchez-Alcoholado, L., Cardona, F., Tinahones, F. J., Gozal, D., Poroyko, V. A., Navajas, D., Queipo-Ortuño, M. I. & Farré, R. Intermittent hypoxia alters gut microbiota diversity in a mouse model of sleep apnoea. *Eur. Respir. J.* **45,** 1055–1065 (2015).

139. Risely, A., Wilhelm, K., Clutton-Brock, T., Manser, M. B. & Sommer, S. Diurnal oscillations in gut bacterial load and composition eclipse seasonal and lifetime dynamics in wild meerkats. *Nat. Commun.* **12,** 6017 (2021).

140. Becker, J. & Wittmann, C. Bio-based production of chemicals, materials and fuels - *Corynebacterium glutamicum* as versatile cell factory. *Curr. Opin. Biotechnol.* **23,** 631–640 (2012).

141. Zahoor, A., Lindner, S. N. & Wendisch, V. F. Metabolic engineering of *Corynebacterium glutamicum* aimed at alternative carbon sources and new products. *Comput. Struct. Biotechnol. J.* **3,** e201210004 (2012).

142. Takeno, S., Ohnishi, J., Komatsu, T., Masaki, T., Sen, K. & Ikeda, M. Anaerobic growth and potential for amino acid production by nitrate respiration in *Corynebacterium glutamicum*. *Appl. Microbiol. Biotechnol.* **75,** 1173–1182 (2007).

143. Nishimura, T., Vertès, A. A., Shinoda, Y., Inui, M. & Yukawa, H. Anaerobic growth of *Corynebacterium glutamicum* using nitrate as a terminal electron acceptor. *Appl. Microbiol. Biotechnol.* **75,** 889–897 (2007).

144. Michel, A., Koch-Koerfges, A., Krumbach, K., Brocker, M. & Bott, M. Anaerobic growth of *Corynebacterium glutamicum* via mixed-acid fermentation. *Appl. Environ. Microbiol.* **81,** 7496–7508 (2015).

145. Tsuge, Y. & Yamaguchi, A. Physiological characteristics of *Corynebacterium glutamicum* as a cell factory under anaerobic conditions. *Appl. Microbiol. Biotechnol.* **105,** 6173–6181 (2021).

146. Keilhauer, C., Eggeling, L. & Sahm, H. Isoleucine synthesis in *Corynebacterium glutamicum*: molecular analysis of the ilvB-ilvN-ilvC operon. *J. Bacteriol.* **175,** 5595–5603 (1993).

147. Erickstad, M., Hale, L. A., Chalasani, S. H. & Groisman, A. A microfluidic system for studying the behavior of zebrafish larvae under acute hypoxia. *Lab Chip* **15,** 857–866 (2015).

148. Marcinkevi Ius, A., Juodkazis, S., Watanabe, M., Miwa, M., Matsuo, S., Misawa, H. & Nishii, J. Femtosecond laser-assisted three-dimensional microfabrication in silica. *Opt. Lett.* **26,** 277–279 (2001).

149. Hermans, M. Selective, laser-induced etching of fused silica at high scan-speeds using KOH. *J. Laser Micro/nanoeng.* **9,** 126–131 (2014).

150. Gottmann, J., Hermans, M., Repiev, N. & Ortmann, J. Selective laser-induced etching of 3D precision quartz glass components for microfluidic applications—up-scaling of complexity and speed. *Micromachines (Basel)* **8,** 110 (2017).

151. Gholivand, A., Korculanin, O., Dahlhoff, K., Babaki, M., Dickscheid, T. & Lettinga, M. P. Effect of in-plane and out-of-plane bifurcated microfluidic channels on the flow of aggregating red blood cells. *Lab Chip* **24,** 2317–2326 (2024).

152. Kim, M.-C., Lam, R. H. W., Thorsen, T. & Asada, H. H. Mathematical analysis of oxygen transfer through polydimethylsiloxane membrane between double layers of cell culture channel and gas chamber in microfluidic oxygenator. *Microfluid. Nanofluidics* **15,** 285–296 (2013).

Publications

Peer-Reviewed Journal Articles

Keitaro Kasahara, Dietrich Kohlheyer, “Creating rapid oxygen oscillations in microbial single-cell growth analysis using microfluidic double-layer device," ***Journal of Visualized Experiments***, accepted.

Keitaro Kasahara, Johannes Seiffarth, Birgit Stute, Eric von Lieres, Thomas Drepper, Katharina Nöh, Dietrich Kohlheyer, “Unveiling periodic microbial growth dynamics synchronized with rapidly fluctuating oxygen environments," ***Lab on a Chip***, **25**, pp.2234-2246 (2025).

Keitaro Kasahara†, Markus Leygeber†, Johannes Seiffarth, Karina Ruzaeva, Thomas Drepper, Katharina Nöh, Dietrich Kohlheyer, “Enabling oxygen-controlled microfluidic cultures for spatiotemporal microbial single-cell analysis," ***Frontiers in Microbiology***, **14**, 1198170 (2023). (†equal contribution)

Peer-Reviewed Journal Articles (not related to the dissertation)

Daiki Miyata, **Keitaro Kasahara**, Yujin Taguchi, Yuta Tokuoka, Takahiro Yamada, Yuta Kurashina, Akira Funahashi, Hiroaki Onoe, “Autonomous exploration system of electrical stimulus condition for maturating *in vitro* skeletal muscle tissue with Bayesian optimization (in Japanese),” ***IEEJ Transactions on Sensors and Micromachines***, **145**, 3, pp.33-40 (2025).

Keitaro Kasahara, Jumpei Muramatsu, Yuta Kurashina, Shigenori Miura, Shogo Miyata, Hiroaki Onoe, “Spatiotemporal single-cell tracking analysis in 3D tissues to reveal heterogeneous cellular response to mechanical stimuli,” ***Science Advances***, **9**, eadf9917 (2023).

International Conference Contributions

Keitaro Kasahara, Johannes Seiffarth, Katharina Nöh, Dietrich Kohlheyer, "Spatiotemporally resolved microbial behavioral analysis with a clear correlation to rapid oxygen fluctuations," ***28th International Conference on Miniaturized Systems for Chemistry and Life Sciences (μTAS 2024)***, Oct. 2024 (oral presentation, Montreal, Canada).

Lennart Witting, **Keitaro Kasahara**, Dietrich Kohlheyer, "Cyanobacteria at single-cell resolution: From analyzing distinct colonies to multi-parameter growth models," ***13th International CeBiTec Research Conference***, Sep. 2024 (Bielefeld, Germany).

Keitaro Kasahara, Dietrich Kohlheyer, "Shaping spatiotemporal oxygen landscapes in microbial single-cell analysis," ***Annual conference 2023 of the Association for General and Applied Microbiology (VAAM)***, Sep. 2023 (poster, Göttingen, Germany) (Best Poster Presentation Award).

Lennart Witting, Marion Eisenhut, Andreas Weber, Tim Schulze, **Keitaro Kasahara**, Johannes Seiffarth, Dietrich Kohlheyer, "In vitro evolution of a synthetic organelle inside a picoliter habitat," ***Annual conference 2023 of the Association for General and Applied Microbiology (VAAM)***, Sep. 2023 (Göttingen, Germany).

Karina Ruzaeva, Jan-Christopher Cohrs, **Keitaro Kasahara**, Dietrich Kohlheyer, Katharina Nöh, Benjamin Berkels, "Cell tracking for live-cell microscopy using an activity-prioritized assignment strategy," ***Proceedings of the 5th IEEE International Conference on Image Processing Applications and Systems 2022 (IPAS)***, pp.1-7, Dec. 2022.

Keitaro Kasahara, Yuta Kurashina, Shigenori Miura, Shogo Miyata, Hiroaki Onoe, “Real-time three-dimensional single-cell-resolution monitoring system for observation of dynamic cell behavior under mechanical stimuli,” ***Proceedings of the 34th IEEE International Conference on Micro Electro Mechanical Systems (MEMS 2021)***, pp.454-457, Jan. 2021 (oral presentation, online).

Keitaro Kasahara, Yuta Kurashina, Shigenori Miura, Shogo Miyata, Hiroaki Onoe, “Shape deformation analysis of single cell in 3D tissue under mechanical stimuli,” ***Proceedings of the 20th International Conference on Solid-State Sensors, Actuators and Microsystems (Transducers 2019 / EUROSENSORS XXXIII Conference)***, pp.413-416, June 2019 (oral presentation, Berlin, Germany).

Other Conference Contributions

Keitaro Kasahara, Dietrich Kohlheyer, "Shaping spatiotemporal oxygen landscapes in microbial single-cell analysis," ***Fall meeting Topic 7: Towards a Sustainable Bioecon-***

omy – Resources, Utilization, Engineering and AgroEcosystems, Dec. 2023 (poster, Jülich, Germany).

Lennart Witting, **Keitaro Kasahara**, Dietrich Kohlheyer, "Cyanobacteria at single-cell level: New insights into population dynamics," ***Fall meeting Topic 7: Towards a Sustainable Bioeconomy – Resources, Utilization, Engineering and AgroEcosystems***, Dec. 2023 (Jülich, Germany).

Keitaro Kasahara, Dietrich Kohlheyer, "Dynamic structuring of oxygen landscapes in microbial single-cell analysis," ***CRC1535 MibiNet Retreat I***, Nov. 2023 (poster, Königswinter, Germany).

Keitaro Kasahara, Markus Leygeber, Dietrich Kohlheyer, "Enabling oxygen landscapes in microbial single-cell analysis," ***General Assembly 2023 of the Program "Changing Earth - Sustaining our Future"***, May 2023 (poster, Karlsruhe, Germany).

Lennart Witting, **Keitaro Kasahara**, Dietrich Kohlheyer, "A novel microfluidic cultivation device for cyanobacteria in high CO2 environments," ***General Assembly 2023 of the Program "Changing Earth - Sustaining our Future"***, May 2023 (poster, Karlsruhe, Germany).

Keitaro Kasahara, Markus Leygeber, Dietrich Kohlheyer, "Shaping oxygen landscapes in microbial single-cell analysis," ***PhD Workshop / Fall meeting Topic 7: Towards a Sustainable Bioeconomy – Resources, Utilization, Engineering and AgroEcosystems***, Nov. 2022 (poster, Leipzig, Germany).

List of Figures

1.1 Spatiotemporally structured environments in microbial habitats 2

1.2 Spatiotemporally fluctuating environments in an industrial-scale bioreactor 4

1.3 Microfluidic devices for spatiotemporal O_2 control 7

1.4 Microfluidic devices enabling microbial growth and interaction studies in confined environments 8

1.5 Schematic illustration describing the scope of the thesis 11

2.1 schematics of photo-lithography and soft lithography for PDMS-based microfluidic chip fabrication 16

2.2 Microbial single-cell analysis using microfluidic grooves and chambers . 17

2.3 Stern-volmer plot illustrating linear and non-linear relationship 18

2.4 Procedure of image analysis 20

3.1 Overview of the microfluidic cultivation system for spatiotemporal microbial single-cell analysis under controlled O_2 environments 22

3.2 Detailed design of the microfluidic chip 24

3.3 Detailed design of the mini-incubator 27

3.4 Setup for FLIM calibration of RTDP 31

3.5 FLIM imaging under various O_2 conditions 34

3.6 O_2 control performance characterization at 30°C 35

3.7 O_2 control performance characterization at 25°C 36

3.8 Time-lapse image series of *E. coli* MG1655 expressing GFP 38

3.9 Population based analysis of *E. coli* growth and GFP expression 39

3.10 Single-cell tracking of fluorescence intensities and generation numbers, analyzed for a selected population from aerobic conditions 41

3.11 Single-cell tracking of fluorescence intensities and generation numbers, analyzed for a selected population from anaerobic conditions with a switch to aerobic conditions 42

4.1 Conceptual illustration of the on-chip microbial growth analysis under rapidly fluctuating O_2 environment 46

4.2 Conceptual illustration of the fast gas exchange through the intermediate thin membrane 47

4.3 Conceptual illustration of the modular system 48

4.4 Fabrication procedure of the double-layer PDMS microfluidic chip 49

4.5 3D-printed mold for the upper layer with three separate gas channels . . . 49

4.6 Geometry of the PDMS chip generated for gas diffusion simulation 50

4.7 Fabricated double-layer microfluidic chip 55

4.8 Fabricated microfluidic chip with various designs 56

4.9 Mass flow controller optimization 57

4.10 Characterization of the on-chip O_2 control 58

4.11 O_2 concentration in the fluid channel of the microfluidic chip 59

4.12 *E. coli* growth rate under different cultivation conditions 60

4.13 *E. coli* cultivation under steady O_2 supplies 61

4.14 Growth curve based on colony area under various O_2 supplies 62

4.15 Exponential growth rate under various O_2 supplies 63

4.16 Single-cell area under various O_2 supplies at $t = 2$ h 64

4.17 Phase-contrast images of *E. coli* cultivated under oscillating O_2 supplies with $T' = 60$, 30, and 10 min 65

4.18 Phase-contrast images of *E. coli* cultivated under oscillating O_2 supplies with $T' = 5$, 2, and 1 min 66

4.19 *E. coli* growth analysis cultivated under oscillating O_2 supplies 67

4.20 Single-cell area plotted over time under oscillating O_2 environments . . . 68

4.21 Periodic growth dynamics synchronized to applied O_2 oscillations 69

4.22 Periodic growth dynamics visualized on polar plots 71
4.23 Comparison of phase-averaged growth data across different *T’* 72

5.1 Metabolic pathways in *C.glutamicum* under aerobic and anaerobic conditions 78
5.2 Phase-contrast images of *C. glutamicum* cultivated under oscillating O_2 supplies, with/without the addition of peptone or amino acids 81
5.3 *C. glutamicum* growth analysis cultivated under oscillating O_2 supplies . . 82
5.4 Comparison of phase-averaged growth rates with different supplements . 83
5.5 *C. glutamicum* single-cell area plotted over time under oscillating O_2 environments 84

6.1 Different approaches for spatial O_2 control in the fluid channel and chambers 88
6.2 Conceptual illustration of spatial O_2 control with side gas channels 89
6.3 O_2 gradient in the fluid channel with side gas channels 90
6.4 Conceptual illustration of spatial O_2 control with large gas channels in the double-layer chip for high throughput 91
6.5 Setup for structuring O_2 gradient in the fluid channel with the double-layer chip 93
6.6 O_2 gradient structured in the fluid channel with the double-layer chip . . . 94
6.7 Conceptual illustration of spatial O_2 control with finer gas channels in the double-layer chip for recreating µm-scale gradient 95
6.8 Top layer designs of the double-layer chip to recreate µm-scale O_2 gradients 96
6.9 Dimension of the top layer with finer channels 97
6.10 Image of the fabricated double-layer chip with finer gas channels 98
6.11 Measured channel width of the fabricated double-layer chip for µm-scale gradient 99
6.12 O_2 measurement with FLIM in the double-layer chip with finer gas channels (chamber 1) 100
6.13 O_2 measurement with FLIM in the double-layer chip with finer gas channels (chamber 2) 101

6.14 Conceptual illustration of spatial O_2 control with a glass-made top layer in the double-layer chip 102
6.15 Dimension of the glass-made top layer 104
6.16 Detailed dimension of the glass-made top layer 105
6.17 Fabrication procedure of the double-layer chip with glass top layer 106
6.18 Image of the fabricated double-layer chip with the glass top layer 107
6.19 Phase-contrast images of the fabricated channels in the glass-made top layer 108
6.20 Measured channel width of the glass-made top layer 109
6.21 Recommended designs of finer gas channels in the top layer 110

7.1 Example of cell tracking analysis 116

List of Tables

3.1 LB medium composition 28
3.2 Defined M9 medium composition 29

A.1 Parameters used in simulation 144

B.1 Permission for re-use of contents from previous studies 145

A Simulation Setup

For the specified model, the fluid and gas flow through the corresponding channels were computed by solving the time-dependent Navier-Stokes equations for laminar and incompressible flow, as follows.

$$\begin{aligned} \frac{\delta \rho}{\delta\, t} + \nabla \cdot (\rho\, \mathbf{u}) = 0 \\ \rho \frac{\delta \mathbf{u}}{\delta t} + \rho(\mathbf{u} \cdot \nabla)\mathbf{u} = \nabla \cdot [-\, pI + \, K] \\ K = \mu(\nabla \mathbf{u} + (\nabla \mathbf{u})^T) \end{aligned}$$

ρ is density (kg/m^3), $\mathbf{u}$ is velocity vector (m/s), p is pressure (Pa), I is identity matrix, and μ is dynamic viscosity (Pa $\cdot$ s). Boundary conditions at the PDMS block and the glass plane are defined as follows.

$$\begin{aligned} \mathbf{u} &= 0 && \text{(wall)} \\ \mathbf{u} &= -\mathbf{n}U_0 && \text{(inlet)} \\ [-pI + K]\mathbf{n} &= -p_0\mathbf{n} && \text{(outlet)} \end{aligned}$$

$\mathbf{n}$ is the boundary normal vector pointing out of the domain, and U_0 is the normal inflow speed.

With $\mathbf{u}$ given by the Navier Stokes equations, O_2 transport via convection and diffusion was simulated using the diluted species transport application in COMSOL, with specific boundary conditions, as follows. The O_2 level in the surrounding air is assumed to remain constant at 21%.

$$\begin{aligned} \nabla \cdot \mathbf{J}_i + \mathbf{u} \cdot \nabla c_i = R_i \\ \mathbf{J}_i = -D_i \nabla c_i \end{aligned}$$

i is the index for different domains (water, air, PDMS), D_i is the diffusion coefficient of each domain i. $\mathbf{u}$ for PDMS is 0. c_i is the concentration of O_2 (mol/m^3) in each domain i.

Table A.1: Parameters used in simulation (1 atm, 310.15 K)

	water	PDMS	air (21% O_2)	air (100% O_2)
S (mol/m^3)	0.218 [152]	1.25 [152]	8.1375	-
D (m^2/s)	2.7×10^{-9} [152]	7×10^{-9} [152]	2.3×10^{-5}	-
ρ (kg/m^3)	993.31	-	1.1383	1.24
μ (Pa $\cdot$ s)	0.00101	-	1.814×10^{-5}	-

R describes sources or sinks. Boundary conditions between different domains are defined as follows.

$$\frac{c_i}{S_i} = \frac{c_j}{S_j} \qquad \text{(between PDMS and gas / water channel)}$$

$$c_{\text{PDMS-air}} = S_{\text{PDMS}} = 1.25\ \text{mol/m}^3 \qquad \text{(between PDMS and surrounding air)}$$

$$-\mathbf{n} \cdot \mathbf{J}_i = 0 \qquad \text{(at the glass plate)}$$

$$c_{\text{water-air}} = S_{\text{water}} = 0.218\ \text{mol/m}^3 \qquad \text{(between water and air)}$$

S_i is the solubility of O_2 (mol/m^3) in each domain i at 1 atm and at 310.15 K. Initial S_{air} was calculated to be 8.134 mol/m^3. The parameters used in the simulation were summarized in Table A.1.

The mesh for the provided geometry was generated using a semi-automated approach. First, a hexahedral mesh was constructed for the fluid channel. Boundaries with surrounding parts were then converted to a triangular mesh. The remaining domains are finally meshed by a tetrahedral mesh with an "extra-fine" resolution.

B Permission for Re-Use of Contents

The permission numbers for materials re-used from previous studies are summarized in Table B.1.

Table B.1: Permission for re-use of contents from previous studies.

Figure number	Reference	Permission license number
1.1, 1.4	[7]	Permission not required
1.1	[8]	5954810688782
1.1	[9]	5954831319970
1.2	[27]	5955310060592
1.3	[51]	1571504-1
1.3	[52]	5955360829859
1.3	[49]	Permission not required
1.3	[54]	Permission not required
1.3	[50]	1571526-1
1.4	[62]	Permission not required
1.4	[63]	Permission not required
2.2	[84]	5906510575894
2.2	[78]	5906511140079
5.1	[145]	5921420434602